High-Pressure Studies of Energetic Materials

Alistair J. Davidson

A thesis submitted in fulfilment of the requirements for the degree of Doctor of Philosophy to the School of Chemistry, the University of Edinburgh

2008

Abstract

Although high pressure has been used extensively to study a range of materials that include metals, minerals, and ices, a class of material that has received rather less attention are energetic materials (explosives, propellants). The work presented has used high-pressure techniques to investigate polymorphism in energetic materials.

Novel-high pressure phases of RDX (cyclotrimethylenetrinitramine or cyclonite) and ammonium perchlorate are reported, which have both been structurally characterised using single-crystal X-ray and powder neutron diffraction. Of particular importance has been the successful determination of the structure of the elusive high-pressure γ-form of RDX. Equations of state for both polymorphs of both compounds have been determined. Hydroxylammonium perchlorate has been investigated using high-temperature single-crystal X-ray diffraction and powder neutron diffraction, and a high-temperature phase has been fully structurally characterised for the first time. High-pressure studies of hydroxylammonium perchlorate indicate the presence of two new polymorphs.

High-pressure measurements of HMX (cyclotetramethylenetetranitramine or octogen) revealed no phase transitions up to 8.46 GPa. An equation of state up to this pressure has been determined. Crystallisation of HMX from DMSO at 0.1 GPa gives a 1:2 HMX-DMSO solvate which has been structurally characterised by single-crystal X-ray diffraction. The high-pressure behaviour of TATP (triacetone triperoxide) has been explored.

High-pressure studies have been performed on ammonium nitrate up to 7.85 GPa, showing no phase transitions. An equation of state has been determined over this pressure range.

Studies have also been undertaken on the simple molecular compound thiourea dioxide. Two new high pressure phases have been identified and structurally characterised using both single-crystal X-ray and powder neutron diffraction.

Abbreviations

RDX	Cyclotrimethylenetrinitramine
HMX	cyclotetramethylenetetranitramine
AP	Ammonium Perchlorate
HAP	Hydroxylammonium Perchlorate
AN	Ammonium Nitrate
ADN	Ammonium Dinitramide
DMSO	Dimethyl Sulfoxide
DMF	N-N-Dimethylformamide
NMP	N-Methyl-2-Pyrrolidinone
TNT	Trinitrotoluene
PTTN	Nitroglycerine
CL-20	Hexanitrohexaazaisowurtzitane

Acknowledgements

I would like to that everyone who has helped me during my PhD. In particular I would like to thank Dr. Colin Pulham for being an excellent and encouraging supervisor. I would also like to thank Dr. William Marshall for all his help and advice.

All members of the Pulham Group and CSEC for making the last three years extremely enjoyable. In particular I would like to thank Dr. Iain "F & C" Oswald, Dr. Francesca Fabbiani and Christopher Spanswick for their very useful input during the course of my PhD.

Duncan Francis, Dr Alistair Lennie, Dr. Timothy Prior and Dr. John Warren for all their help with experiments at ISIS and Daresbury. Dr. David Allan for high-pressure advice both at Edinburgh and central facilities. Dr. Adam Cumming for his assistance with all the work conducted on energetic and explosive materials. Dr. Simon Parsons and the crystallography service for running samples. In addition, the University of Edinburgh, CCLRC and MOD WPE (through Dstl under the terms of contract RD028-06366) for funding.

Finally I would like to thank my parents and my wife, Esther Hoffman for their support, and putting up with me whilst I've been writing this thesis.

Contents

Chapter 1

Introduction

Chapter One: Introduction

1.1 Polymorphism

The term "polymorphism" is used in many disciplines to describe the diversity of nature. According to the Oxford English Dictionary, the term first appeared in 1656 to describe changes in fashion. In chemistry and materials science, polymorphism can be defined as the phenomenon by which a substance can adopt more than one crystal structure. These different crystal structures are denoted polymorphs. There are examples in older literature of the term *pseudo-polymorphism*, when referring to solvates and hydrates. This notation has been discouraged due to its rather confusing nature.

The classic example of polymorphism occurring in nature is represented by carbon and three of its main polymorphs (allotropes) - carbon, graphite and C_{60}, (buckminsterfullerine). Each of these forms display markedly different structures and properties (Figure 1.1). For example, graphite is a black, soft, electrically conducting and chemically reactive material. Diamond is optically transparent, hard, electrically insulating, and chemically rather inert. The most recently discovered allotrope, C_{60} is quite different from both. Its structure comprises hexagons and pentagons in a closed shell. It is soluble in aromatic solvents and can be vaporised at relatively low temperatures.

The differences in properties displayed by these three allotropes of carbon are a result of their different crystal structures. Some of the most common properties to be

altered due to polymorphism are conductivity, melting and boiling points, density, heat capacity, dissolution rate, solubility, and solid-state chemistry [1].

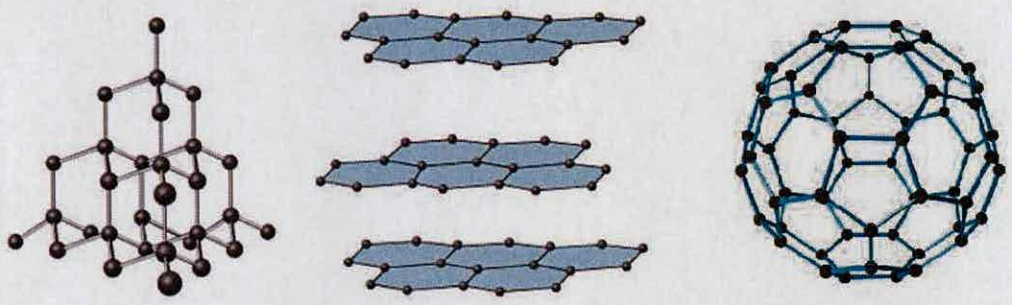

a b c

Figure 1.1. Structures of (a) diamond, (b) graphite, and (c) C_{60}

The phase diagram of carbon under different conditions of temperature and pressure is given in Figure 1.2. Both diamond and graphite possess two crystallographic forms. Graphite can adopt a hexagonal form and a rhombohedral form. Diamond can adopt a hexagonal form (lonsdaleite) and a cubic form (gem-stone). The thermodynamically stable form of carbon under normal conditions is the hexagonal form of graphite.

Due to the high energetic barrier for interconversion between the two phases of carbon, the transition from diamond to graphite at normal conditions is very slow. The transition to diamond can occur more rapidly by applying increased temperatures and pressures to graphite. There are currently two main methods used to produce synthetic diamond from graphite. High-Pressure High-Temperature (HPHT) is often used because

of its relatively low cost. Large presses are used to create pressure up to 5 GPa at 1500°C. The aim is to reproduce the conditions that create natural diamond inside the Earth.

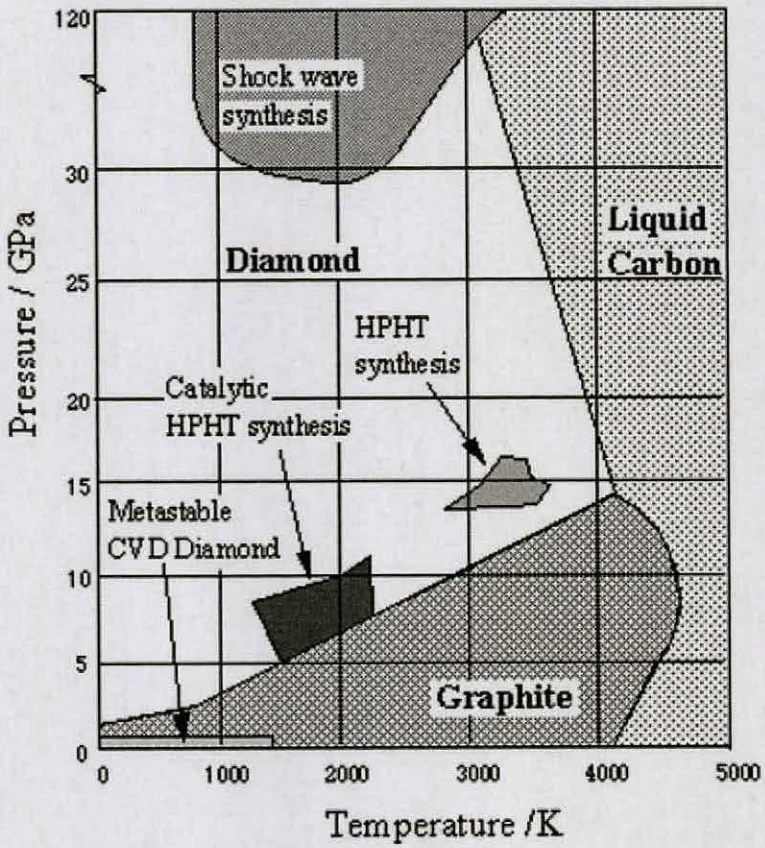

Figure 1.2 Pressure-temperature phase diagram of elemental carbon [2]

Another technique of HPHT synthesis of diamond from carbonaceous materials is one which makes use of the short time compression and high temperatures that occur during detonation. Various types of carbonaceous precursors can be used in this detonation process, but graphite is the most widely used. The second method is chemical

vapor deposition (CVD). This does not require high-pressure and high-temperature conditions to create diamond crystallites. This method creates a carbon plasma above a substrate onto which carbon atoms deposit to form diamond.

Polymorphism can also occur in molecular compounds, and a good example is provided by ice. Two solid phases of water are known to occur at the Earth's surface. As water freezes it undergoes a phase transition from liquid to ice-Ih. This is referred to as hexagonal ice [3]. As ice-Ih is further cooled below -80 °C a further phase transition occurs to ice Ic, a cubic form. Figure 1.3 shows the 2D crystal structure of Ice Ih [4]. There are at least eleven polymorphs of ice that have been identified under a variety of different temperatures and pressures. These are shown in the phase diagram in Figure 1.4 [5]

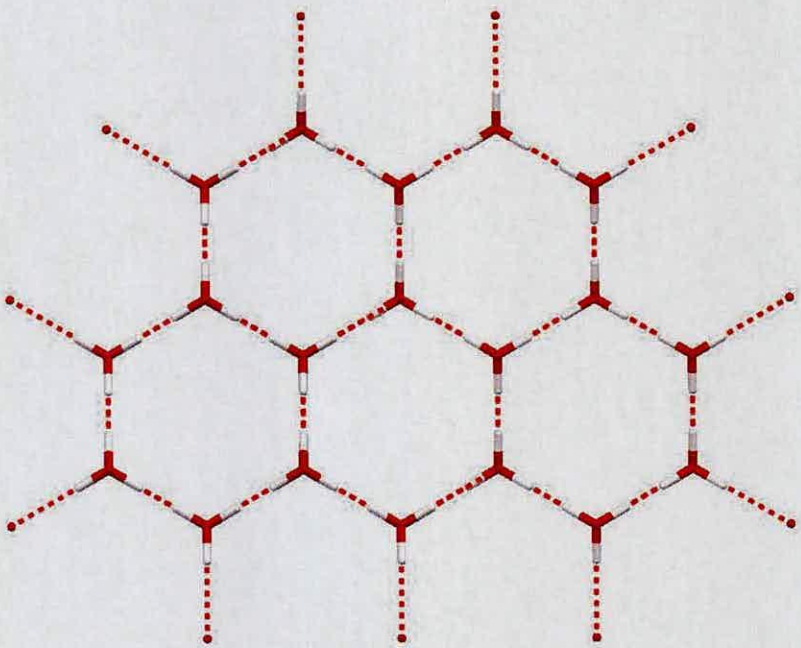

Figure 1.3 Crystal structure of ice Ih viewed down the *c*-axis. Hydrogen bonding interactions shown in red.

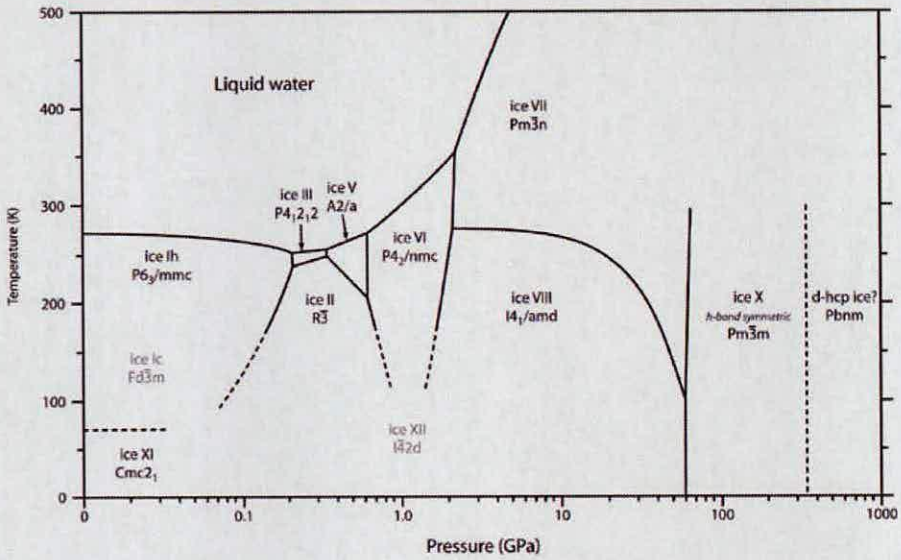

Figure 1.4 Phase diagram of ice [5]

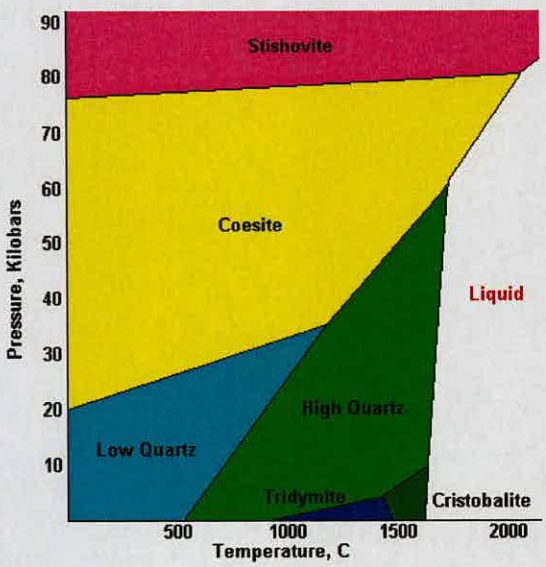

Figure 1.5 Phase diagram of silica

Polymorphism is also widespread in minerals. For example silica, SiO_2, exhibits a remarkable variety of polymorphs. The stability of the different polymorphs of silica under differing ranges of temperature and pressure is illustrated in Figure 1.5.

1.2 Implications of Polymorphism

1.2.1 Pharmaceutical Compounds

The increased awareness and importance of polymorphism in the last thirty years is probably due to the pharmaceutical industry. Polymorphism and solvate formation can alter almost all of the solid-state properties of a drug molecule. As such, the pharmaceutical industry expends much time and money in the search for new polymorphs. Areas for concern in the industry are as follows:

- *Bio-availability and solubility*: Most drugs are administered in the solid form and rely on dissolution in the gastro-intestinal tract for their action. Hence if two polymorphs of the same drug compound have very different solubilities, then the bio-availabilities of the two forms may be very different with implications for administration of the correct dosage to the patient.
- *Processibility and storage*: The conditions under which polymorphs interconvert is of critical importance, particularly when pharmaceuticals may encounter changes in temperature, pressure and relative humidity during processes such as drying, granulation, milling, pellet production, and storage. It is important to know if any phase transitions are possible in order to control the properties of drugs selectively and consistently. The importance of polymorphism in the pharmaceutical industry is

strikingly illustrated by the case of Abbott Laboratories' protease inhibitor for HIV, Ritonavir [6]. In 1996 the drug was brought on to the market as a semi-solid capsule in liquid form. However, in 1998 a significant proportion of capsules failed a dissolution test. The presence of a new crystalline form was discovered, which was thermodynamically more stable and hence less soluble. Thus new methods to process this new form were developed, and when combined with the subsequent requirements to satisfy regulatory bodies, this resulted in substantial financial costs for the company.

- *Regulatory authorities*: As a result of the patient risk associated with polymorphism occurring in drug compounds, regulatory authorities such as the US Food and Drug Administration (FDA) now require detailed information about drug polymorphs in order to grant licenses for products.
- *Intellectual property*: Intellectual property and patents are also an issue for pharmaceutical companies, where challenges to patents have been made on the basis of the discovery of a new polymorph. Since crystal modifications of a substance represent different crystal structures with potentially different properties, the discovery or preparation of a new crystal modification represents an opportunity to claim an invention that can potentially be recognised in the awarding of a patent. Challenges to patents on the basis of polymorphism are therefore becoming increasingly frequent and very expensive [7].

1.2.2 Dyes and Pigments

The pigment and dye industry has been a significant commercial enterprise since the discovery of the dye indigo, which is the source of colour for the ubiquitous blue jeans. The precise distinction between pigments and dyes has been contested much the same as the definition of polymorphism. However, a working definition is that dyes are soluble and thus normally adsorbed onto fabrics, while pigments are generally regarded as insoluble. Since both these substances are solids, the solid state chemistry and dependence of their properties on different polymorphic structures have been of considerable interest [1]. One of the best examples of a pigment displaying polymorphism is copper phthalocyanine (Figure 1.6). At least five forms are known, designated α, β, γ, δ, ε, which all have different solubilities.

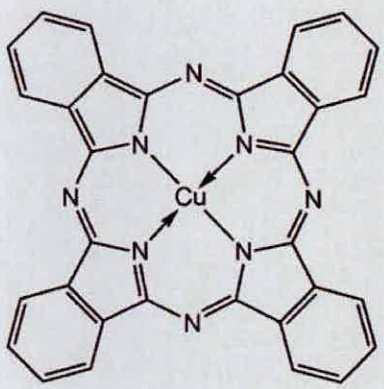

Figure 1.6 Molecular structure of copper phthalocyanine

These different polymorphs have different shades of blue (from green to red). The β-form is used as the standard letter press printing ink, and the ε-form is used as a colour filter for liquid crystal displays.

Polymorphism and solid-state phase transitions can also have significant effects on the scientific study and applications of energetic materials. This is covered in detail in section 1.3

1.3 Energetic Materials

1.3.1 Definition

The majority of the work presented in this thesis is concerned with energetic materials. Energetic materials can be defined as those that generate large amounts of heat and generally a large amount of gas upon stimulus by heat, impact, shock, spark, *etc* [8]. A chemical explosion is the result of a chemical reaction or change of state that occurs over an extremely short space of time (typically < 0.01s). Due to the extreme speed of the reactions, the gases formed do not have time to expand instantaneously, and remain for a fraction of a section trapped inside the reaction vessel that was once occupied by the explosive material. At this point, the volume remains constant and extremely small, and the temperature is extremely high (several thousands of °C). A consequence of this is the creation of very high pressures that cause a 'shock wave'

which breaks the walls of the reaction vessel and causes destruction to surrounding objects.

1.3.2 Classification

Explosives can be classified as primary and secondary explosives [8]. Primary explosives undergo a very rapid transformation from burning to detonation. They can be considered to be sensitive materials that require relatively mild stimulus to cause detonation. This then leads to a short, strong shock wave. Primary explosives are often used as initiators to detonate less sensitive materials. Examples of primary explosives include materials such as lead azide (Figure 1.7a), nitrogen triiodide (NI_3) and triacetone triperoxide (TATP, Figure 1.7b). This latter material will be discussed further in Chapter 4.

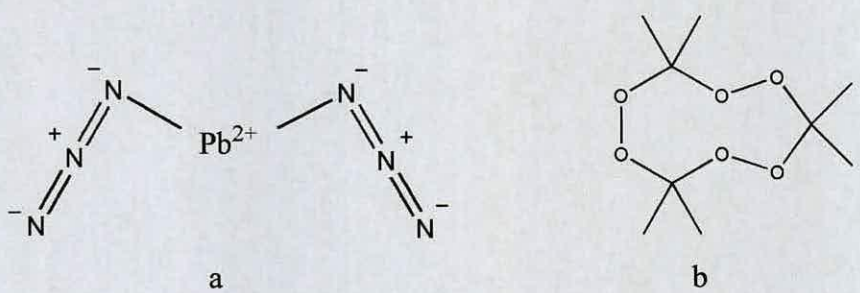

Figure 1.7 Molecular structure of (a) lead azide, and (b) TATP

Secondary explosives are much less sensitive. They cannot be detonated readily by heat or shock. Secondary explosives can only be initiated to detonation by the shock produced by the explosion of a primary explosive. On initiation, secondary explosives

create a much more powerful and sustained shock wave. Some secondary explosives are so stable that they cannot be detonated by rifle bullets. Examples of secondary explosives are HMX, RDX and TNT (Figure 1.8).

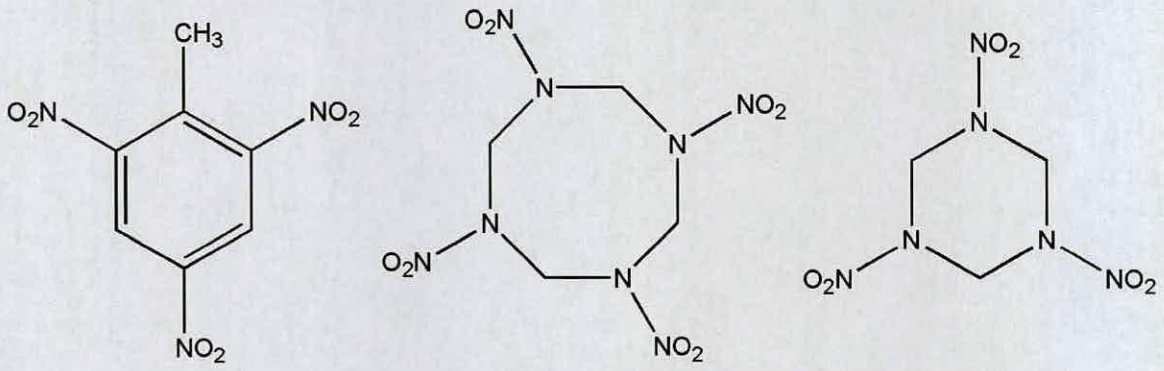

a b c

Figure 1.8 Molecular structures of (a) TNT, (b) HMX and (c) RDX

Propellants are a further type of energetic material. They can be defined as materials which undergo rapid and predictable combustion (without detonation) resulting in a large volume of hot gas. This gas can then be used to propel a projectile, such as a bullet or missile, or in gas generators to drive a turbine, *i.e.* torpedoes. An example of a propellant is ammonium perchlorate (NH_4ClO_4), which is used by NASA in its space shuttles, and will be discussed in greater detail in Chapter 5.

1.3.3 Effects of Polymorphism on Energetic Materials

Many high-energy materials have been shown to be polymorphic. An example of this is TNT (trinitrotoluene-Figure 1.8a), which is reported to have both an orthorhombic form and a monoclinic form. However, the solid-state chemsitry of TNT is poorly understood, since it is very difficult to prepare the material in a single-crystal form. PTTN (nitroglycerine, Figure 1.9) has been known since 1914 to be polymorphic [1]. The structure of the stable orthorhombic form is known, while a triclinic metastable form has been reported, although its structure is not known [1]. In addition, materials such as HMX, RDX and TATP show rich phase behaviour, and will be discussed further in the thesis.

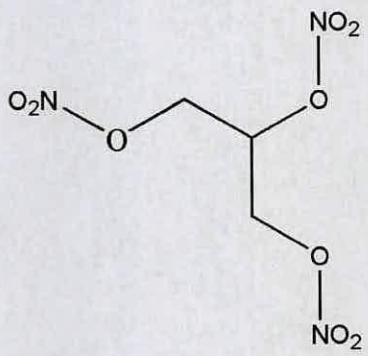

Figure 1.9 Molecular structure of nitroglycerine

Polymorphism and solid-state phase transitions can have significant effects on the scientific study and applications of energetic and explosive materials. This is due to several reasons:

- *Defects*: during solid-state phase transitions, crystals may develop surface and internal defects, such that the crystal size may be reduced. This is important in energetic materials because the more defects in a crystal, the easier it is to initiate. This is because during the initiation process and associated compression, energy becomes concentrated at defect sites because of cavitation and/or frictional heating. This leads to the formation of "hot spots" and it is from these that the reaction front propagates outward leading to a violent runaway reaction. Thus the sensitivity of energetic materials is related to the number of defects. In fact, a perfect crystal of a high explosive is not a particularly good explosive [8].
- *Density*: As previously mentioned, changes in phase of a material can cause a change in the density. This is important in high-energy materials because to a first approximation the detonation velocity of an energetic material is proportional to density [8]. In addition, the most dense polymorph of an explosive material is often chosen due to the fact that many applications of energetic materials are volume limited. The crystal morphology of a given polymorph also governs how well material can be processed and packaged, e.g. prismatic crystals pack more efficiently than crystals with rod, needle, or platelet morphologies.
- *Sensitivity*: Different polymorphs of an energetic material can display quite different sensitivities. An example of this can be found in HMX, which has four different polymorphs under ambient conditions (the γ-form is actually a hydrated form rather than a true polymorph) and the sensitivity to impact has been found to occur in the

order $\delta > \gamma > \alpha > \beta$ [8]. The β-form is used in military applications due to concerns about unwanted detonation of the three other forms.

- Reproducibility: A fundamental requirement of explosive materials is the reproducibility of its performance, and that reproducibility can be compromised by polymorphic variations and transformations.

A good example of polymorphism affecting the performance of an energetic material is found in ammonium nitrate (AN). At 32 °C, the most stable form of AN (IV) undergoes a transition to form III, which is accompanied by an increase in volume. Temperature cycling due to ambient temperature fluctuations around the transition temperature causes fracturing of crystallites, forming a fine powder which often "cakes". This caked powder contains significantly more defects, and as such this material is more sensitive to accidental detonation when attempts are made to break up the caked salt [8].

Thus, polymorphism has considerable impact on energetic and explosive materials in a complicated manner. For example, a phase transition in an energetic material could potentially turn a rocket motor into an explosive charge.

1.4 High-Pressure Research

The field of high-pressure research has been of significant scientific interest for over one hundred years. In 1905, P. W. Bridgman developed an opposed-anvil device for compressing solids, which led to unprecedented pressures of 5-10 GPa (50000 – 100000 atmospheres). This represented a regime for materials which had not previously

been attainable. In these new accessible pressure ranges, well-known substances started to behave in unexpected ways. He realised that sudden changes in the arrangement of atoms could be achieved using high pressure i.e. structural transitions. Thus, high pressure could be used as a new tool for probing polymorphism in a range of compounds and materials. For example solid H_2O transformed into ice-VI, which only started to melt above 100°C. Bridgman received a Nobel Prize in 1946 for his pioneering work. Since then researchers have continued to study materials under conditions of high pressure. An overview of the high-pressure research being undertaken, which is by no means exhaustive, is given in section 1.4.1. In high-pressure research, there is often use of more than one unit of pressure. The unit of gigapascals (GPa) will be employed in this work. The relationship between the three most common units are as follows:

9869.2 atm =10 kbar = 1 GPa

1.4.1 Previous High-Pressure Research

- *Metallic Elements*: High-pressure techniques have revealed remarkably complex crystal structures for the metallic elements. In many cases, these structures are found to be incommensurate, having either a host-guest composite structure, or modulations of the atomic positions [9]. For example, application of pressure to Rb creates an incommensurate structure stable between 17 and 20 GPa. Ba, Sr, Bi and Sb have been reported to show similar behaviour [9].

- *Elements, Groups 12-16*: The high-pressure behaviour of element groups 12-16 have been widely studied [10,11]. On the application of pressure, these compounds often adopt high symmetry structures with increasing coordination numbers. At pressures of around 10 GPa, these materials tend to be covalently bonded semiconductors, with some forming metallic structures under further increase of pressure. An example of this is ZnS, which shows very interesting phase behaviour. The stable low-pressure form of ZnS is zinc-blende. Under high pressures, this form transforms to the NaCl structure, and behaves as an indirect-gap semiconductor [12]. At pressures of *ca.* 65 GPa, the NaCl phase is reported to undergo a further transformation into an orthorhombic *Cmcm* phase, with no significant change in volume [13].
- *Actinides:* The high pressure behaviour of the actinides has been studied experimentally up to pressures of 100 GPa [14]. Despite the more complex structures of the lighter actinides, the application of pressure has not been reported to produce differences in the state of the 5f orbitals. This results in few phase transitions. The pressure studies have shown that the metals are not very compressible (large bulk modulus). However protactinium has been observed to change phase at 77 GPa. In contrast, for the trans-plutonium metals, the 5f states are localised at atmospheric pressure and their bulk moduli are smaller. Application of pressure on these metals leads to delocalisation of their 5f states, and a transition to

similar packing arrangements to the light actinides. High-pressure phases have been suggested for Cm and Cf, but they have not yet been characterised.

- *Synthesis of New Materials:* In the past, high-pressure synthesis has focused on the industrial preparation of synthetic diamonds and cubic boron nitride, which are the superhard abrasives of choice for cutting and shaping hard metals and ceramics. High pressure has also been utilised to explore superconductivity of the elements. Until fairly recently, superconducting behaviour was only known for a few elements and compounds. Under high-pressure conditions, the "superconducting periodic table" now extends to all almost all classes of elements, and ionic compounds. An emerging area is the discovery of the solid-state chemistry of light-element "gas" molecules such as CO_2, N_2 and N_2O. These react to give polymerized covalently bonded or ionic mineral structures on application of pressure and temperature. These new solids are potentially tractable to ambient conditions [15].
- *Planetary Materials*: Most materials known in the Earth's crust are tetrahedrally based silicates. Geologists have studied density-driven phase transitions in depth, in the hope that the results might lead to highly coordinated mineral species, thus affecting the density profile and seismic wave propagation within the Earth [16]. The composition of the Earth's mantle is modelled within the $MgSiO_3$-Mg_2SiO_4 systems. Experiments performed under conditions of high pressure have shown that below 670 km (which corresponds to pressures greater than 24 GPa), minerals transform into an assemblage of MgO and $MgSiO_3$ perovskites [17, 18]. Silicate

perovskite is probably the most abundant mineral on Earth, but it has never been discovered at the surface. High-pressure techniques are also providing maps of the mineral content of planets such as Mars and Venus. Deep inside gas giants, Jupiter and Saturn and their moons, experiments have shown that their mineralogy is based on C-O-N-H chemistry. Light-elements such as CO_2, CO, N_2 and NO_x usually give rise to multiply bonded species [19]. However, polymerization reactions occurring under conditions of very high pressures lead to covalently bonded frameworks and unexpected ionic solids [20]. N_2 has the strongest intramolecular bond known, but when subjected to pressures greater than 180 GPa, it becomes a singly bonded polymorph [21].

- *Liquids and Glasses*: High-pressure studies of liquids and glasses were first performed by Bridgman [15]. Melting temperatures generally increase with increasing pressure. However, some substances show the inverse of this, with negative dT/dP slopes, indicating that the liquids are denser than the corresponding crystals. Examples of this can be found for H_2O, Si, Ge, Bi and Ge. A "two-state" model of the liquid structure was suggested to explain this unusual behaviour. The liquids could simultaneous contain both low and high density forms. As pressure is increased the proportion of each form changes, and the liquid become unusually dense; crystals float rather than sink in it. This behaviour is well know for a water-ice mixture under ambient conditions, but is also seen in minerals such as $(Mg,Fe)_2SiO_4$-olivine, within the Earth's mantle. Modelling of this two state

behaviour show that the liquids develop a critical point during cooling, indicating the onset of a new type of liquid-liquid transition between the low- and high-density phases. These different liquid polymorphs have identical compositions, but have different densities and entropies. The transitions are comparable with high-pressure, high-temperature polymorphism seen in crystalline phases [15].

- *Origin of Life*: For most of the past century, conventional wisdom has suggested that the Earth's energy-rich surface was the most logical site for life's origin. Recent discoveries of abundant life in high-pressure areas such as deep oceans, hydrothermal vents and crustal rocks, and the surprising high-pressure stability of some microbes, has suggested a wider range of plausible origin environments [22]. It has been suggested that the discovery of life in such unusual circumstances implies the possibility that life-forming processes may also have occurred in the wet, high-pressure environments found in the interiors of Mars, Europa and other objects in the solar system.
- *Protein Crystallisation*: High-pressure protein crystallisation has been widely examined [23]. The preparation of large, high quality single-crystals which are required for X-ray structure analysis still presents a large problem. Pressure has been investigated as a candidate to control the protein crystallisation, since hydrostatic pressure affects the whole system uniformly and can be changed very quickly. Experiments on a range of proteins have shown that solubility, growth rate and nucleation rates can be tuned using high pressures up to 120 MPa.

- *Food Processing*: High-pressure treatment has emerged as a useful method as a food processing technology. Applying high pressure to food products modifies interactions between individual components, influences reaction rates of enzymatic reactions and can inactivate microorganisms. Pressures in the region of hundreds of MPa are used in these experiments. Another advantage is that factors such as colour and flavour are not altered on application of pressure. Foodstuffs such as milk, cheese, ham, oysters and orange juice are currently produced using high-pressure food technologies [24].
- *Pharmacology and Medicinal Applications*: High pressure has emerged as an important tool to tackle several problems in biotechnology and medicine. Misfolded proteins, aggregates and amyloids have been studied, with the aim of increasing understanding of protein-misfolding diseases. Diseases of this type include emphysema and cystic fibrosis. The use of high pressure has been useful in identifying the mechanisms behind these defects, and in creating therapies against these diseases. High pressure has also been used to study viruses for the purpose of sterilisation and in the development of vaccines, through the ability of pressure to inactivate viruses, prions and bacteria [25].

1.4.2 Molecular Systems at High Pressure

As previously mentioned, the structure of elements has been widely study with a wide range of pressure induced allotropy reported. However, in contrast, there have

been relatively few studies on molecular systems under pressure. This represents a remarkable gap in the field of high-pressure chemistry. The studies performed on molecular systems have focused on compression studies to investigate intermolecular and intramolecular interactions, and also in the search for new polymorphs.

The role of intermolecular and interatomic interactions in solids is of great interest to structural chemists. These interactions are of fundamental importance in controlling the structure and behaviour in the solid state. The response of materials to changes in external conditions can reveal information about the nature of these interactions. These interactions are significantly distance dependent, and as such high pressure can prove a highly useful tool for investigating these interactions. Utilising high pressure provides a way to overcome the ordinary stability limits of materials set by the ambient condition thermodynamics.

The study of the response of intermolecular interactions in a crystal as a result of hydrostatic pressure provides important knowledge. In particular, the changes in hydrogen bonding interactions offer information about the properties of compounds. The knowledge gained through understanding of hydrogen bonds and their response to pressure may lead to better prediction and control of polymorphism in materials.

Recently high-pressure groups in Edinburgh have conducted studies on simple organic molecules such as amines, ketones, carboxylic acids, alcohols and urea derivatives which have shown very rich and interesting phase behaviour [26, 27]. This will be discussed in detail in Chapter 7. High-pressure compression studies have also

been performed at Edinburgh on amino acids [28, 29, 30, 31]. Amino acids are simple molecules which are the building blocks for polypeptides and proteins, and are often used in the synthesis of larger pharmaceutical molecules. The study of simple compounds containing a particular functional group is a crucial step towards the understanding of interactions, bonding characteristics and packing motifs of specific types of compounds. Many of these compounds such as L-glutamine, and L-β-glutamic acid, have not shown any polymorphism, but have displayed significant closing of central voids in their crystal structures. However L-cysteine showed very interesting behaviour. A single-crystal to single-crystal transition was observed under direct compression to form a new polymorph designated form III. On depressurisation, a new form (IV) was observed to appear at 1.7 GPa. The crystal structure of form IV separates into zones with motifs that are alternatively form I and form III-like. Form IV can thus be thought of as an unusual example of an intermediate phase.

1.4.3 Effects of Pressure on Pharmaceutical Compounds

As shown in section 1.4.1, high pressure is a proven way of exploring polymorphism in a wide range of compounds. It can thus be expected that pressure would have a similar affect on pharmaceutical compounds. During processing of a pharmaceutical, the drug molecule will come into two high pressure environments, namely milling (mechanical grinding) and tabletting. Milling has been shown to increase the surface area, and has also been reported to increase the number of defects

present in the crystals, such as fractures and dislocations [32]. If the number of defects in the crystal is large, this can ultimately lead to loss of long range order, i.e. the material becomes amorphous. This has an affect on the drug's properties since amorphisation leads to an increase in both the dissolution and the solubility of the substance.

An example of a material undergoing polymorphism as a result of milling is phenylbutazone (this is used as a non-steroidal anti-inflammatory drug for the treatment of chronic pain, including the symptoms of arthritis), where grinding at 4 °C has been shown to cause the formation of two new polymorphs. In addition metastable forms of caffeine and paracetamol have been transformed to more stable polymorphs by grinding [7].

Tableting involves the direct compression of a pharmaceutical. The pressure applied in the instance is generally in the range of 40-200 MPa. An example of this can be found in the metastable form of caffeine. On application of pressure, a transformation to the more stable form was observed in the range 100-400 MPa, and the extent of transformation was found to depend on the zone of the tablet, the pressure applied and the particle size of the powder [7].

1.5 High-Pressure Studies of Energetic Materials

High pressure plays an important role in the chemistry and understanding of energetic and explosive materials. When a high-energy material undergoes a detonation, the shock waves can cause pressures of up to 50 GPa, and temperatures of up to 5500 K

[33]. These extreme conditions can result in polymorphic changes and cause the initiation of chemical reactions. As a result of this, a large amount of effort has been put into studying these materials under conditions of high pressure and high temperature, with the hope of improving the understanding of the mechanisms of detonation and also any structural changes which occur during an explosion [34]. There are three main techniques used for studying these materials under pressure. The first is direct static compression where pressures of up to 30 GPa and 650 K can be achieved. The second technique is the dynamic shockwave method. A shock wave is created by firing a high-velocity projectile from either a gas gun or explosive charge. Velocities of up to 8 kms^{-1} can be achieved. When the projectile hits the material, a shock-wave is created that can reach pressures of up to 100 GPa. Shock waves can also be created using high power lasers, which are used to produce a high-pressure plasma that acts either directly on the material or launches a flyer plate into it [34]. Measurement of the propagation speed of the shock-wave front through the material and the change of the velocity across the front (i.e. the velocity of the material behind the front if the material ahead of the front is at rest) is then used to determine the equation of state of the material.

The third method of studying energetic materials is *via* computational methods. These methods allow examination of a wide range of temperatures and pressures, and can provide detailed information about reaction mechanisms and rates under extreme conditions. The aim of these computational studies is to accurately predict and model the behaviour, performance and characteristics of current and new energetic materials.

1.5.1 Previous High-Pressure Research

The effects of temperature on energetic materials have been studied in detail. By comparison, the number of high-pressure studies on such compounds is relatively few. Where high-pressure studies have been performed, there is a noticeable lack of structural information. A summary of the experiments conducted on some well known energetic and explosive materials is given below.

HMX: HMX (octahydro-1,3,5,7-tetranitro-1,3,5,7,-tetrazocine, or Octogen, Figure 1.8b) is a commonly used secondary explosive. Under ambient conditions, three polymorphs (α, β, and δ) and a hemihydrate (usually referred to as γ-HMX) are known, and have been structurally characterised [8]. There has been considerable interest in the variable temperature and pressure behaviour of HMX. A transition from the β-form of HMX to the δ-form is observed at 158°C on heating at atmospheric pressure. This $\beta \rightarrow \delta$ transition is typically associated with the thermal decomposition of HMX [35,36]. The high pressure behaviour of all polymorphs and hydrates of HMX has been studied, and this is further discussed in Chapter 3.

RDX: Two polymorphic forms of RDX (Cyclotrimethylenetrinitramine or Cyclonite, Figure 1.8c) are known, designated α and β [37,38]. There has been significant interest in the high-pressure behaviour of RDX, with a well known transition occurring to a new γ-phase at approximately 4.0 GPa. This is described in detail in Chapter 3.

Ammonium Perchlorate: Ammonium perchlorate (AP), $[NH_4]^+[ClO_4]^-$ is an energetic oxidiser in solid rocket motors and explosive compositions. Under ambient conditions of temperature and pressure, ammonium perchlorate adopts an orthorhombic crystal structure (*Pnma*). [39,40,41].

The high-temperature behaviour of AP has been widely studied, with a structurally characterised transition to a new cubic form occurring above 511K. With respect to high-pressure behaviour, several studies have been performed, with a high pressure suggested to form at approximately 4.0 GPa. Both the high-temperature and high-pressure behaviour of ammonium perchlorate are described in Chapter 5.

Ammonium Nitrate: Ammonium nitrate (AN), $[NH_4]^+[NO_3]^-$ is an energetic oxidiser, which forms an explosive mixture when combined with hydrocarbons such as diesel or kerosene.

AN is an excellent example of a highly polymorphic energetic material, with five known temperature phases are known at ambient pressure [42]. Ammonium nitrate has been studied under hydrostatic conditions, with no phase transitions reported. However under non-hydrostatic conditions, a possible new phase has been suggested to form. This is reported in Chapter 5.

CL-20: CL-20 (hexanitrohexaazaisowurtzitane or 2,4,6,8,10,12-hexanitro-2,4,6,8,10,12-hexaazatetracyclododecane, or HNIW, Figure 1.10a) is currently the densest and most powerful energetic material known to have a practical use. It is primarily used as a propellant. Four polymorphs (α, β, γ, ε) are know under ambient

conditions [43]. The formation of a new ζ-form has observed under direct compression studies at 0.7 GPa using FTIR, energy dispersive X-ray powder diffraction, and optical polarizing light microscopy (OPLM) [44]. The high-pressure high-temperature phase diagram of CL-20 was also investigated using FTIR and OPLM. The study demonstrated the different thermal decomposition temperatures associated with the different polymorphs. The γ-form decomposes at 0.4 GPa and between 240-260° C, while the α-form decomposed between 0.4 GPa and 10.0 GPa, at temperatures between 250-300°C. The high pressure ζ-form decomposed above 10.0 GPa between 300-340 °C. Theoretical studies have also been performed on CL-20 investigating the behaviour of the lattice parameters and unit cell volume with increasing pressure [45].

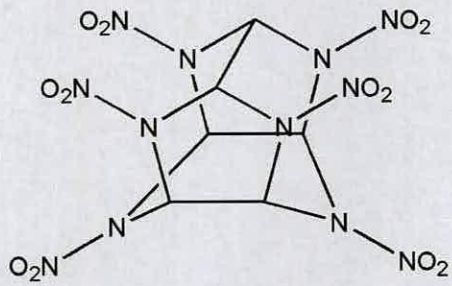

a

b

Figure 1.10. Molecular structures of (a) CL-20 and (b) AND

Ammonium Dinitramide: Ammonium dinitramide (ADN) (Figure 1.10b) is an inorganic oxidizer with minimum signature characteristics. ADN is considered as a possible replacement for ammonium perchlorate in propellant applications due to decreased hydrochloric acid production. ADN addresses concerns about pollution of

both the upper atmosphere and wetlands near launch pads, because its use as a propellant significantly reduces the level of harmful contaminants introduced to these environments [46]. The crystal structure under ambient conditions has been determined. Variable temperature studies have been performed up to 353K, with no reported phase transitions [47]. The pressure-temperature phase diagram has been determined using optical polarizing light microscopy, laser-Raman spectroscopy and energy dispersive X-ray diffraction. A transition to a new monoclinic cell has been suggested to occur above 2.0 GPa [47]. In addition this study showed that above 140 °C, and between pressures of 1.0-10.0 GPa ADN undergoes a molecular rearrangement to form ammonium nitrate and N_2O. More recent results performed using powder neutron diffraction studies have revealed no phase transitions up to a pressure of 4.03 GPa [48].

1.6 General Aims and Outline of Research

As a consequence of the lack of structural information obtained for energetic materials at high pressures, high-pressure studies have been conducted on a range of materials. The aims of the work are as follows:

- To investigate pressure-induced structural changes for a range of energetic materials
- To identify and characterise new phases prepared under pressure *in situ*

- To increase understanding of the effects of pressure on energetic materials

Chapter 3 describes the high-pressure studies of HMX and RDX using single-crystal X-ray diffraction and neutron diffraction. Chapter 4 is a study of TATP. Chapter 5 describes the study of the salts ammonium perchlorate and ammonium nitrate using single-crystal and powder X-ray diffraction, powder neutron diffraction and Raman spectroscopy. Chapter 6 is an investigation of hydroxylammonium perchlorate (HAP) under conditions of high temperature and high pressure. Chapter 7 illustrates that high pressure can also be used to study simple molecular compounds. In this case, high-pressure experiments were conducted upon thiourea dioxide. Conclusions and future directions are described in Chapter 8.

1.7 References

[1] J. Bernstein, *Polymorphism in Molecular Crystals*, IUCr Monographs on Crystallography, Clarendon Press, Oxford, UK, 2002.

[2] F. P. Bundy, *J. Geophys. Res.*, 1980, **85(B12)**, 6930.

[3] R.W. Whitworth, *J. Phys. Chem. B.*, 1999, **103**, 8192.

[4] S. Jenkins, I. Morrison, *J. Phys.: Condens. Matter.*, 2001, **13**, 9207.

[5] A. D. Fortes, I. G. Wood, M. Alfredsson, L. Vocadloa and K. S. Knight, *J. Appl. Cryst.*, 2005, **38**, 612.

[6] S. R. Chemburkar, J. Bauer, K. Deming, H. Spiewk, K. Patel, J. Morris, R. Henry, S. Spanton, W. Dziki, W.Porter, P. Quick, P. Bauer, J. Donaubauer, B. A. Narayanan, M. Soldani, D. Riley, K. McFarland, *Organic Research and Development.*, 2000, **2**, 412.

[7] F. P. A. Fabbiani and C. R. Pulham, *Chem. Soc. Rev.*, 2006, **35**, 932 and references therein

[8] J. Akhavan, *The Chemistry of Explosives*, 2nd Edition; Royal Society of Chemistry. 2004

[9] M. I. McMahon and R. J. Nelmes, *Z. Kristallogr.*, 2004, **219**, 742.

[10] G. J. Ackland, *Rep. Prog. Phys.*, 2001, **64(4)**, 483.

[11] A. Mujica, A. Rubio, A. Munoz, R. J. Needs, *Rev. Mod. Phys.*, 2003, **75(3)**, 863.

[12] S. U. Ves, N. E. Schwarz, K. Christensen, K. Syassen, M. Cardona, *Phys. Rev. Lett.*, 1990, **42**, 9133.

[13] R. J. Nelmes and M. I. McMahon, *Semicond. Semimetals.*, 1998, **54**, 145

[14] A. Lindbaum, S. Heathman, T. Le Bihan, R. G. Haire, M. Idiri, G. H. Lander, *J. Phys.Condens. Matter.*, 2003, **15**, S2297.

[15] P. F. McMillan, *Nature Materials.*, 2005, **4**, 715.

[16] L. G. Liu and W. A. Bassett, *Elements, Oxides, Silicates: High-Pressure Phases with Implications for the Earth's Interior*, Oxford University Press, Oxford, UK,1986.

[17] R. J. Hemley, *Ultrahigh-Pressure Mineralogy: Physics and Chemistry of the Earth's Deep Interior*, Reviews in Mineralogy, Mineralogical Society of America, Washington DC, U.S.A. 1998, **37.**

[18] R. J. Hemley, *Ann. Rev. Phys. Chem.*, 2000, **51**, 763.

[19] P. F. McMillan, *Nature Materials.*, 2002, **1**, 19 and references therein.

[20] M. I. Eremets, *J. Chem. Phys.*, 2004, **121**, 11296.

[21] G. Jenner, *Tetrahedron.*, 2002, **58**, 5185.

[22] R. M. Hazen and R. T. Downs (Eds), *Rev. Min. Geochem.*, 2005, **41.**

[23] Y. Suzuki, G. Sazaki, S. Miyashita, T. Sawada, K. Tamura, H. Komatsu, *Biochim, Biophys. Acta.*, 2002, **1595**, S929 and references therein.

[24] C. E. O'Reilly, A. L. Kelly, P. M. Murphy, T. P. Beresford, *Trends in Food Science and Technology.*, 2001, **12**, 51 and references therein.

[25] J. L. Silva, D. F. Marisa Suarez, A. M. O. Gomes, A. C. Oliveira, *J. Phys. Condens. Matter.*, 2004, **16**, S929 and references therein.

[26] D. R. Allan, S. J. Clark, A. Dawson, P. A. McGregor, S. Parsons, *Acta Cryst.*, 2002, *B***58**, 1018.

[27] D. R. Allan, S. J. Clark, R. M. Ibberson, S. Parsons, C. R. Pulham, *Chem. Commun.*, 1999, **8**, 751.

[28] S. A. Moggach, D. R. Allan, P. Lozano-Casal, S. Parsons, *J. Synchrotron Rad.*, 2005, **12**, 590.

[29] S. A. Moggach, D. R. Allan, S. Parsons, L. Sawyer, J. E. Warren, *J. Synchrotron Rad.*, 2005, **12**, 598.

[30] S. A. Moggach, D. R. Allan, C. A. Morrison, S. Parsons, L. Sawyer, *Acta Cryst.*, 2005, *B***61**, 58.

[31] A. Dawson, D. R. Allan, S. A. Belmonte, S. J. Clark, W. I. F. David, P. A. McGregor, S. Parsons, C. R. Pulham, L. Sawyer, *Cryst. Growth Des.*, 2005, 1415.

[32] H. G. Brittain, *J. Pharm. Sci.*, 2002, **91**, 1573 and references therein.

[33] Y. B. Zel'dovich and Y. P. Raiser, *Physics of Shockwaves and High Temperature Hydrodynamics Phenomena*, Academic Press, New York, 1966.

[34] R. W. Shaw, T. B. Brill, D. L. Thompson, *Overviews of Recent Research on Energetic Materials, Advanced Series in Physical Chemsitry*, Worlfd Scientific, Singapore. 2005, **16**.

[35] H. Czerski, M. W. Greenway, W. G. Proud, J. E. Field, *J. Appl. Phys.*, 2004, **24**, 409.

[36] B. F. Henson, B. W. Asay, R. K. Sander, S. F. Son, J. M. Robinson, P. M. Dickson, *Phys. Rev. Lett.*, 1999, **82**, 1213.

[37] W.C. McCrone, *Anal. Chem.*,1950, **22**, 954.

[38]. C.S Choi, and E. Prince, *Acta Cryst.*, 1972, **B28**, 2857.

[39] K. Venkatesen, *Proc. Ind. Acad. Sci.*, 1957, *A***46**, 134.

[40] H. G. Smith, H. A. Levy, *Acta Cryst.*, 1962, **15**, 1201.

[41] H. J. Prask, C. S. Choi, *J. Chem. Phys.*, 1974, **61**, 3523.

[42] C. S. Choi and H. J. Prask, *J. Appl. Cryst.*, 1980, **13**, 403.

[43] T.P. Russell, P.J. Miller, G.J. Piermarini, and S. Block, *J.Phys. Chem.*, 1993, **97**, 1993.

[44] T. P. Russell, P. J. Miller, *G.* J. Piermarini, and S. Block, *J. Phys. Chem.,* 1992, **96**, 5509.

[45] D. C. Sorescu, B. M. Rice and D. L. Thompson, *J. Phys. Chem.*, 1999, **103**, 6783.

[46] H. Östmark, U. Bemm, A. Langlet, R. Sanden and N. Wingborg, *J. Energetic. Mat.*, 2000, **18**, 123.

[47] T. P. Russell, G. J. Piermarini, S. Block and P. J. Miller, *J. Phys. Chem.*, 1996, **100**, 3248.

[48] A. J. Davidson, A. Cummings, D. J. Francis, W. G. Marshall, C. R. Pulham, unpublished results, 2006.

Chapter 2

Experimental Techniques

Chapter Two: Experimental Techniques

2.1 The Merrill-Basset Diamond Anvil Cell

The basic principle of the diamond–anvil cell (DAC) is relatively simple. A sample is placed between two flat parallel diamond faces and the sample is subjected to conditions of high pressure when a force pushes the opposed anvils together. Due to the fact that diamond is transparent to a wide range of electromagnetic radiation energies, DACs have been utilised for both X-ray diffraction and spectroscopic studies.

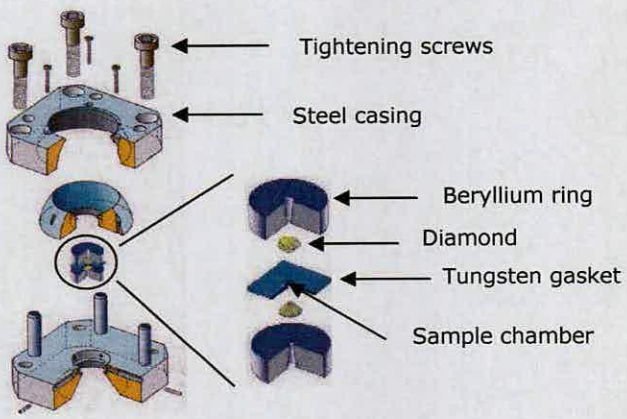

a

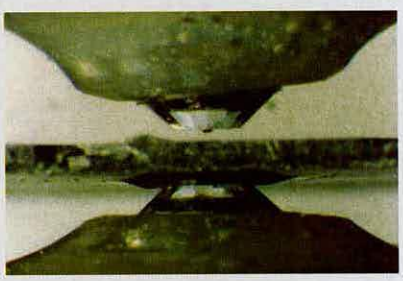

b

Figure 2.1 (a) assembly of diamond-anvil cell, (b) cross section of DAC [1]

Much of the work undertaken in this thesis was performed using a Merrill-Bassett DAC [1] (shown in Figure 2.1and 2.2). The DAC is ~5 cm in diameter and comprises two gem-quality diamonds attached to beryllium discs. A small cylindrical hole is present in the centre of these discs to allow optical observation of the sample and access to X-rays and electromagnetic radiation. These discs are then held in a stainless steel casing by small screws to allow alignment of the diamond anvils. The

sample chamber is a tungsten gasket, which is created by drilling through a pre-indented 250 μm piece of tungsten by spark erosion. This gasket is then placed in the cell and aligned with the diamonds' thrust axis. Pressure is then applied by tightening the three allen screws attached to the steel casing. As the diamonds are pushed together, the gasket extrudes outwards around the culets (diamond face), sealing the sample chamber. In this configuration, very little force is required to create extremely large pressures in the sample chamber. The pressure limit of the cells used in Edinburgh is about 12 GPa but can be substantially increased by reducing the size of the gasket hole and the diamond culets.

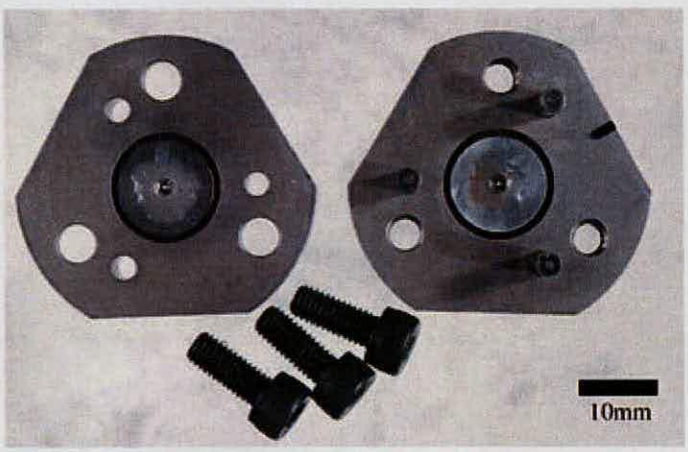

Figure 2.2 Diamond anvil cell separated showing allen screws.

2.1.1 Components of the DAC

- *Diamonds*

The culet size of the diamonds that are used in the DAC play a big part in determining the pressure which can be reached. The diamond culets used in this

work have varied between 400 and 800 μm. The most common cause of diamond failure in the DAC is a result of poor alignment of the diamonds.

- *Backing Discs*

Beryllium was used as the backing discs in the DACs used in this work. Due to its low atomic number, Be is relatively transparent to X-rays, which allows wide angle X-ray access to the sample. Beryllium also has a high mechanical strength and so can be used to reach pressures in excess of 20 GPa. A disadvantage of using Be is the presence of a high background due to scattering in single-crystal diffraction experiments. Furthermore, Be is toxic, and so its machining and subsequent handling require care. Consequently, beryllium is increasingly being replaced by tungsten carbide seats.

- *The Gasket*

The gasket is very important in the construction of the DAC. Not only does it provide the sample chamber for the experiment, but it also provides mechanical support for the diamond anvils, reducing the shear stress at the culet tips. A variety of metals such as rhenium, tungsten, steel and inconel (an alloy of Ni, Cr and Fe) are used, depending upon the experiment. Each of these metals has different mechanical properties and hence will restrict the pressures that can be obtained during the experiment. Tungsten is suitable for large sample volumes, as it has high mechanical strength which maintains the sample volume. The large sample volume limits the total pressure that can be applied to the sample, but this limit is outside the range of pressures that can be accessed using the Merrill-Bassett DAC [1].

For pressure to increase, the volume of the sample chamber must decrease. The force pushing outwards from the sample chamber must be equalled by the

inwards force from the shear strength of the gasket and the friction between the diamond culets and the walls of the gasket hole. As a result of this, the thickness of the gasket is very important. If the gasket is too thick, the outwards force from the sample will exceed the friction, which will cause the hole to expand, and no pressure will be applied. On the other hand, a very thin gasket will limit the sample volume.

The manner is which the gasket is prepared is also important. Prior to drilling a gasket hole, the gasket is indented between the two anvils. This is to ensure the gasket is at the required thickness (100-180 μm). The support from the increased thickness of the gasket outside the anvils allows higher pressures to be attained, than calculated from the anvil size, gasket hole, and gasket thickness alone [2]. The thick flank supports the culets, thereby reducing the shear stress on the diamonds. The indenting work also hardens the gasket, thereby improving its mechanical stability.

- *Pressure-transmitting medium*

Most studies performed in this work have been performed under hydrostatic conditions. The use of an encapsulating fluid as a pressure-transmitting medium generally fulfils this condition provided the fluid does not solidify in the pressure range under study. As such, the selection of an appropriate pressure-transmitting medium is crucial, as non-hydrostatic media can cause several problems. Significant broadening and shifts in diffraction peaks may be observed under non-hydrostatic conditions. Such conditions can also promote or suppress phase transitions, and may also lead to amorphisation of the sample. In addition, they can modify the relative evolution of cell parameters with pressure and can cause problems in determining pressure using ruby fluorescence on account of broadening of the R_1 line (Section

2.1.3). Thus non-hydrostatic conditions can adversely affect results such as the equation of state of materials.

In much of the work presented in this thesis, a 4:1 mixture of methanol: ethanol by volume was used. This has been shown to be hydrostatic up to pressures slightly in excess of 10 GPa. However, a disadvantage of this mixture is that some samples may react or dissolve in these alcohols. For these compounds an alternative pressure-transmitting medium is Fluorinert-FC75 (3M), which has been shown to be hydrostatic up to 2.3 GPa. The large difference in pressure range between methanol: ethanol and Fluorinert-FC75 caused problems, as the aim of this project was to explore materials up to pressures of 10 GPa. For this reason a medium called HT70 (GALDEN) which is a mixture of perfluorinated ethers was investigated. Preliminary studies of HT70 have suggested that this liquid may be hydrostatic up to 4.5 GPa, which would be a significant improvement on current pressure-transmitting media [3].

2.1.2 Sample Loading

The majority of studies undertaken with a DAC reported were conducted using direct compression studies of materials as either a single crystal or polycrystalline powder. For both types of experiment, the sample was loaded into the tungsten gasket chamber along with a ruby chip and a pressure-transmitting medium.

In a few cases, single crystals were grown from solution under pressure. In this case a solution of the sample was loaded into a DAC, which was then pressurised. This normally caused a decrease in the solubility of the compound, and

usually resulted in the precipitation of a polycrystalline material. This powder could then be studied by X-ray powder diffraction, and/or spectroscopic methods. Further studies could also be conducted using single-crystal diffraction. The cell was temperature-cycled until most of the powdered sample had disappeared, and all that remained was a single crystallite. A large single crystal could then be grown from this seed as the system was cooled. For the cases in which single crystals have been grown from solution, detailed descriptions are given in the particular chapter.

2.1.3 Pressure Calibration

The ruby fluorescence method was introduced in 1972 as a new way for calibrating the pressure in the DAC [4]. Prior to this, pressure was determined by internal pressure markers such as sodium chloride or silver. Further studies have established the ruby fluorescence method as a quick and simple way for pressure measurement [5]. A small chip of ruby is placed in the tungsten gasket together with the sample and a pressure-transmitting medium. The R lines of the ruby (Al_2O_3: Cr^{3+}) fluorescence spectrum are very intense. Studies have shown that the R_1 electronic transition shows a linear dependence with pressure up to at least 25 GPa [5]. Ruby fluorescence in this work was induced using the 632.8 nm line from a He-Ne laser, and was dispersed and detected by a Jobin-Yvon LabRam 300 spectrometer with a typical precision in the measurements of $\pm$ 0.05 GPa.

2.2 The Paris-Edinburgh Pressure Cell

The other pressure cell which has been used in this work is the Paris-Edinburgh Cell (PEC), which was developed in 1992 [6]. Neutron diffraction requires samples *ca.* 10^6 times larger than that required for powder X-ray diffraction and so prior to 1992 pressures of above 5 GPa were not accessible for neutron diffraction studies. The development of the Paris-Edinburgh cell has extended the range of pressures that can be accessed for neutron powder diffraction studies to 10-20 GPa. A schematic of the cell is given in Figure 2.3.

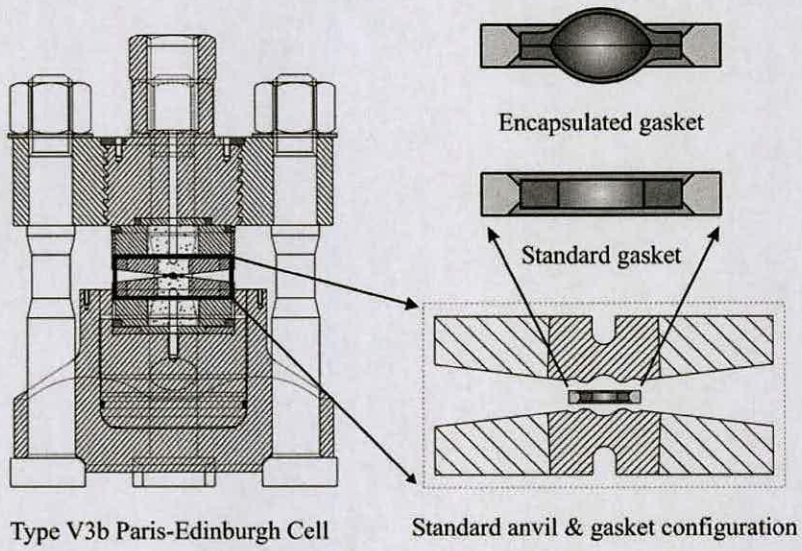

Figure 2.3. Schematic of the Paris Edinburgh Cell (PEC) with encapsulated gasket.

The PEC is an opposed anvil device in which the sample is placed between two anvils. Application of pressure is then achieved by means of an *in situ* hydraulic ram, which can apply loads of up to 250 tonnes between the two anvils. The cell weighs about 50 kg, which is significantly lighter than previous cells used for

neutron work, and as such provides easier transportation. Up to 100 mm^3 can be loaded into the PEC.

2.2.1 Components of the PEC

- *Gasket*

A standard TiZr gasket has been used in Paris-Edinburgh cells since 1992, since the 1:1 titanium-zirconium alloy is a null scatterer. However on several occasions, attempts to compress samples beyond 2 GPa led to the failure of anvils through cracking. More recently, it was realised that it was necessary to prevent the pressure-transmitting medium from coming into contact with the anvil surface to protect the anvils [7]. For this reason, an encapsulated gasket was developed (Figure 2.3), that allows compression up to pressures of at least 9 GPa.

- *Anvils and Pressure-transmitting media*

The anvils used in a PEC are made from tungsten carbide or sintered industrial diamonds.

Similar pressure-transmitting media are used in PECs as in DACs, although deuterated media are used.

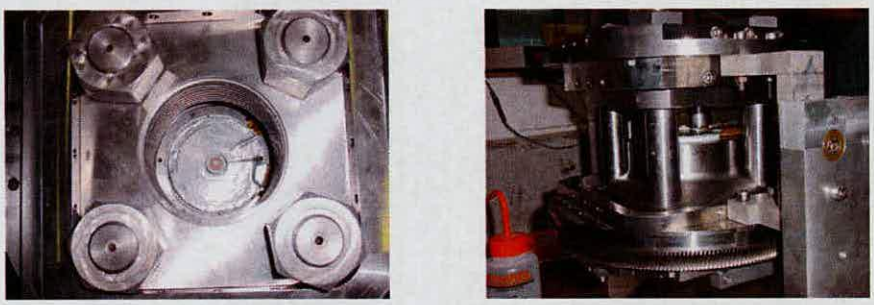

a b

Figure 2.4. Paris-Edinburgh cell viewed from (a) above and (b) side view

2.2.2 Pressure Calibration

A disadvantage of WC anvils is that they are optically opaque. Thus, measurement using the ruby fluorescence method is not possible. Instead, sodium chloride and lead have been used as pressure markers in this work. The high-pressure equations of state for NaCl and Pb are well known, and both materials adopt cubic structures, with space group *Fm*3*m* [8, 9]. Thus a small amount of the marker is loaded into the TiZr gasket along with the powdered sample.

2.3 Raman Spectroscopy

Raman spectroscopy has been less widely used than infrared spectroscopy (IR), but recent advances in instrument technologies have simplified the equipment, and so Raman spectroscopy is now relatively straightforward and ideally suited for high-pressure studies using DACs.

In Raman spectroscopy, the energy levels of molecules are explored by examining the frequencies present in the radiation scattered by molecules. In an experiment a monochromatic laser source of frequency ν_0 is directed through a sample. The scattered light is collected and passed through a monochromator. The latter scans frequencies from near the incident laser frequency to lower frequencies and the output is plotted as scattered intensity against wavenumber. About *ca.* 1.5 % of incident photons emerge from collisions with a lower energy. These scattered photons constitute the lower-frequency Stokes radiation from the sample. Other incident photons may collect energy from the molecules and emerge as higher-frequency anti-Stokes radiation. The component of radiation scattered into the

forward direction without change of frequency is called Rayleigh radiation. This can be seen in Figure 2.4. Generally, Raman spectra are plotted with respect to the laser frequency such that the Rayleigh band lies at 0 cm^{-1}. On this scale, the band positions will lie at frequencies that correspond to the energy levels of different functional group vibrations.

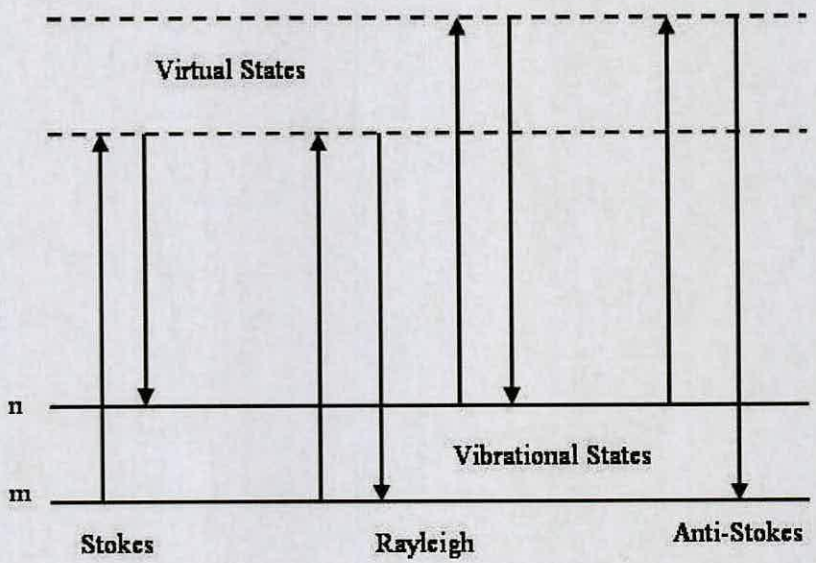

Figure 2.4 Rayleigh and Raman scattering processes. The lowest energy state m is shown at the bottom of the diagram with states of increasing energy above it.

The selection rule associated with Raman spectroscopy is that for a vibration to be Raman active the polarisability of the molecule must change with the vibrational motion. This is best pictured as the ease with which the electron cloud is distorted i.e. polarised.

Raman spectroscopy is particularly useful for the work described in this report because monochromatic light is used. This means that any material that is transparent to visible light can be used as a sample chamber (e.g. thin walled glass

tubes, diamond). Furthermore sample examination can be carried out by focussing the incident beam with a microscope, which is very useful when using the DAC.

Detection of solid-state phase transitions is possible using Raman spectroscopy since the active vibrational modes of molecules are strongly dependent upon molecular symmetry. Raman-scattered light is polarised and can assist in the identification of the symmetries of molecular vibrations. As pressure is increased in a Raman experiment there is a general increase in frequency of most vibrational bands. This is because of changes in environment, solution and intermolecular potential. Thus if pressure is increased on a crystal that remains in the same phase, a constant shift in wavenumber will be observed, and a plot of wavenumber against pressure will show a constant gradient. A phase transition can cause a change in symmetry of a molecule or modify the intermolecular interactions present. This can lead to changes in the vibrational frequency of a band. Raman spectra were collected using a LabRam instrument equipped with a 50 mW He-Ne laser of wavelength 632.8 nm. An excellent description of the subject is covered in Smith and Dent's text [10].

2.4 X-Ray Diffraction

2.4.1 Single-Crystal X-Ray Diffraction

X-ray diffraction is the most widely used and least ambiguous method for the determination of positions of atoms in molecules and solids. X-ray diffraction occurs when a beam of X-rays interacts with electrons in a material and is elastically scattered. Separations between atoms or ions are characteristically a few Å and are

thus comparable to typical X-ray wavelengths (e.g. Mo-Kα radiation, λ = 0.71073 Å).

Bragg presented the basis of diffraction in 1912 and showed that resultant reflected rays are only in phase for certain angles of incidence of the X-rays upon the crystal. This is illustrated in Figure 2.6, which shows the path difference between the two rays, if one assumes that the atoms lie in the diffracting plane. For these two rays to combine they must be completely in phase i.e. their path difference ($2d \sin\theta$) must be a whole number of wavelengths ($n\lambda$) where d is the separation between the planes and λ is the wavelength of the X-rays. This leads to the Bragg Equation, $n\lambda = 2d\sin\theta$, which correctly predicts that a reflected beam will be observed (i.e. constructive interference) only for certain angles of incidence of the X-ray beam on the crystal; at other angles of incidence the rays from the different layers of the crystal will be partly or completely out of phase (destructive interference).

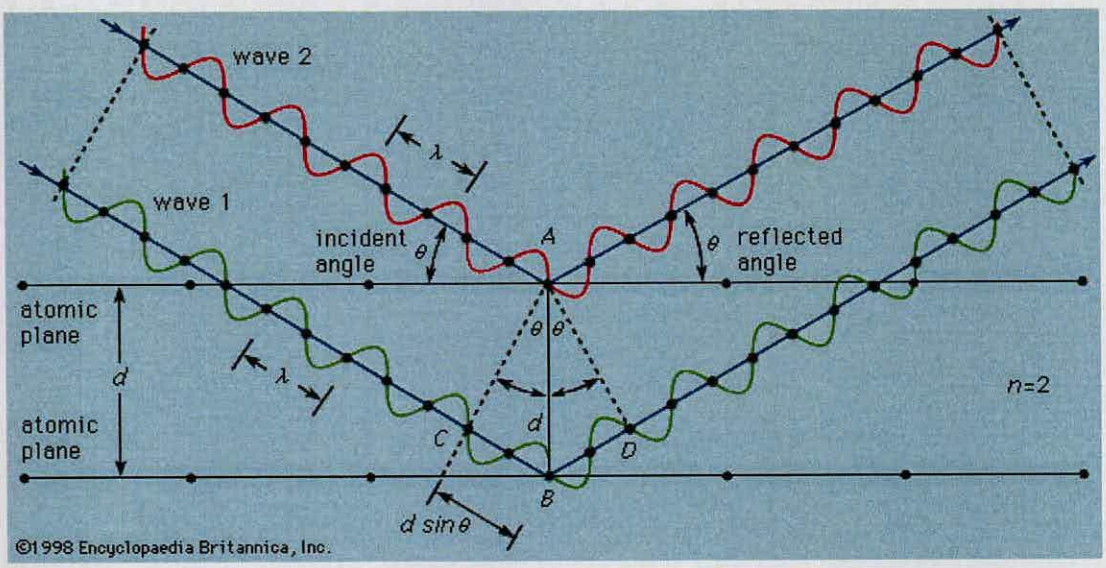

Figure 2.6 The Bragg construction for diffraction by a two planes of atoms

The intensities of the diffraction pattern are related to the arrangement and nature of atoms in a crystal by a Fourier transformation. The intensities observed provide information about amplitudes of the waves, but provide no knowledge about the phase of the wave. This is one of the main challenges to the X-ray crystallographer, since both the amplitude and the phase of the X-rays scattered by a crystal are required for structure determination. The determination of approximate phases can be achieved by structure solution (Patterson, direct methods). Calculated phases are then combined with observed intensities. Fourier transformation is then used to create a better model (and as such a new set of calculated phases). Structure refinement is then undertaken, where the aim is to create the best agreement between observed and calculated amplitudes or intensities, leading to determination of the crystal structure. An in depth description of this methodology is presented in W. Massa's and C. Giacovazzo's respective texts on the subject [11, 12].

2.4.1.1 Data Collection and Processing

The majority of experiments presented in this thesis were undertaken at the SRS Daresbury Laboratories, Warrington, UK, on Stations 9.8 and 16.2 on a Bruker APEX 2 CCD diffractometer at 293(2) K using synchrotron radiation X-ray wavelengths of between 0.65 Å and 0.85 Å. Some work was undertaken at Edinburgh on a Bruker-Nonius APEX 2 CCD diffractometer using Mo-Kα radiation, $\lambda = 0.71073$ Å at 293(2) K.

Data collection was performed according to an established 1-second ω-scans procedure. Data were processed according to the procedure described by Dawson *et al* [13].

Figure 2.7 illustrates a typical frame from an APEX 2 CCD recorded using a DAC. Diffraction from the diamonds and the beryllium backing discs can cause problems with data manipulation as they can overlap with sample reflections leading to anomalous intensities. Hence, the whole process of indexing, integration and structure solution is more challenging than studies conducted at ambient pressure.

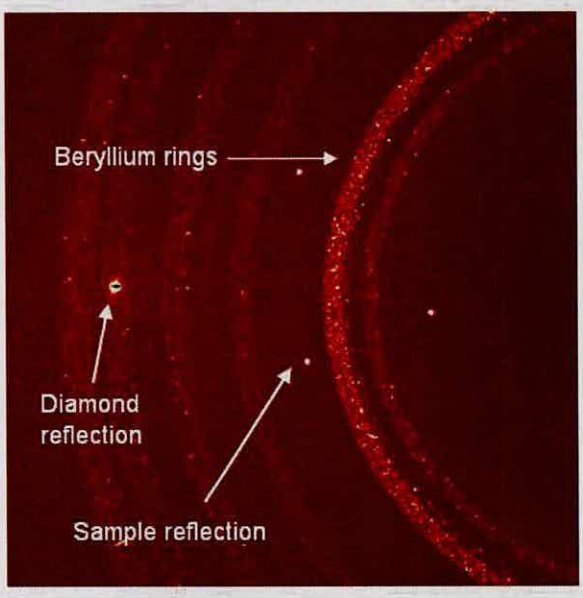

Figure 2.7. APEX 2 CCD frame obtained for a high-pressure sample in a DAC.

A thresholding algorithm in the APEX 2 program was used to harvest sample reflections [14]. Orientation matrices and unit cell parameters were obtained using the same program. Data integration and global-cell refinement were preformed using the program SAINT [15]. Dynamic masks were implemented during integration to ensure that intensity data were not harvested from the regions of the detector that are shaded by the body of the DAC and areas of intense beryllium

diffraction. Dynamic masks have been shown to significantly improve results of integration.

The quality of the data can be improved by implementing various corrections. For example, an analytical absorption correction was employed in SHADE [16]. This rejects reflections that lie within 2° of the high-pressure cell opening angle (40°) and have poorly fitting profiles. A multi-scan absorption correction was performed using SADABS [17]. This corrects for differences in path lengths of X-ray through the crystal, which varied as the crystal orientation changed. Data were merged using the SORTAV [18] in the WinGX [19] suite of programs.

The structures reported in this thesis were solved either by reciprocal-space methods (direct methods: SHELXS [20], Sir92 [21], Sir2002 [22]), or by direct-space methods (FOX [23]). The manner in which each structure was solved is detailed in each relevant chapter. One of the main problems with high-pressure data is the limit in reciprocal space that can be accessed caused by shading from the steel body of the DAC.

This problem can be overcome using direct-space methods which have previously been used for solution of structures from powder data [21]. This particular area has developed significantly in the last few years, with the introduction of global optimisation methods for powder samples. The success of these methods derives from the fact that the problem of structure solution is reduced to determining only molecular position, orientation and internal conformation. However, these methods are only successful when the molecular contents of the crystal structure are known. Once a solution has been obtained, structure

refinement was performed using the program CRYSTALS [23], which will be described in each relevant section.

2.4.2 Powder X-Ray Diffraction

A single crystal gives a three dimensional diffraction pattern with discrete diffracted beams, each in a certain direction relative to the orientation of the crystal and the incident beam, as stipulated by the Bragg equation. A microcrystalline powder consists of an essentially infinite number of tiny crystals, and this produces concentric rings for each reflection, with the radii determined by the Bragg equation. Theoretically the intensities should be closely related to those that would be produced by one single crystal. As such, in a powder pattern, the information contained in the spatial distribution of the reflection is lost. Only the single dimension of the scattering angle remains, and this makes the problem of indexing, and obtaining any specific intensity measurement rather difficult. The main advantage of powder diffraction is that it is far easier to obtain a powder of a sample as opposed to a single crystal, as in some cases it is difficult to grow a suitable crystal for single crystal X-ray diffraction. In addition, powder X-ray diffraction experiments are much quicker to perform than single-crystal X-ray diffraction experiments, and the technique is therefore an excellent method for phase identification.

The high-pressure X-ray diffraction experiments were performed on Station 9.5 HPT at the SRS Daresbury Laboratory, Warrington, UK. White beam X-rays impinge on a silicon crystal cleaved parallel to the (110) plane in Laue geometry to produce monochromatic beams. Bending the crystal allows focusing of the

monochromatic beam over a distance of four metres, thereby intensifying the radiation. This focused beam is used to probe the samples contained in a DAC. Diffraction from crystalline phases within these cells is then recorded on a MAR345 image plate detector for subsequent processing [25]. A schematic of the experimental set up on Station 9.5 is shown in Figure 2.8, with an example of a powder pattern detected on an image plate illustrated in Figure 2.9

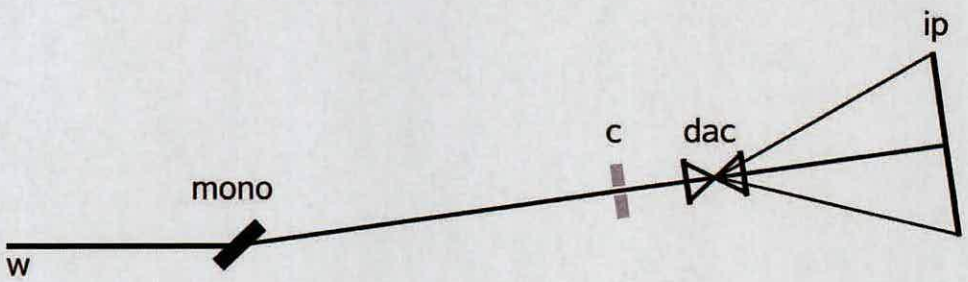

Figure 2.8 Schematic of Station 9.5 (mono refers to a monochromator, dac to an diamond-anvil cell, and ip refers to an image plate)

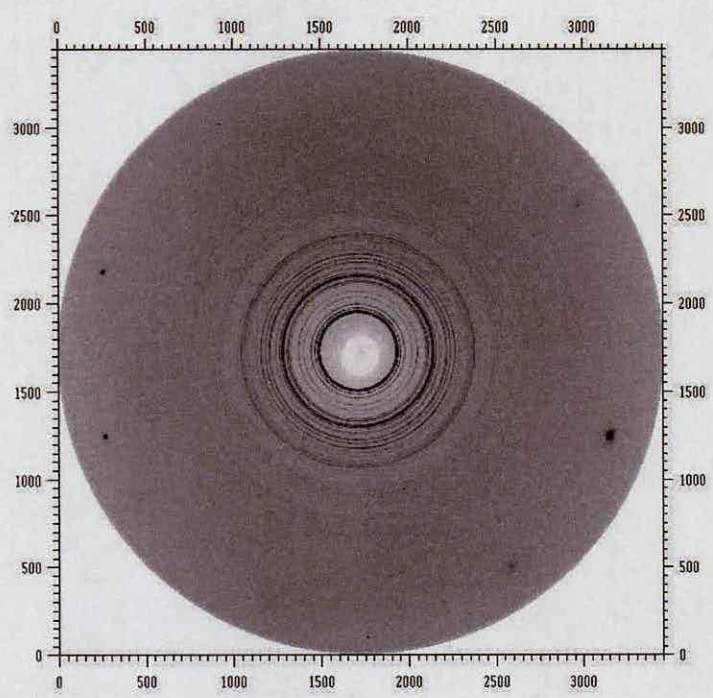

Figure 2.9 Powder pattern obtained from Station 9.5 using image plate

2.4.3 Sources of X-rays

Laboratory X-ray Sources

X-rays used in laboratory sources are generated using a sealed high-vacuum tube. A beam of electrons is accelerated at a flat plate of a very pure metal (anode). Molybdenum and copper are commonly used, but occasionally metals such as silver, iron or chromium are sometimes employed. X-rays are produced from the surface layers of the anode by two separate mechanisms. In the first way, the deceleration of the electrons by the field of the metal ions converts some of their energy into radiation. This radiation gives a continuous energy spectrum, which is termed "white" radiation. However, the more important radiation for use in diffraction is "characteristic radiation". This radiation occurs when the incoming beam causes the ionisation of electrons from atoms of the target material, in particular from the K-shell (principal quantum number $n = 1$). When an electron from a higher level (normally the L-shell, $n = 2$) falls back into the vacant K-shell, an X-ray photon of defined wavelength is emitted, corresponding to the energy difference between the two levels. Because of the selection rule for transitions between the K and L shells ($\Delta l = \pm 1$), a closely spaced double is seen, designated $K_{\alpha 1}$ and $K_{\alpha 2}$ radiation.

Since nearly all diffraction experiments are carried out with monochromatic radiation, the very strong K_α lines are normally employed, and it is essential to eliminate radiation of other wavelengths. The most common way of doing this is to use a single crystal monochromator. This consists of a single-crystal flake of quartz or graphite with an area of a few cm^3 oriented to the beam so that only the desired K_α line meets the condition for constructive interference. The scattered radiation thus becomes the "primary beam" for the actual diffraction experiment.

Synchrotron Radiation

X-rays can also be generated by sources known as synchrotron radiation facilities. In these installations electrons are accelerated at relativistic velocities along closed orbits of very large radii, often hundreds of metres. All synchrotron data in this work has been performed at the STFC Daresbury Laboratory.

It is well known that charged particles moving under the influence of an accelerating field emit electromagnetic radiation. The energy of this radiation is dependent on the velocity of the particle. Figure 2.10 shows the essentials of a synchrotron radiation source. The electrons are kept circulating within an evacuated cavity on a closed path (the ring) by a number of curved (bending) magnets. An extremely high vacuum is required in the ring cavity, to prevent electrons being lost by collision with the atoms present. Prior to injection into the ring, the particles are pre-accelerated first by a linear accelerator, and then by a booster (Figure 2.10). If the electrons are injected into the ring below the operating energy (usually 2-6 GeV), the machine is used as a true synchrotron, as a short period of acceleration is needed after injection to reach the operating energy. If the particles are injected at the operating energy, no acceleration is required, as the ring is used as a storage ring, where they can be kept circulating for periods of several hours. The radiation, which is emitted tangentially from the ring, has a continuous spectrum, from which a single wavelength of any value can be selected by monochromator.

As previously mentioned, only the characteristic lines of copper, molybdenum and a few other metals are sufficiently intense for crystallographic work, and thus with conventional sources, experiments are limited to only a discrete number of wavelengths. Experiments conducted using synchrotron radiations do not

suffer from this limitation. The possibility of selecting the wavelength for X-ray diffraction has far reaching consequences. For example, it can be used to enhance the resonant scattering effects on particular elements contained in the sample, e.g. to solve the phase problem by measuring anomalous dispersion effects, or to increase the scattering contrast between neighbouring atoms in the periodic table. Furthermore, crystal absorption and radiation damage are wavelength dependent and therefore can be minimized by optimizing the X-ray wavelength used.

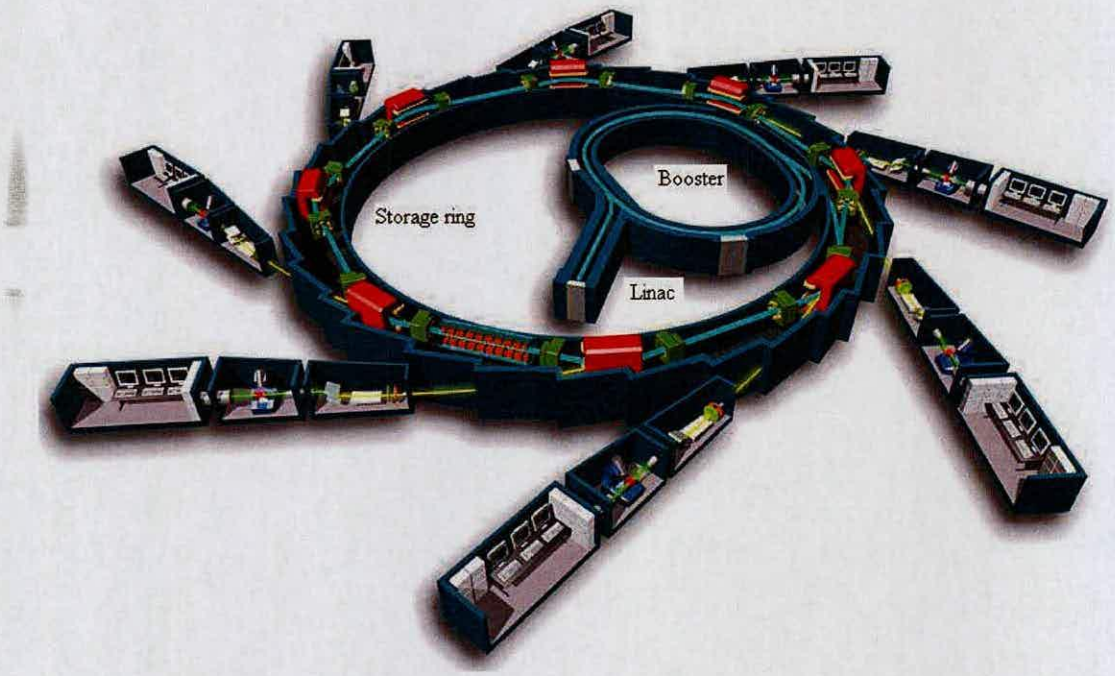

Figure 2.10 The production of synchrotron radiation from relativistic electrons in a particle accelerator

2.5 Neutron Diffraction

Neutrons can also be used to study materials by diffraction. The De Broglie equation relates the momentum, p, of a free particle to the wavelength of the corresponding quantum-mechanical wave representation as:

$$\lambda = \frac{h}{p} = \frac{h}{m_n v}$$

where h is Planck's constant, m is mass, and v is the thermal velocity. Thus neutrons with average thermal velocities of 2500 ms^{-1} will have a wavelength of 1.5 Å, and can therefore be used for diffraction.

As previously explained X-rays are scattered by the electrons of an atom. By contrast neutrons interact insignificantly with electron density when they pass through a crystalline solid and scattering instead occurs from the nuclei of atoms. Since both nuclei and neutrons are small, significant scattering occurs only when a neutron passes close to a nucleus, and thus on average the total intensity of diffraction of neutrons by a crystal is low compared to that of X-rays and therefore larger samples are required. An advantage of neutron scattering is that due to the point scattering from a nucleus the scattering factor does not fall off at higher angles unlike that for X-rays.

The main advantage of using neutron diffraction in this work is the ability of this method to locate hydrogen atoms. High-pressure X-ray diffraction studies cannot generally pinpoint hydrogen positions with any accuracy, due to the lack of electron density surrounding hydrogen atoms, and the limitations in sampling reciprocal space caused by the geometry of the DAC. This is not the case in neutron diffraction. In X-ray diffraction, the scattering power of an atom is directly

proportional to its atomic number. Neutron scattering powers, however, vary randomly across the periodic table, often with large differences between adjacent elements and isotopes. The atomic scattering factors for neutrons are effectively constants, (given as the scattering length, b_j^2) and there is considerable variation in b_j from element to element. As such, heavier elements do not dominate lighter ones as they do in X-ray diffraction. Thus neutron diffraction is far superior to X-ray for determination of hydrogen positions, especially for deuterated compounds. Not only is the neutron measurement more precise, because the H/D atoms scatter strongly, it is also more accurate, because it locates nuclei directly rather than the electron density distorted by valence effects. Hydrogen is a strong incoherent scatterer (phase of outgoing wave not determined by that of incident wave) and as a result the neutron diffraction pattern of a hydrogenous sample may have a low peak to background ratio that may partially obscure information from the reflection peaks. This problem is avoided by deuteration of a compound which gives a much improved background. In addition, since neutrons possess magnetic moments, they interact with magnetic ions, and can therefore be used to determine magnetic structure in materials.

2.5.1 Neutron Sources

High-energy neutrons are produced as a by product of a nuclear reaction, either in a reactor core or from a "spallation" source, where a high-energy proton beam from a synchrotron bombards a heavy metal such as tantalum. Protons hitting nuclei in the target material trigger an intranuclear cascade, placing individual nuclei into a highly excited state. The nuclei then release energy by neutrons some of which

will leave the target, while others go on to trigger further reactions. Each high energy proton delivered to the target results in the production of approximately 15 neutrons.

There are two ways of undertaking a neutron experiment. One way is to fix the wavelength of the neutrons and vary the detector angle (angle dispersive). The other method is to fix the detector angle, and vary the wavelength (wavelength dispersive).

Angle dispersive neutron diffraction requires neutrons from a reactor source, which are produce in effectively continuous time. The thermal neutron from a steady state reactor source can then be monochromatised, as for X-ray diffraction. Neutrons from a spallation source on the other hand, are pulsed, and a specific wavelength can be selected or analysed by time of flight (TOF) methods. All the neutron powder diffraction work presented in this thesis has been recorded using TOF neutron diffraction. In this method, the detector angle is fixed, and the powder pattern is obtained as a variable wavelength scan by time of flight. This can be derived as follows: neutrons travelling the distance L from the source, to the sample, and then to the detector, have a velocity equal to L/t, and a momentum of $m_n L/t$. Thus, Bragg's law may be reformulated in terms of TOF as:

$$\lambda = 2d\sin\theta = \frac{h}{p} = \frac{h}{m_n v} = \frac{ht}{m_n L} \Rightarrow t = \frac{2m_n L}{h} d\sin\theta$$

where, h is Planck's constant, m_n is the mass of a nuclei, d is d-spacing, L is the distance of the flight path, p is momentum, v is the thermal velocity, and t is time. Thus, if the total flightpath, scattering angle and time of flight are known, the d-spacings of the planes giving rise to a diffraction peak may be found. When banks of

detectors are used, the patterns can be summed, so long as they are all converted into d-spacings. The instrumental resolution function $\Delta d/d$ is given by:

$$\frac{\Delta d}{d} = \left[\left(\frac{\Delta t}{t} \right)^2 + (\Delta \cot \theta)^2 + \left(\frac{\Delta L}{L} \right)^2 \right]^{\frac{1}{2}}$$

Thus, higher resolution can be obtained by increasing the path length in order to minimise $\Delta t/t$. Finally, the time of flight data must be normalised with respect to the intensity distribution of the incident neutron pulse.

The high-pressure powder neutron diffraction experiments presented in this thesis were performed at the ISIS Neutron Facility, Rutherford Appleton Laboratory, UK, on the PEARL HiPr beamline, using the 2θ = 90° detectors of the PEARL diffractometer with a 'transverse' (through-anvil) scattering geometry.

The high-temperature studies were also performed at ISIS Neutron Facility, on the High Resolution Powder Diffractometer (HRPD), which provides the highest resolution of any neutron diffractometer currently available. This is because the total path length is 100 metres long.

2.6 References

[1] L. Merrill, W. A. Bassett, *Rev. Sci. Instrum.*, 1974, **45**, 290.

[2] A. Dawson, *PhD Thesis*, The University of Edinburgh, 2003.

[3] A. J. Davidson, D. Francis, W. G. Marshall, C. R. Pulham, unpublished results, 2006.

[4] R. A. Forman, G. J. Piermarnini, J. D. Barnett, and S. Block, *Science.*, 1972, **176**, 892.

[5] G. J. Piermarini, S. Block, J. D. Barnett, R. A. Forman, *J. Appl. Phys.*, 1975, **46**, 2774.

[6] J. M. Besson, R. J. Nelmes, G. Hamel, J. S. Loveday, G. Weill, S. Hull, *Physica B.*, 1992, **180–181**, 907.

[7] W. G. Marshall and D. Francis, *J. Appl. Crystallogr.*, 2002, **35**, 122.

[8] D. L. Decker, *J. Appl. Phys.*, 1971, **42**, 3239.

[9] K. P. Thakur, *J. Appl. Phys.*, 1978, **16**, 201.

[10] E. Smith, G. Dent, *Modern Raman Spectroscopy: A Modern Approach*, John Wiley and Sons, Hoboken, USA. 2005

[11] W. Massa, *Crystal Structure Determination*, Springer-Verlag, Berlin, Germany. 2000

[12] C. Giacovazzo, H. L. Monaco, D. Viterbo, F. Scordardi, G. Gilli, G. Zanotti, M. Catti, *Fundamentals of Crystallography*, Oxford Univeristy Press, Oxford, UK, 1992

[13] A. Dawson, D. R. Allan, S. Parsons, M. Ruf, *J. Appl. Crystallogr.*, 2004, **37**, 410.

[14] Bruker AXS, APEX 2. Bruker-AXS, Madison, Wisconsin, USA. 2006

[15] Bruker AXS, SAINT, Version 7.01A, Bruker-AXS, Madison, Wisconsin (USA), 2003.

[16] S. Parsons, SHADE. The University of Edinburgh (Scotland), 2004.

[17] G. M. Sheldrick, SADABS, version 2004/1, University of Göttingen (Germany), 2004.

[18] R. H. Blessing, *Acta Cryst.*, *B***51**, 33

[19] L. J. Farrugia, *J. Appl. Cryst.*, **32**, 837

[20] G. M. Sheldrick, SHELXS, Bruker-AXS, Madison, Wisonsin, USA, 1997.

[21] A. Altomare, A., G. Cascarano, C. Giacovazzo, A. Guagliardi, *J. Appl. Cryst.*, 1993, **26**,343.

[22] M. C. Burla, M. Camalli, B. Carrozzini, G. L. Cascarano, C. Giacovazzo, G. Polidori, R. Spagna, *J. Appl. Cryst.*, 2003, **36**, 1103.

[23] V. Favre-Nicolin, R. Cerny, *J. Appl. Cryst.*, 2002, **35**, 734.

[24] W. I. F. David, K. Shankland, L. B. McCusker, C. Baerlocher., *Structure determination from powder diffraction data*. IUCr Monographs on Crystallography, vol **13**, OUP, Oxford.

[25] W. I. F. David, K. Shankland, N. Shankland, *Chem. Commun.*, 1998, 931.

[26] P.W. Betteridge J. R. Carruthers, R. I. Cooper, C. K. Prout, D. J. Watkin, *J. Appl. Cryst.*, 2003, **36**, 1487.

[27] A. R. Lennie, D. Laundry, M. A. Roberts, G. Bushnell-Wye, *J. Synchrotron Radiation.*, 2007, **14**, 433.

Chapter 3

High-Pressure Studies of Explosive Materials: RDX and HMX

Alistair J. Davidson, Iain D. H. Oswald, Duncan J. Francis, Alistair R. Lennie, William G. Marshall, David I. A. Millar, Colin R. Pulham, John E. Warren, and Adam S. Cumming. **Explosives under pressure – the crystal structure of γ-RDX determined by high-pressure X-ray and neutron diffraction**, CrystEngComm, 2008, 10, 162–165

Chapter Three: High-Pressure Studies of Explosive Materials: RDX and HMX

3.1 Introduction

This work has focused on the high-pressure behaviour, polymorphism and solvate formation of cyclotrimethylenetrinitramine (RDX or cyclonite) and cyclotetramethylenetetranitramine (HMX or octogen). RDX and HMX are powerful yet relatively insensitive energetic materials, which are classified as secondary explosives (Figure 3.1). Both compounds are relatively insensitive to initiation by heat, friction and shock [1].

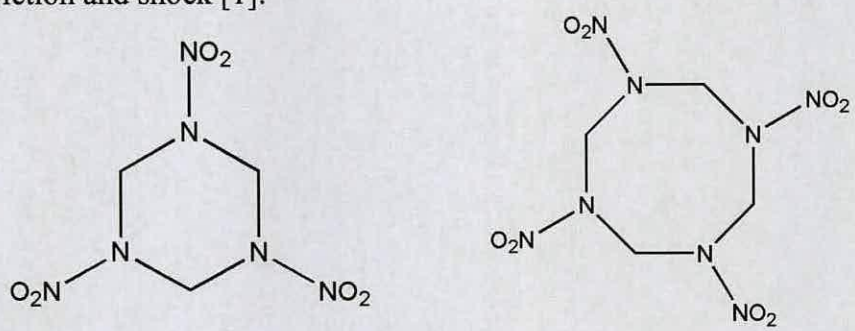

Figure 3.1. Molecular structures of RDX and HMX

3.1.1 RDX

The enhanced chemical and thermal stability of RDX led to it attaining importance as a military explosive during World War II. RDX is now a widely used explosive that when compounded with mineral jelly and polymers forms plastic explosives such as C4 [1]. Pure RDX is sensitive to initiation by impact and friction although it is desensitised by coating the crystals with wax, oil or grease [1]. Insensitive explosives may be created by embedding the RDX crystals in synthetic rubbers or polymeric matrices.

Two polymorphic forms of RDX are known, designated α and β [2]. The structure of α-RDX has been determined by single crystal neutron diffraction [3]. The structure of β-RDX has not been determined because of the difficulty of obtaining and preserving well formed crystals, even for short periods, owing to its extreme instability under ambient conditions.

As described in Chapter One, there has been significant interest in the high-pressure behaviour of RDX. The optical and infrared spectra of RDX have been obtained up to pressures of 65 GPa. Colour changes were observed which were suggested to be a result of a decrease in the HOMO-LUMO band gap [4]. Molecular simulations of RDX have been conducted investigating the effects of pressure on the lattice parameters and volume up to 3.95 GPa [5]. High-pressure studies have been performed using a diamond-anvil cell (DAC), and it is well known that a phase transition occurs at approximately 4 GPa at room temperature, with a corresponding change in volume of 1.6 % [6]. This high pressure phase is designated form-γ. Equations of state for both the α- and γ-forms have been reported based on high-pressure X-ray powder diffraction measurements. More recently several spectroscopic studies have been undertaken in an attempt to shed light on the structure of the γ-form. High-pressure experiments up to 15 GPa using Raman spectroscopy have proposed that the α → γ transition leads to a rearrangement of the RDX molecules, which in turn significantly changes the intermolecular interaction experienced by the N-O bonds [7]. A further direct compression study using Raman and far-IR spectroscopy up to pressures of 26 GPa, has presented evidence for a new δ-phase formed between pressures of 17.8 and 18.8 GPa [8]. The presence of this

new form was proposed based on the appearance of new vibrational bands and associated changes in intensity patterns.

A structure of the γ-form has recently been proposed using a combination of infrared spectroscopy and powder X-ray diffraction [9]. The authors suggested the space group *Pbca* and used the Rietveld method to fit their X-ray data to a series of models with the nitro groups in different conformations. The authors reported that the most likely molecular conformation had the same conformation as the α-form, but that the N-NO_2 torsion angle had changed slightly.

3.1.2 HMX

HMX was first prepared in 1930, and it is now almost exclusively used in military applications, in the form of a polymer-bonded explosive. The stability of HMX to both temperature and chemical decomposition is superior to that of RDX although its explosive power is somewhat less than RDX [1].

As described in Chapter One, HMX provides an excellent example of the importance of polymorphism in energetic materials. Three polymorphs of HMX have been identified and characterised (α, β, and δ) [1]. Investigations have shown that the sensitivities to impact follow the order δ > α > β – and so the risk of accidental detonation of the δ, and α-forms means that only β-HMX is permitted in munitions used by the British armed forces. The unit cell parameters for the polymorphs of both RDX and HMX are given in Table 3.1.

	α-HMX [11]	β-HMX [11]	δ-HMX[11]	α-RDX [2]
Crystal System	orthorhombic	monoclinic	hexagonal	orthorhombic
Space group	*Fdd*2	$P2_1/c$	$P6_1$	*Pbca*
***a*/Å**	15.14	6.54	7.711(2)	13.182(2)
***b*/Å**	23.89	11.05	7.711(2)	11.574(2)
***c*/Å**	5.913	7.37	32.553(6)	10.709(2)
α/°	90	90	90	90
β/°	90	102.8	90	90
γ/°	90	90	120	90
***V*/Å^3**	2138.7	519.387	1676.27(5)	1633.86(4)
Z	8	2	6	8
***D*$_c$/g cm^{-3}**	1.84	1.90	1.80	1.82
T/K	150	150	150(2)	150(2)

Table 3.1. Unit cell parameters for known polymorphs of HMX and RDX

The ability of HMX to form hydrates and solvates with organic solvents has been widely studied. HMX has been reported to co-crystallise with nearly one hundred organic molecules [11,12]. The most well know is the γ-form of HMX, which is a hemihydrate (Table 3.2). Solvates of HMX with DMF (1:1) (N-N-dimethylformamide) [13], DMSO (dimethyl sulfoxide) (1:2) [14] and NMP (1:1) (N-Methyl-2-pyrrolidinone) [15] have been reported. The HMX-DMF and HMX-NMP solvates have been structurally characterised, but no structural data are available for the HMX-DMSO solvate. Interest in this area has been fuelled by the need for information about the intermolecular interactions in the solid, which might be important in terms of its stability and decomposition routes. The structures of these and any novel solvates would extend the understanding about the most important intermolecular interactions in the solid phase. This would also provide insight into how guest solvent molecules interact with the host structure. For example, the

chemical and physical properties of HMX might be tailored by incorporation of guest molecules.

There has also been considerable interest in the variable temperature and pressure behaviour of HMX. A transition from the β-form of HMX to the δ-form is observed at 431 K on heating at atmospheric pressure. This β → δ transition is typically associated with the thermal decomposition of HMX [16,17]. The stability to pressure of each polymorph of HMX has been studied using Raman and infrared spectroscopy [18]. The observed behaviour of the polymorphic forms is as follows: β-HMX is stable up to 5.4 GPa, and the α-form is stable up to 4.2 GPa. γ-HMX converts to β-HMX at 0.55 GPa. δ-HMX converts to a mixture of α- and β-forms at pressures below 0.05 GPa. Further studies have shown that the β-form is stable up to 10.0 GPa [19]. More recent studies using Raman spectroscopy and angle-resolved X-ray diffraction studies have been conducted under both hydrostatic and non-hydrostatic conditions. The results show that the high-pressure behaviour of β-HMX depends upon the stress conditions. HMX is more compressible under hydrostatic conditions than under non-hydrostatic conditions [20]. The hydrostatic studies have also suggested a conformational transition of β-HMX at 12 GPa, with no apparent change in volume, and a further discontinuous transition at 27 GPa with a 4% volume change. At 40 GPa, the *b*- and *c*-axes become nearly identical with the structure adopting a nearly close-packed structure. Theoretical studies have also been performed on the hydrostatic compression of HMX, and have investigated the changes in lattice parameters and volume [5]. The deflagration rate of a powdered sample of HMX has been studied between 0.7 and 35 GPa. An increase in the rate was observed above 10 GPa [19]. Theoretical experiments have been used to

determine rate laws and decomposition mechanisms under detonation conditions [21]. These showed that the rate of water formation is much faster than the rate of formation of N_2, reflecting the more complex mechanism associated with the formation of N_2.

	γ-HMX [10] hemihydrate	1:1 HMX-DMF[13]	1:1 HMX-NMP[15]
Crystal System	monoclinic	monoclinic	hexagonal
Space group	*Pc*	*C2/c*	*R3c*
***a*/Å**	10.95	22.627(10)	16.607(4)
***b*/Å**	7.93	16.000(4)	31.506(8)
***c*/Å**	14.61	13.849(6)	31.506(8)
α/°	90	90	90
β/°	119.4	114.09(3)	90
γ/°	90	90	120
***V*/Å^3**	1268.637	4577.0(3)	7525.2(38)
Z	4	12	18
***D*$_c$/g cm^{-3}**	1.76	1.607	1.570
T/K	150	298(2)	298(2)

Table 3.2. Unit cell parameters for structurally characterised hydrates and solvates of HMX.

3.2 Experimental

Crystalline samples of RDX and HMX (SME type II; 100-300 μm) were kindly provided by W. G. Proud and H. Czerski (Cavendish Laboratory, University of Cambridge).

Deuteration of RDX and HMX were performed by Mr David Millar, (School of Chemistry, University of Edinburgh) following the preparation given by Bulusu *et al* [22]. A mixture of deuterated HMX: RDX was prepared from deuterated

paraformaldehyde and deuterated ammonia in a two-step synthesis, which is outlined in Scheme 3.1.

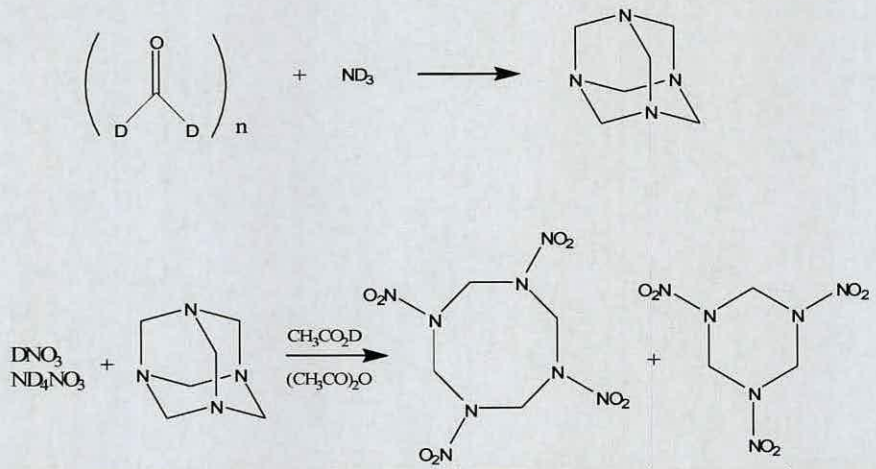

Scheme 3.1: The two-step synthesis of HMX and RDX. Hexamethylenetetramine prepared from paraformaldehyde and ammonia was nitrated by nitric acid and ammonium nitrate. This resulted in a mixture of HMX and RDX.

The reaction between paraformaldehyde and ammonia gave hexamethylenetetramine (hexamine), which was subsequently nitrated by concentrated nitric acid and ammonium nitrate in a complex multi-step mechanism. Deuterated ammonia, ND_3 (Sigma-Aldrich; 99.9 at %), was bubbled into a solution of paraformaldehyde-d_2 [$(CD_2O]_n$, 3.28 g) in D_2O (5 cm^3) until the solution was saturated. The solvent was removed by heating and evaporation at ambient pressure. Recrystallisation by azeotropic distillation with benzene then gave pure hexamine-d_{12} in 73% yield (2.00 g ; m.p. 262 °C decomp., lit. m.p. 263 °C decomp). The next step in the procedure was nitrolysis of hexamine-d_{12}. A mixture of glacial acetic acid (CH_3CO_2D, 15 cm^3), acetic anhydride (0.25 cm^3) and paraformaldehyde-d_2 (0.35 g) was maintained at 44 °C in a vessel fitted with three glass syringes. The following solutions were then added to this mixture simultaneously and uniformly over a period of 15 minutes: (a) hexamine (2.00 g) in CH_3COOD (3.35 cm^3); (b)

$(CH_3CO)_2O$ (5.5 cm^3); and (c) the nitrolysis mixture of DNO_3 (98 – 100 %, 1.89 g) and ND_4NO_3 (99 %, 1.65 g). After stirring for 15 minutes, additional portions of $(CD_3CO)_2O$ (9.0 cm^3) and the nitrolysis mixture (DNO_3, 2.85 g; ND_4NO_3 2.63 g) were subsequently added simultaneously and uniformly. The reaction mixture was stirred at 44 °C for one hour before dilution with D_2O and subsequent heating under reflux for 30 minutes. Addition of 50 g frozen D_2O precipitated the crude product which was then collected, washed with cold H_2O and allowed to dry. This gave 3.5 g of a mixture of HMX and RDX. The crude mixture was stirred in 1,1-dichloroethane (300 cm^3) in order to dissolve the more soluble RDX. After filtration, the white solid was recrystallised from acetone to give colourless crystals (3.2 g, m.p. 275 °C, lit. m.p. 276 – 277 °C). The RDX was then recovered from the dichloroethane extract before recrystallisation from 50 % aqueous acetone yielded the fraction in pure form (0.03 g, m.p. 195 °C, lit. m.p. 205 °C). In order to increase the yield of RDX, a second preparation was undertaken which involved performing the nitration at a higher temp of 55°C [22]. The RDX fraction was then precipitated with cold water before recrystallisation with acetone gave the pure solid.

3.2.1 High-Pressure Powder Neutron Studies

Neutron powder diffraction data were collected using the high flux, medium-resolution time-of-flight diffractometer, HiPr, on the PEARL beamline at the ISIS Neutron Facility, Rutherford Appleton Laboratory. High pressures for neutron powder diffraction were generated using a Paris–Edinburgh cell [23]. A lightly ground sample of RDX (*ca.* 100 mg) was loaded into an encapsulated TiZr gasket [24] with a pressure transmitting medium of 4:1 methanol:ethanol. Pressures were

determined from the well defined equation of state of lead [25]. Data were collected using the $2\theta = 90^{\circ}$ detectors with a transverse (through-anvil) scattering geometry. Suitable safety precautions were undertaken, involving face shield, Kevlar arm shields and gloves. All sample loading procedures were performed behind a blast screen. Data analysis was performed by use of the Rietveld method using The General Structure Analysis System (GSAS) suite of programs [26].

3.2.2 High-Pressure Single-Crystal X-Ray Studies

High pressures for single-crystal X-ray diffraction were generated using a Merrill-Bassett diamond anvil cell (DAC) [27] equipped with 600 μm culet diamonds and a tungsten gasket. A single-crystal and small ruby chip were loaded into the DAC, together with 4:1 methanol:ethanol pressure-transmitting medium. The pressure applied to the sample was determined by the ruby fluorescence method [28] using a 632.8 nm excitation line from a He-Ne laser. The fluorescence was detected by a Jobin-Yvon LabRam 300. High-pressure data sets were collected using ω-scans in 12 settings of 2θ and φ with step size 0.3° for 30 s [29].

High-pressure single crystal studies on samples of non-deuterated RDX were performed at the STFC Daresbury Laboratory on Station 9.8 ($\lambda = 0.6765$ Å) using a Bruker APEX 2 diffractometer. High pressure data on HMX were recorded at Station 16.2 using synchrotron radiation, with wavelength of 0.82520 Å.

All single-crystal data sets were processed according to the procedure described by Dawson *et* al [30]. Integration of data sets and global cell refinement were carried out using the program SAINT [31], in which 'dynamic masks' were used in order to prevent integration of areas of the detector shaded by the body of the

DAC. An analytical correction for the absorption by the DAC component was then applied using SHADE [32] and an absorption correction for the crystal was applied using SADABS [33]. All structures were solved by direct methods using SIR92 [34] and full-matrix least-squares-refinement against $|F|^2$ were performed using the program CRYSTALS [35].

3.3 Results and Discussion: RDX

3.3.1 Structure of α-RDX

α-RDX crystallises in an orthorhombic crystal system, space group *Pbca*, with eight molecules per unit cell [36, 37] The unit cell parameters are given in Table 3.1. The molecules in the α-form exhibit a chair conformation (Figure 3.2). The substituent nitro-groups adopt both axial and equatorial positions. The groups involving N5 and N6 are designated axial and the group involving N4 is designated equatorial. Thus, the molecular conformation in the α-form has been denoted AAE [9]. The crystal structure of α-RDX is shown in Figure 3.3. It comprises of zig-zagging planes of RDX molecules running approximately parallel to the *a*-axis.

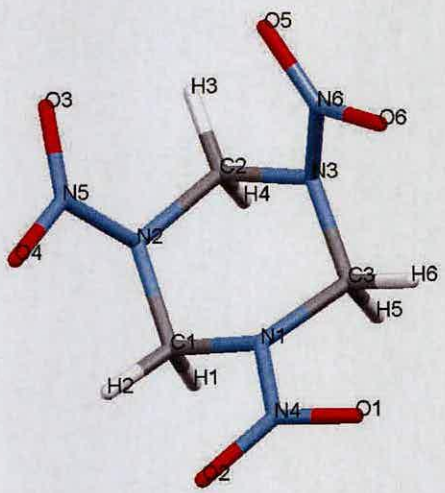

Figure 3.2. Molecular structure with numbering scheme of α-RDX

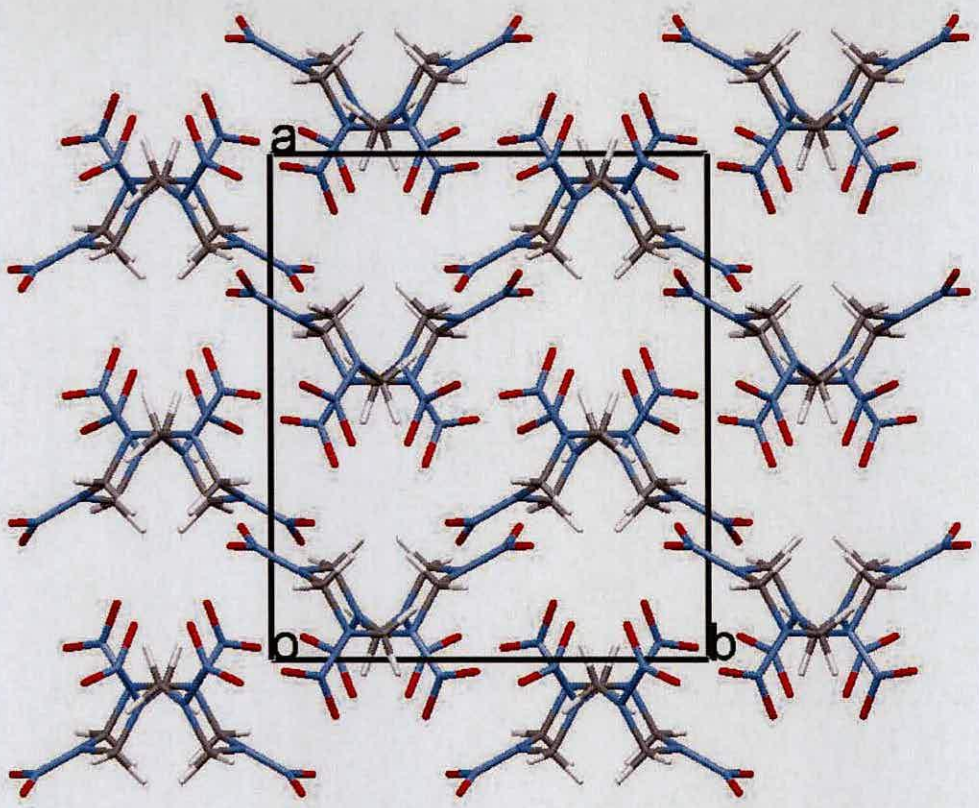

Figure 3.3. Crystal structure of α-RDX viewed down the *c*-axis

3.3.2 High-Pressure Powder Neutron Studies

Figure 3.4 shows the powder neutron diffraction patterns collected at incremental steps between 0.01GPa and 7.99 GPa. Inspection of the 0.01 GPa powder pattern confirmed the presence of the α-form of RDX. Rietveld refinement of all powder patterns was possible up to pressures of 3.85 GPa. The lattice parameters are given in Table 3.3. Over this pressure range, no significant changes were observed in the orientations of the nitro groups relative to the ring, or in any of the primary bond lengths and angles of the molecule.

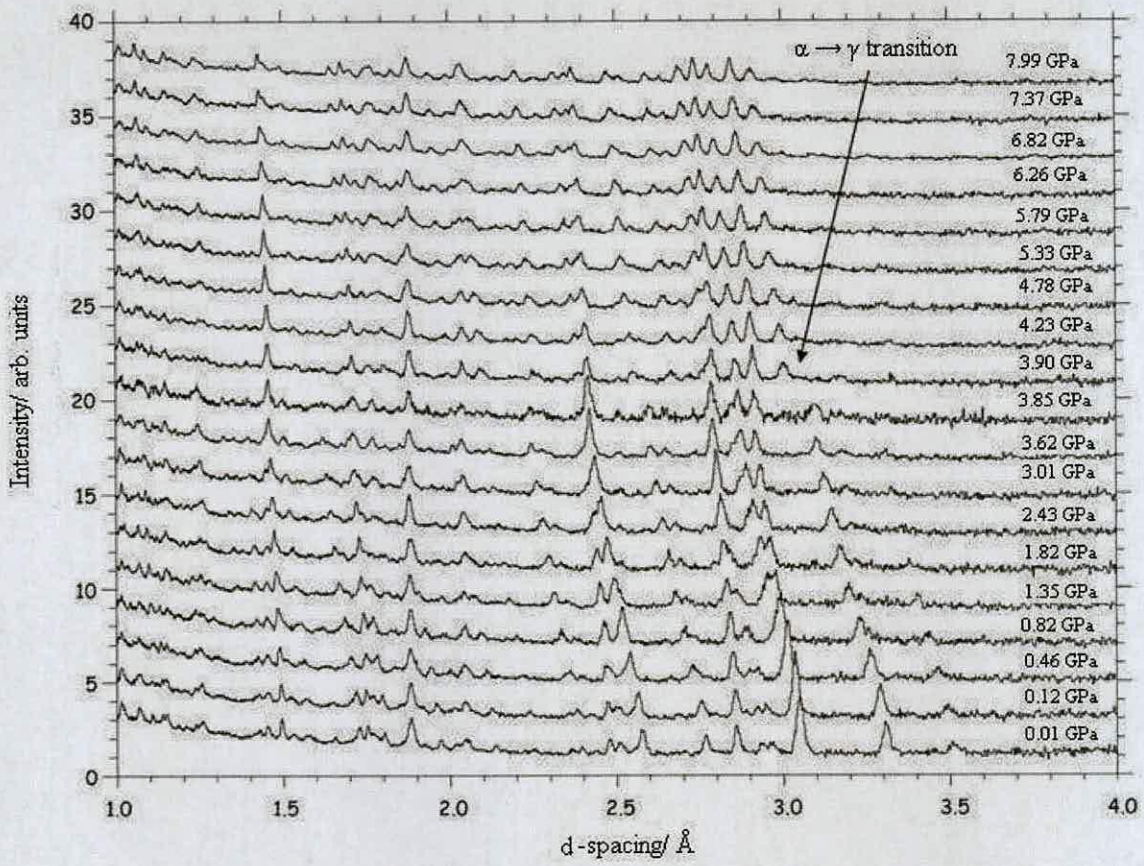

Figure 3.4. Neutron powder patterns of α-RDX-d_6 with increasing pressure.

P (GPa)	*a*(Å)	*b*(Å)	*c*(Å)	V(Å^3)
0.00	13.1920(2)	11.6020(2)	10.7230(2)	1641.10(3)
0.12	13.1530(2)	11.5420(2)	10.6630(2)	1618.90(3)
0.46	13.0750(2)	11.4520(2)	10.5530(2)	1580.00(2)
0.82	13.0080(2)	11.3510(3)	10.4540(2)	1543.60(2)
1.35	12.9300(2)	11.2480(3)	10.3460(2)	1504.80(3)
1.82	12.8680(2)	11.1660(2)	10.2640(2)	1474.80(3)
2.43	12.8090(2)	11.0801(2)	10.1810(2)	1445.00(3)
3.01	12.7540(2)	11.0050(2)	10.1040(1)	1418.20(2)
3.62	12.7030(2)	10.9380(2)	10.0320(2)	1394.00(2)
3.85	12.6860(2)	10.9120(3)	10.0130(2)	1386.20(2)

Table 3.3 Unit cell parameters for α-RDX with increasing pressure.

The most significant changes were seen in the C-D...O-N, N...O, and N...N intermolecular contacts. These are listed in Table 3.4, which displays intermolecular contacts present in α-RDX at 0.01 and 3.85 GPa.

	0.01 GPa	3.85 GPa
D1...O1	3.040(5)	2.721(5)
D1...O2	2.671(7)	2.368(6)
D1...O3	2.802(5)	2.651(5)
D2...O1	2.622(5)	2.180(4)
D3...O6	3.008(8)	2.855(7)
D4...O6	2.558(4)	2.392(6)
D4...O1	2.512(4)	2.467(4)
D4...O2	2.666(4)	2.294(3)
D4...O4	2.558(6)	2.390(4)
D5...O1	2.763(7)	2.387(5)
D5...O2	3.080(5)	2.895(5)
D5...O5	2.476(5)	2.252(4)
D6...O2	2.572(4)	2.346(4)
N3...N5	3.011(5)	2.663(5)
N4...O3	2.985(4)	2.697(4)
N5...O4	2.962(6)	2.878(5)
N6...O5	3.027(5)	2.778(5)

Table 3.4 Intermolecular contacts of α-RDX at 0.01 and 3.85 GPa. All distances in Å.

Table 3.4 reveals significant shortening of all intermolecular contacts over this pressure range. It can also be seen that the C-D...O-N interactions vary by the largest amount, for example the D2...O1 interaction decreases by over 0.4 Å between 0.01 and 3.85 GPa. The variation of lattice parameters over the same pressure range is shown in Figure 3.5, where it can be observed that the *c*-axis decreases by 6.6 % between 0.01 and 3.85 GPa compared to a decrease of 3.8 % and 6.0 % for the *a*- and *b*- axes, over the same pressure range.

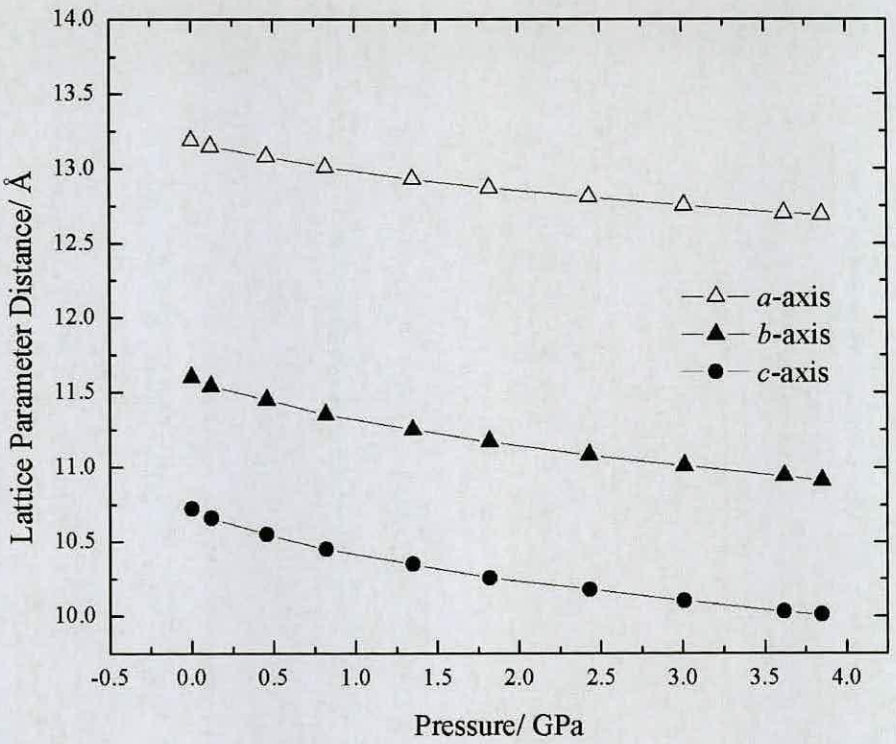

Figure 3.5 Variation of lattice parameters of α-RDX with increasing pressure.

On increasing the pressure to 3.90 GPa, new peaks were observed to appear in the diffraction pattern. Indexing of this pattern confirmed the presence of the γ-phase, previously identified by Goto *et al.* [9]. Attempts to refine this pattern using their proposed structure in space group *Pbca* proved unsuccessful. After many attempts to fit the data, it became apparent that the space group was incorrect. The assignment of space group can often be a complex problem in high-pressure powder neutron diffraction studies, particularly for such a complex system, where not only is resolution sacrificed for higher flux, but the constraints of the sample environment restrict the range of *d*-spacings that can be accessed.

For this reason, single-crystal X-ray diffraction studies were performed with the expectation that a single-crystal might survive the transition without

disintegration. Support for this came from the small volume change reported over the α → γ transition [6] and the fact that previous optical studies had suggested that the hydrostatic compression of a single crystal of RDX through the α → γ transition did not result in the destruction of the crystal [4].

3.3.3 High-Pressure Single-Crystal X-Ray Studies

A single-crystal of RDX was loaded into a DAC with a pressure-transmitting medium of 4:1 methanol:ethanol. The cell was initially pressurised to *ca.* 0.1 GPa. Indexing of the reflections from the single-crystal X-ray diffraction experiment confirmed the known orthorhombic α-phase of RDX. The pressure in the cell was then increased to 5.2 GPa. Indexing of the reflections identified an orthorhombic unit cell, space group $Pca2_1$ with lattice parameters, a = 12.5650 (19) Å, b = 9.4769(6) Å, c = 10.9297(9) Å. As a result of the limitations caused by shading from the steel body of the diamond-anvil cell, high-pressure data-sets are frequently incomplete (in this case 73% complete) compared with data-sets recorded at ambient pressure. These factors combined to make structure solution particularly challenging and all attempts using direct methods were unsuccessful. Attempts were made using direct space methods to solve the structure. Global optimisation methods require a number of different input files. These include a merged reflection file, an instructions file (containing all the unit cell information) and a Z-matrix for the compound (the molecular geometry). The space group $Pca2_1$ combined with the expected density, required two independent molecules in the asymmetric unit and so two Z-matrices were input into the program FOX [38]. FOX allows a great deal of flexibility in the molecules, and this was important because there was a suspicion

that the conformations of the molecule had changed during the phase transition. After approximately one hour running on a standard PC, a possible solution was obtained. Subsequent full-matrix least-squares structure refinement of the X-ray data proved to be possible.

Further support that this was the correct structure was provided by using the X-ray structure as a model to refine the neutron powder diffraction patterns. Figure 3.6 shows the Rietveld plot for γ-RDX at 3.90 GPa (χ^2 = 1.137, wRp = 0.0268). Structural refinement was possible for all subsequent neutron powder patterns up to 7.99 GPa. Unit cell parameters for γ-RDX with increasing pressure are given in Table 3.5.

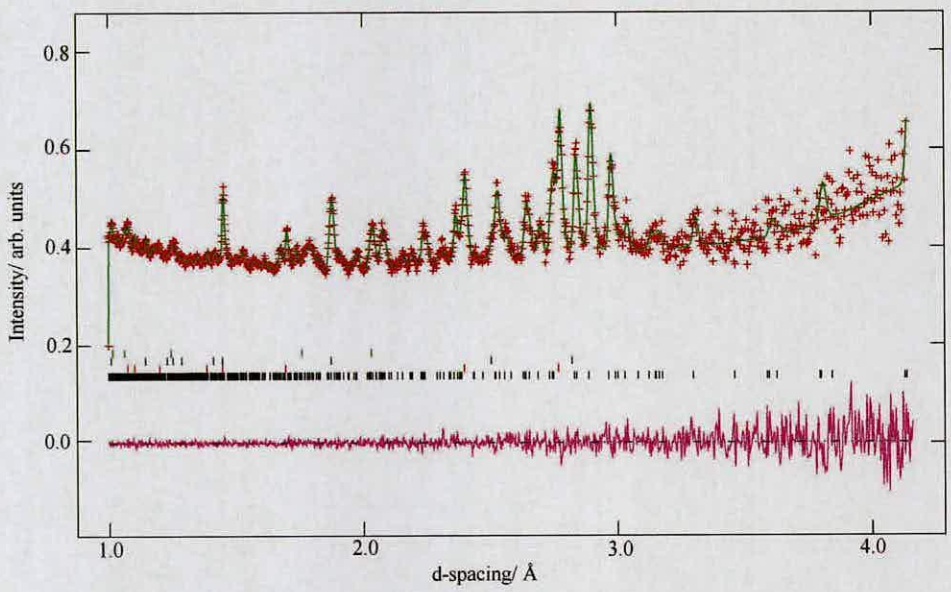

Figure 3.6. Neutron powder patterns of γ-RDX at 3.90 GPa. The crosses denote the observed intensities and the solid lines those calculated from the best-fit model of the Rietveld refinement. The tick marks represent the calculated peak positions, (black tick marks signify RDX, the red marks correspond to the lead internal pressure marker, and the blue and green tick marks represent tungsten carbide and nickel, respectively). The line below them represents the deviation between observed and calculated intensities.

P (GPa)	*a*(Å)	*b*(Å)	*c*(Å)	*V*(Å3)
3.90	12.6961(2)	9.6507(2)	11.0830(3)	1357.90(3)
4.23	12.6684(1)	9.6095(1)	11.0505(2)	1345.26(2)
4.78	12.6317(2)	9.5549(2)	11.0037(2)	1328.09(2)
5.33	12.5961(2)	9.5064(2)	10.9643(3)	1312.90(2)
5.79	12.5625(1)	9.4700(2)	10.9292(3)	1299.85(3)
6.26	12.5347(2)	9.4328(2)	10.8977(3)	1288.50(3)
6.82	12.5022(2)	9.4019(2)	10.8522(2)	1275.60(3)
7.37	12.4729(2)	9.3661(2)	10.8259(3)	1264.70(3)
7.99	12.4378(1)	9.3315(1)	10.7888(2)	1252.19(3)

Table 3.5 Unit cell parameters of γ-RDX with increasing pressure.

3.3.4 Structure of γ-RDX

The γ-phase of RDX contains two independent molecules in the asymmetric unit (Figures 3.7), and hence eight molecules per unit cell. The unit cell parameters for α-RDX and γ-RDX are listed in Table 3.6.

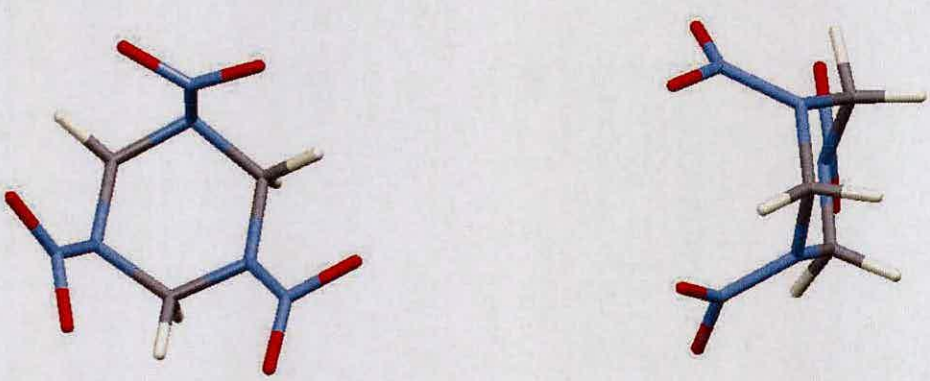

Figure 3.7. Molecular structure of γ-RDX

	α-RDX at 3.85 GPa	γ-RDX at 3.90 GPa
Crystal System	orthorhombic	orthorhombic
Space group	*Pbca*	$Pca2_1$
***a*/Å**	12.6863(26)	12.6319(15)
***b*/Å**	10.9124(30)	9.5554(10)
***c*/Å**	10.0130(22)	11.0030(22)
α/°	90	90
β/°	90	90
γ/°	90	90
***V*/Å^3**	1386.2(4)	1328.17(23)
Z	8	8
***D*$_c$/g cm^{-3}**	2.130	2.267
T/K	293(2)	293(2)

Table 3.6. Unit cell parameters for α- and γ-RDX

Figure 3.8 compares the conformation of the two molecules of γ-RDX. Both RDX molecules in the γ-form retain the chair conformation of the six-membered ring.

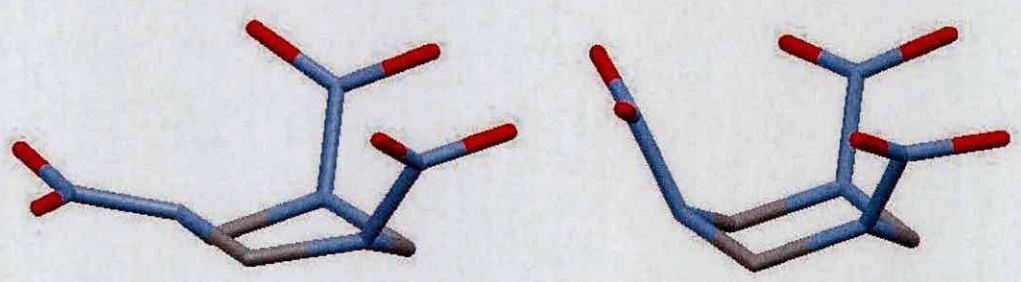

1 **2**

Figure 3.8. Molecular structure of two independent RDX molecules in the asymmetric unit of γ-RDX. Hydrogen atoms omitted for clarity.

The orientations of the nitro groups can be compared by reference to the angle δ, which is defined as the angle between the plane of the C-N-C ring and the corresponding N-N bond (Figure 3.9)

Table 3.7 shows the values of δ for the molecule in both crystalline forms, and for a range of conformations calculated using DFT methods [40]. The AAA-AAE (TS-1) conformation represents the transition state between AAA and AAE conformations, i.e. one of the nitro-groups lies midway between the axial and equatorial positions. Neither of the conformations in γ-RDX corresponds to any of the conformations observed in the calculated structures or in the α-form.

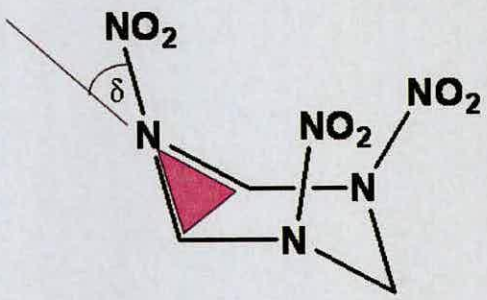

Figure 3.9 Schematic showing the angle, δ, between the plane of the C-N-C ring and the corresponding N-N bond

The molecule denoted 1 in Figure 3.8 lies closest to the TS-1 (AAA-AAE) conformation, so could be designated AAI, where I represents an intermediate orientation of the nitro-group. Molecule 2 tends towards the AAA conformation, since all the δ angles are positive. Based on the results of the calculations, such a variability in the conformation is perhaps not unexpected, since relative to the AAE conformation, the AAA and AAA-AAE (TS-1) conformations are only higher in energy by 1.21 and 3.43 kJ mol^{-1}, respectively.

α-form	γ-form (molecule 1)	γ-form (molecule 2)	AAA[33]	AAE[33]	AAA-AAE[33] (TS-1)
33.4	39.6	39.6	30.3	34.0	34.1
33.9	17.3	17.3	30.1	34.0	33.8
-19.8	-2.4	9.5	29.9	-37.9	1.5

Table 3.7 Values of δ (in °) for different conformations of RDX [33]

A point to note is that there is no significant change in the primary bond lengths (for example the C-C, N-C, N-N, N-O, and C-H bond lengths) between the two phases of RDX.

The presence of two molecular conformations allows for more efficient packing of molecules in γ-RDX. For example, a projection down the *a*-axis (Figure 3.10a) shows alternating AAA and AAI RDX molecules running parallel to the *c*-axis; AAI at $b = 0,1$ etc, and AAA at $b = 1/2, 3/2$ etc. This can be observed more clearly in Figure 3.10b, where molecules are coloured by symmetry equivalence, AAA molecules shown in blue, AAI molecules given in green.

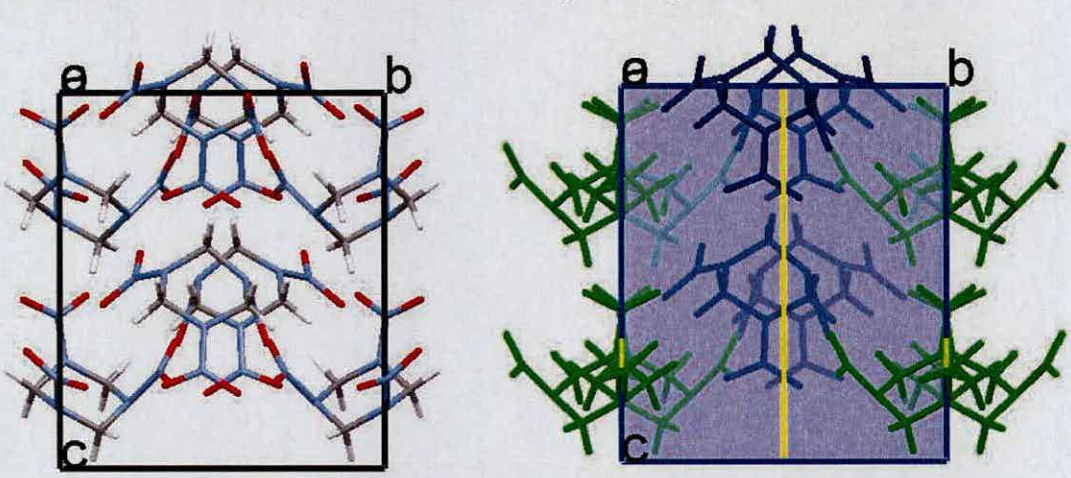

a b

Figure 3.10. (a). γ-RDX viewed down the *a*-axis, (b). γ-RDX viewed down the *a*-axis showing symmetry elements, with molecules coloured by symmetry equivalent (blue = AAA, green = AAI).

Figure 3.11 shows the orientations of two adjacent AAA and AAI molecules in the unit cell, illustrating how each molecule effectively "cups" one of the nitro-groups of the other molecule. This interlocking of adjacent molecules allows a more efficient packing of the molecules in γ-RDX compared to α-RDX.

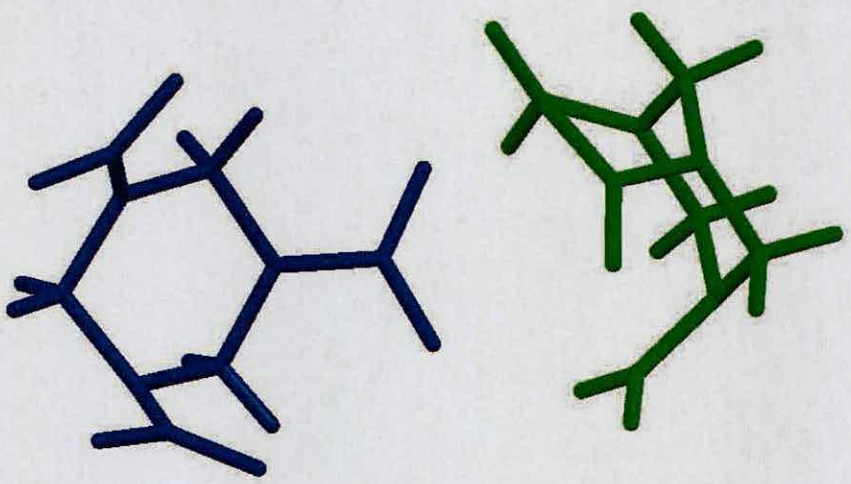

Figure 3.11. Asymmetric unit of gamma RDX, AAI molecule given in blue, AAA in green, illustrating the AAA molecule "cupping" the AAE molecule.

This can also be observed in Figure 3.12, which shows γ-RDX viewed down the *b*-axis. The packing arrangement of γ-RDX consists of alternating chains of AAI and AAA groups running parallel to the *a*-axis, adopting a similar zig-zag structure to that of α-RDX (Figure 3.13 and 3.14). However, inspection of Figures 3.13 and 3.14 reveals how the "cupping" of the AAA and AAI molecules in γ-RDX enables a more efficient zig-zagging arrangement.

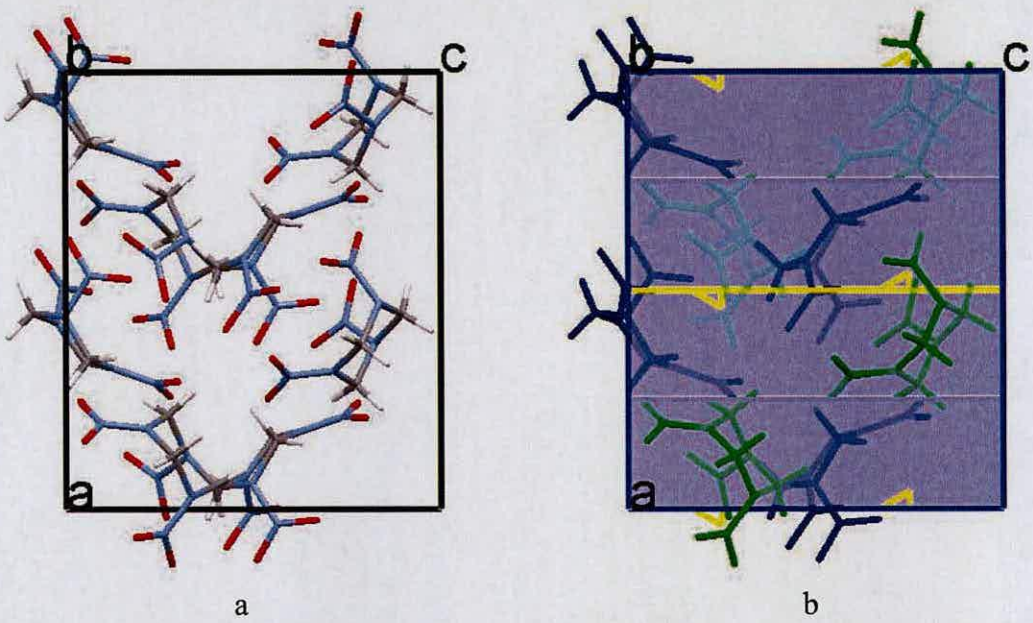

Figure 3.12. (a). Crystal structure of γ-RDX viewed down the *b*-axis, (b) crystal structure viewed down the *b*-axis, showing symmetry elements, with molecules coloured by symmetry equivalence (AAI shown in blue, AAA in green).

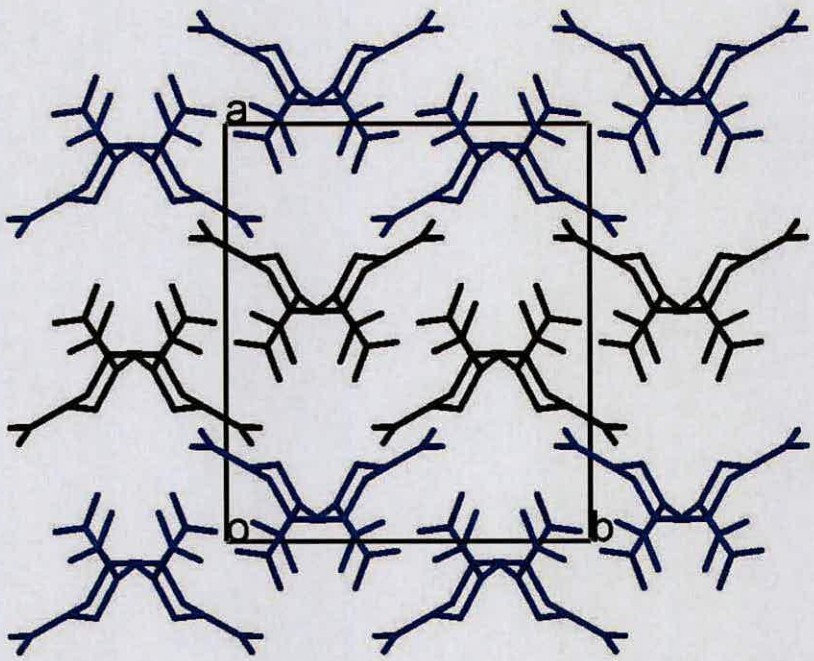

Figure 3.13. α-RDX viewed down the *c*-axis, AAI molecules shown in blue. Zig-zagging chain illustrated in black. Hydrogen atoms omitted for clarity

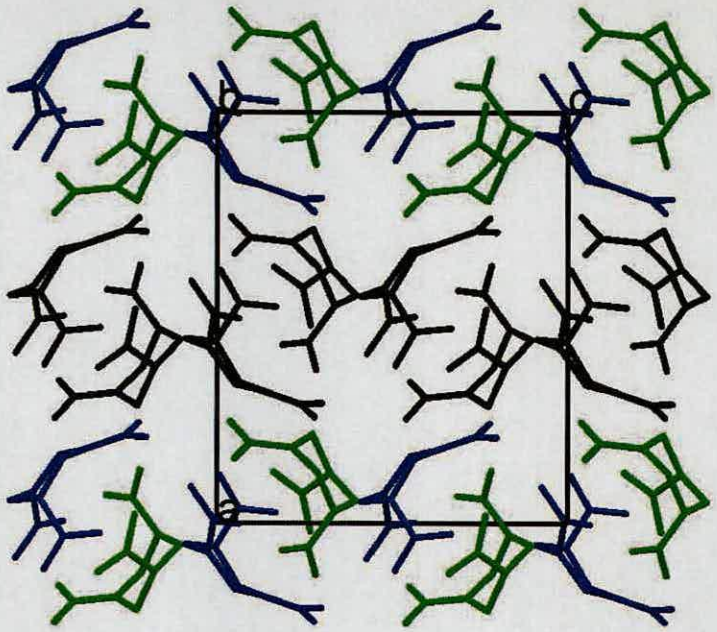

Figure 3.14. γ-RDX viewed down the *b*-axis, AAI molecules shown in blue, AAA molecules in green. Zig-zagging chain illustrated in black. Hydrogen atoms omitted for clarity

A consequence of the more efficient packing arrangement of γ-RDX is the change in the C-D...O-N, N...O, and N...N intermolecular contacts present in the structure (Table 3.8). It can be seen that the C-D...O-N distances change between the two phases. Between 3.85 GPa and 3.90 GPa, as α-RDX transforms into the γ-form, the C-D...O-N distances decrease (the average D...O distance in α-RDX at 3.85 GPa is 2.48(5) Å, where as at 3.90 GPa, the average D...O interaction is 2.42(4) Å). Further inspection of Table 3.8 show further reduction of all intermolecular interactions as the pressure is further increased up to 7.99 GPa.

	3.90 GPa	7.99 GPa
D22...O16	2.380(19)	1.960(17)
D61...O16	2.431(21)	2.349(8)
D31...O17	2.231(14)	2.208(31)
D42...O18	2.598(27)	2.351(12)
D21...O18	2.262(14)	2.255(11)
D51...O20	2.538(20)	2.515(33)
D52...O20	2.506(27)	2.150(14)
D51...O21	2.492(26)	2.476(19)
D41...O21	2.726(24)	2.660(14)
D61...O22	2.459(14)	2.336(19)
D11...O22	2.570(22)	2.543(15)
D52...O23	2.489(22)	2.372(23)
D41...O23	2.554(35)	2.442(11)
D61...O24	2.241(18)	2.148(8)
D51...O25	2.410(25)	2.291(14)
D52...O25	2.454(34)	2.440(23)
D31...O26	2.385(17)	2.184(35)
N11...N21	2.803(27)	2.701(31)
N12...N17	2.940(27)	2.864(32)
N10...O19	2.667(20)	2.578(28)
N13...O27	2.863(23)	2.686(28)
N16...O20	2.787(22)	2.613(26)
N17...O20	2.793(14)	2.762(14)
N19...O20	2.637(22)	2.457(28)
N20...O21	2.817(25)	2.626(29)
N21...O21	2.775(26)	2.595(29)

Table 3.8 Intermolecular interactions of γ-RDX at 3.90 and 7.99 GPa. All distances in Å.

The plots of the *a*-, *b*- and *c*-axis of RDX with increasing pressure for both α- and γ-RDX-d_6 (obtained from powder neutron data) are shown in Figure 3.15, with the corresponding plot of volume shown in Figure 3.16. As a result of the change of space group between α- and γ-RDX from *Pbca* to $Pca2_1$, a "reassigning" of axes has been performed for ease of comparison. Thus, the *b*-axis of α-RDX becomes the *c*-axis of γ-RDX, and *vice versa*.

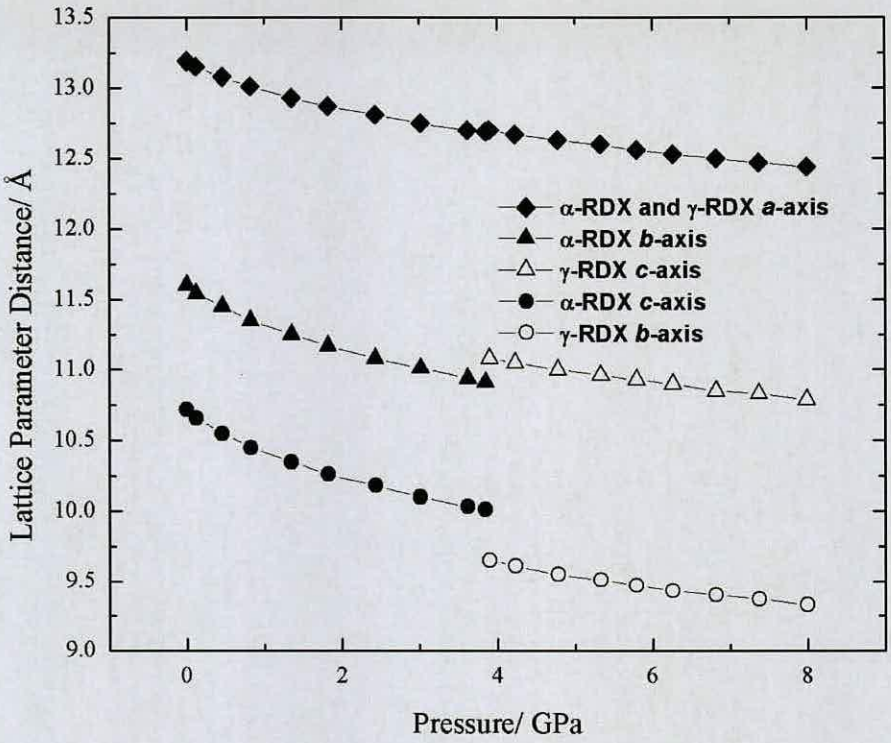

Figure 3.15. Plot of lattice parameters vs. pressure for RDX. The estimated standard deviations are smaller than the plotted symbols.

Figure 3.15 shows that there is no significant change in the *a*-axis with increasing pressure. However there is a slight increase of 1.6 % between the *b*-axis of α-RDX and the *c*-axis of γ-RDX over the transition. The most marked change in the lattice parameters is that of the *c*-axis of α-RDX which decreases by 3.6 % over the transition.

Figure 3.16 demonstrates that there is a 3 % decrease in volume between the two phases, confirming that this is a first order phase transition. This is a slightly larger change in volume than previously reported [6], but presumably reflects the higher precision of the lattice parameters obtained in the present study.

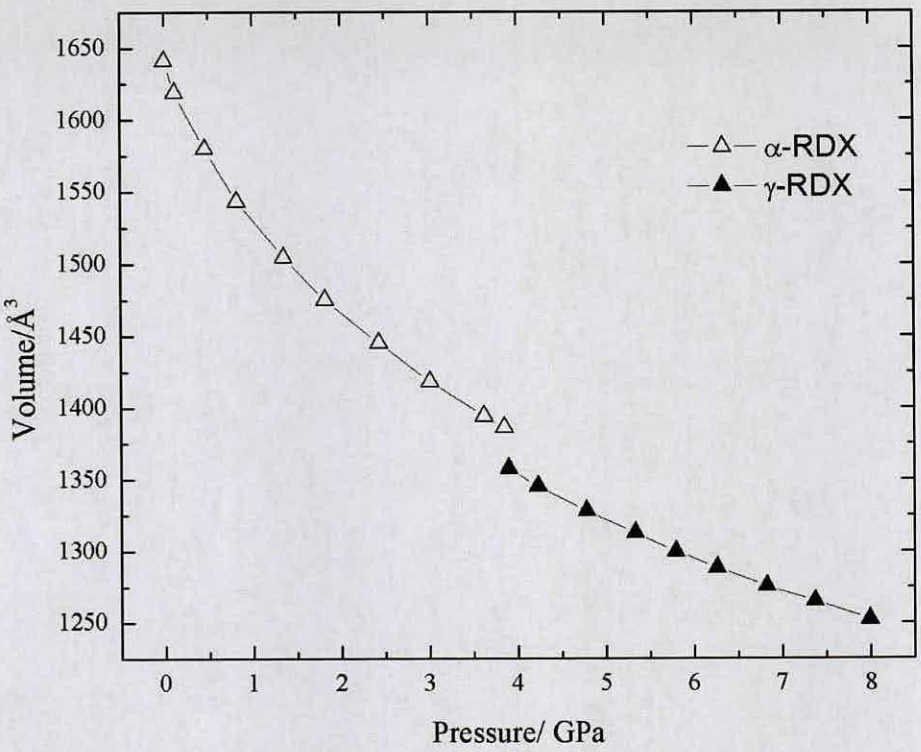

Figure 3.16. Volume plot for α- and γ-RDX. The estimated standard deviations on the volume are smaller than the plotted points. Line represents fit to equations of state for for α- and γ-forms.

As pressure is increased from 0.01 GPa to 3.85 GPa, there is an increase in density of α-RDX of 15.5% from 1.80 g/cm^3 to 2.13 g/cm^3. At the transition pressure there is a further increase in density of 3%. As pressure is further applied to γ-RDX, the density increases by 7.8 % between 3.90 GPa and 7.99 GPa

The volume data determined by powder neutron diffraction were used for the determination of the bulk modulus, B_0, and its pressure derivative, B_0', using a third-order Birch–Murnaghan equation of state (Equation 3.1) for both α- and γ- phases of RDX.

$$P = (3/2)\, B_0(x^{-7/3}-x^{-5/3})\, [1-(3/4)(4- B_0')(x^{-2/3}-1)] \qquad \text{Equation 3.1.}$$

Equation 3.1. x denotes the volume ratio V/V_o, V_o the volume at zero pressure, and B_o and B_0' the initial isothermal bulk modulus and its pressure derivative, respectively.

A least-squares fit to the measured data from 0.01 GPa to 3.85 GPa for α-RDX gave a value of B_o = 9.8(14) GPa for the bulk modulus of α-RDX, with B_0' = 11.4(30), and V_o = 1614.1 $Å^3$. These values are in fairly good agreement with previous studies (B_0 = 13.0 GPa and B_0' = 7.9, B_0 = 6.6 GPa and B_0' = 13.9) [40,41]. The small differences may be a result of the improved precision with which the unit cell volumes have been determined in this study - neither of the previous studies indicated the uncertainties in the derived parameters.

A least squares fit for the pressure range 3.90 GPa to 7.99 GPa of γ-RDX gives a value of B_o = 17.6(14) GPa for γ- RDX, with B_0' = 6.8(10), and V_o = 1557.6 $Å^3$. Thus, the high-pressure γ-phase is less compressible than α-RDX. The values differ from those reported [41] (B_0 = 10.9 GPa and B_0' = 7.9), but this again reflects the greater precision with which the lattice parameters have been determined in this work.

3.4 Conclusions: RDX

The results of this study agree with the majority of previous studies which have suggested that RDX undergoes a phase transition at *ca.* 4 GPa with a relatively small volume change. A point to discuss is the effect of deuteration on the transition pressure, since the transition pressure observed in the X-ray diffraction measurements is different than that of the powder neutron diffraction studies. However, the single-crystal X-ray diffraction data set reported was not the only data set obtained. Many other crystals of RDX were loaded into DAC. Although it was not possible to obtain structural information, it was possible to index the γ-form of

RDX in each case. The transition pressure for all these data sets was at *ca.* 4 GPa, indicating that the $\alpha \rightarrow \gamma$ transition in RDX is independent of deuterium substitution.

3.5 Results and Discussion: HMX

3.5.1 Structure of β-HMX

The crystal structure of β-HMX is shown in Figure 3.17. The structure comprises columns of HMX molecules sitting on the edges and centre of the unit cell, with the eight-membered rings adopting a "chair" conformation.

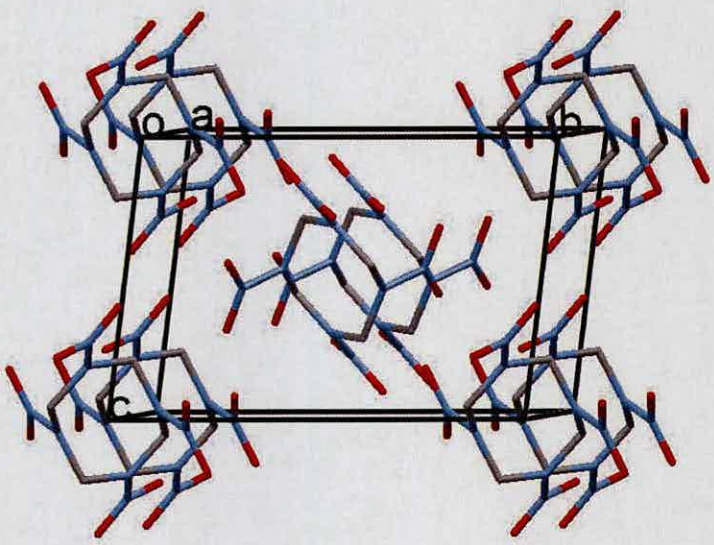

Figure 3.17. Crystal structure of β-HMX viewed down the *a*-axis

3.5.2 High-Pressure Powder Neutron Studies

Powder neutron diffraction patterns of deuterated β-HMX were recorded at increasing pressure steps between 0.01 GPa and 8.0 GPa, and the patterns are shown in Figure 3.18.

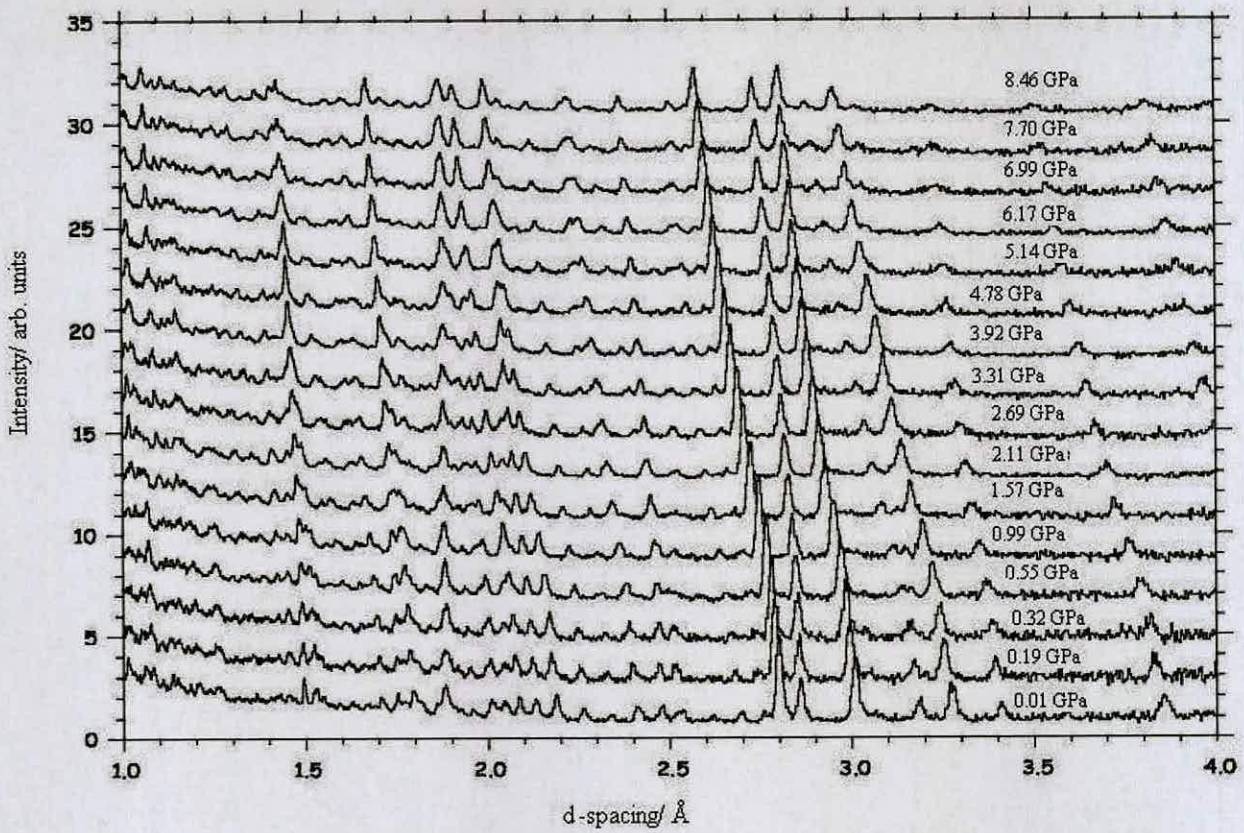

Figure 3.18. Neutron powder diffraction patterns of HMX as a function of pressure

Rietveld refinement of the neutron powder pattern at 0.01 GPa confirmed the presence of the β-HMX. Refinement was possible for all subsequent higher pressure data patterns. No phase transitions were observed up to pressures of 8.46 GPa. The pattern profiles obtained at 0.01 GPa, and 8.46 GPa are displayed in Figure 3.19 (χ^2 = 1.125, wRp= 0.0332, χ^2 = 1.223, wRp= 0.0364, respectively).

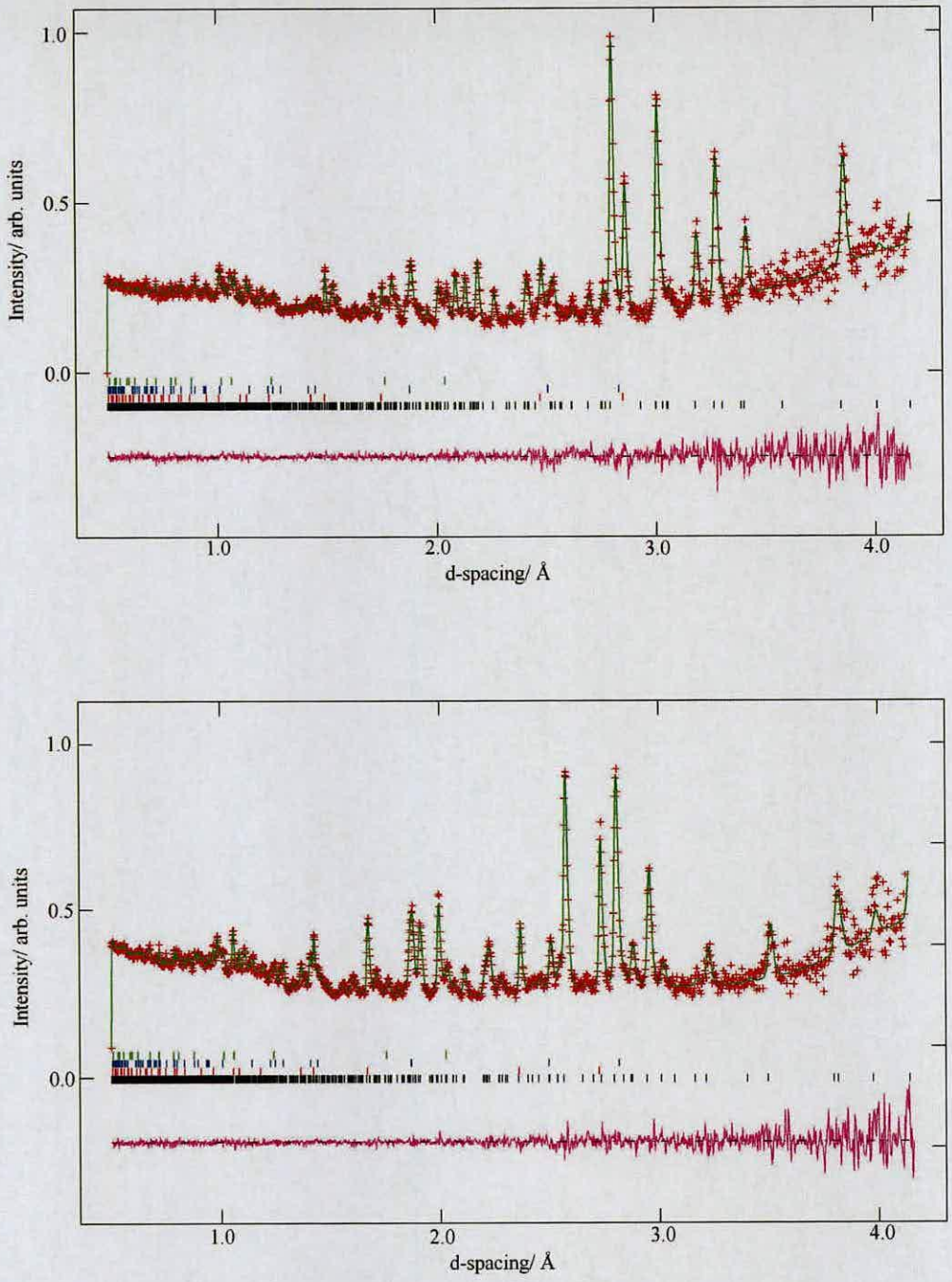

Figure 3.19. Powder neutron patterns of β-HMX at 0.01 and 8.46 GPa respectively. The crosses denote the observed intensities and the solid lines those calculated from the best-fit model of the respective Rietveld refinement. The tick marks represent the calculated peak positions, (black tick marks signify RDX, the red marks correspond to the lead internal pressure marker, and the blue and green tick marks represent tungsten carbide and nickel, respectively). The line below them represents the deviation between observed and calculated intensities.

The crystal structures between 0.01 GPa and 8.46 GPa show remarkably few differences. There is no significant change in any of the primary bonds or bond angles, and the eight-membered ring remains in the "chair" conformation. Figure 3.20 shows the structures at 0.01 GPa and 8.3 GPa. The most noticeable observation over this pressure range is the marked shortening of the C-D...O-N interactions (Table 3.9). A selection of intermolecular interactions present in β-HMX is illustrated in Figure 3.21.

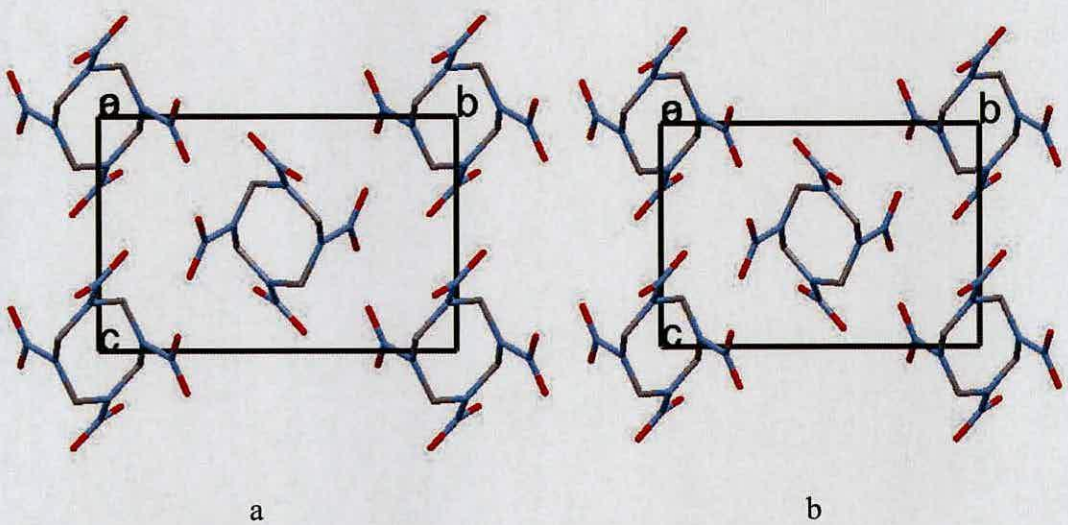

a b

Figure 3.20. (a). β-HMX at 0.01 GPa and (b). β-HMX at 8.46 GPa viewed down the *a*-axis.

	0.01 GPa	8.46 GPa
O1...D1	2.509(21)	2.131(16)
O1...D3	2.531(25)	2.039(16)
O2...D1	2.550(23)	2.211(17)
O2...D4	2.472(22)	2.121(18)
O3...D2	2.692(18)	2.457(12)
O3...D4	2.654(21)	2.319(16)
O4...D2	2.863(23)	2.617(14)
O4...D3	2.621(21)	2.255(17)

Table 3.9 Significant intermolecular interactions in β-HMX at 0.01 GPa and 8.46 GPa.

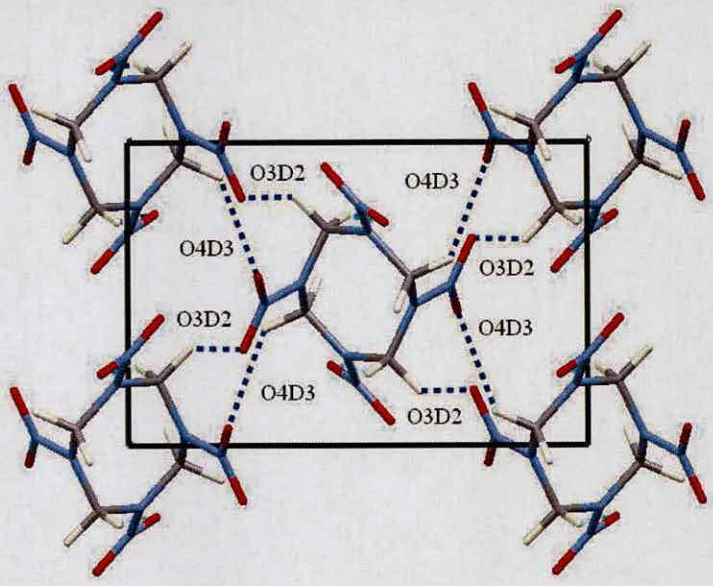

Figure 3.21 Selected intermolecular interactions in β-HMX

The variations in lattice parameters and unit-cell volume with increasing pressure are shown in Figures 3.22 and 3.23. Figure 3.22 shows that the *a*-, *b*- and *c*- axis decrease with increasing pressure, by 6.0%, 11.0% and 3.7%, respectively.

Figure 3.23 shows a smooth decrease in volume of 20.4% with decreasing pressure up to 8.4 GPa. The variation in volume was fitted to a third-order Birch–Murnaghan equation of state, to give a bulk modulus (B_o) of 12.316 (12) GPa. Both the ambient pressure volume V_0 and the pressure derivative of the bulk modulus B' were treated as a refinable parameters, to give values of 516.39(20) $Å^3$ and 11.36(11), respectively. This value of the bulk modulus is in good agreement with previous studies which reported a bulk modulus of 14.0 ±3.5 GPa [42].

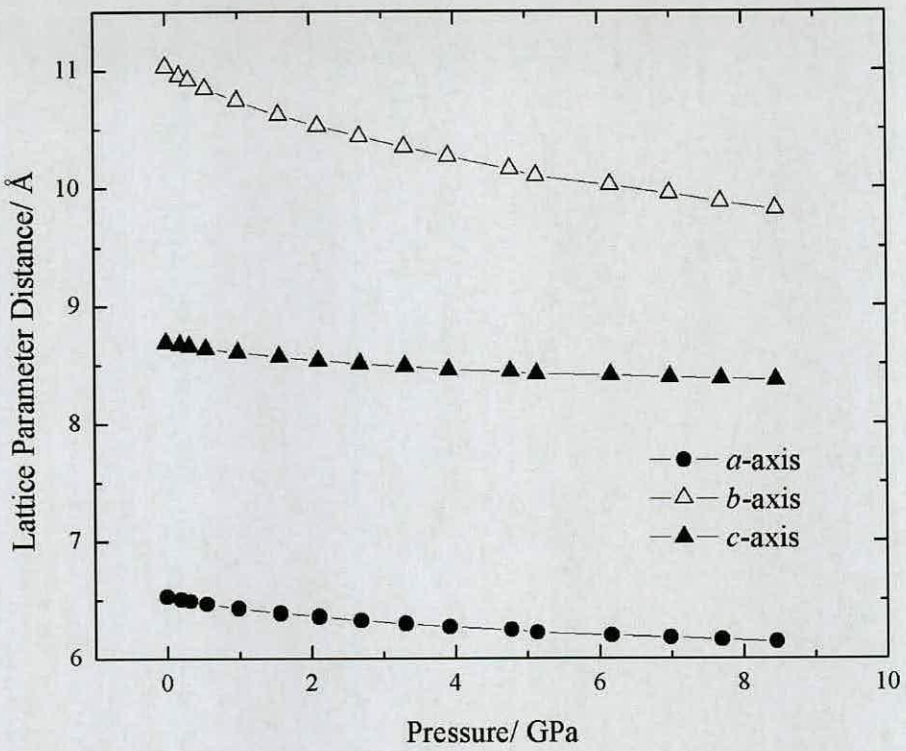

Figure 3.22. A plot of *a*-, *b*-, *c*- lattice parameters against pressure for β-HMX

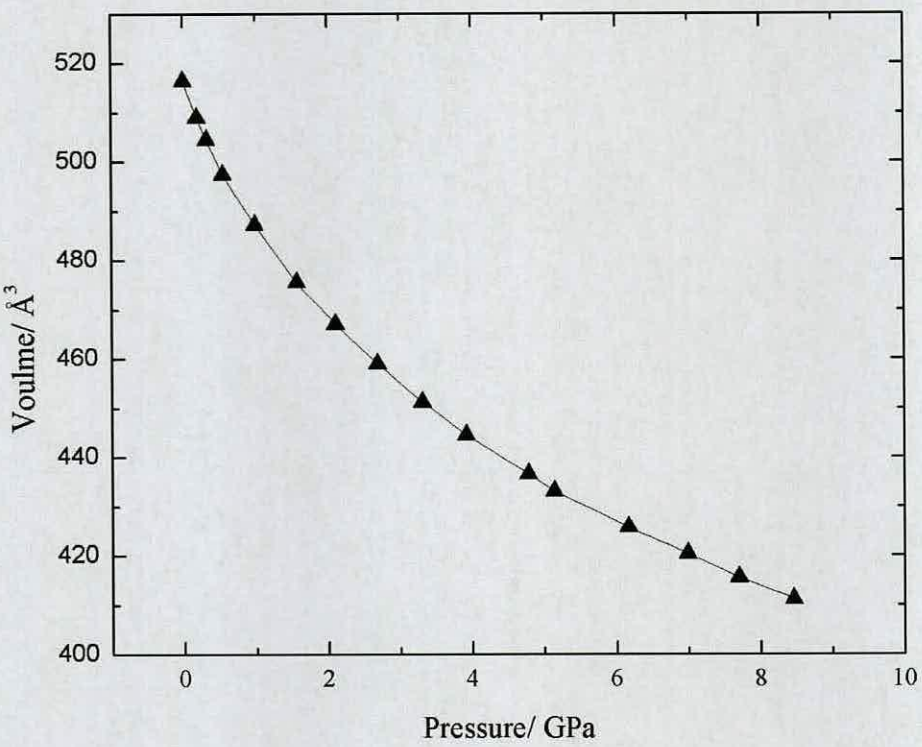

Figure 3.23. A plot of volume against pressure for β-HMX

3.5.3 High-Pressure Recrystallisation from Solution

A *ca* 1.0 M HMX-DMSO solution was loaded into a DAC. The cell was subsequently pressurised to 0.1 GPa with the precipitation of a polycrystalline material. As a result of careful temperature cycling, it was possible to dissolve all but one of the crystallites, and on slow cooling to 293 K a single crystal grew from solution to fill *ca*. 25 % of the gasket hole. Indexing of the reflections obtained from single crystal X-ray diffraction gave a new monoclinic unit cell, which was markedly different from that of any known polymorph of HMX. Structure solution using direct methods identified the crystal as *a new 1:2 HMX -DMSO solvate*.

3.5.4 Structure of HMX-DMSO Solvate (1:2)

The crystal structure of the HMX-DMSO solvate can be observed in Figure 3.24. The asymmetric unit comprises half a molecule of HMX and one molecule of DMSO. There is a small amount of positional disorder associated with the DMSO molecules; the sulfur atom and attached CH_3 groups are statistically distributed over two orientations. The solvate crystallises in the monoclinic crystal system, with space group of $P2_1/a$. The unit cell parameters are shown in Table 3.10. The HMX molecules in both the DMSO solvate and β-HMX have the same "chair like" configuration of the eight membered ring. There is no significant change in either the primary bond lengths or the bond angles in the HMX molecules between β-HMX and the 1:2 DMSO solvate.

A projection down the *b*-axis of the HMX-DMSO solvate shows alternating chains of DMSO and HMX molecules running parallel to both the *a* and *c*-axes (Figure 3.24).

	HMX-DMSO solvate at 0.1 GPa
Crystal System	monoclinic
Space group	$P2_1/a$
***a*/Å**	11.734(4)
***b*/Å**	7.109(4)
***c*/Å**	11.547(2)
α/°	90
β/°	90
γ/°	90
***V*/Å^3**	958.5(7)
Z	4
***D*$_c$/g cm^{-3}**	1.526
T/K	293(2)

Table 3.10 Lattice parameters of HMX-DMSO solvate

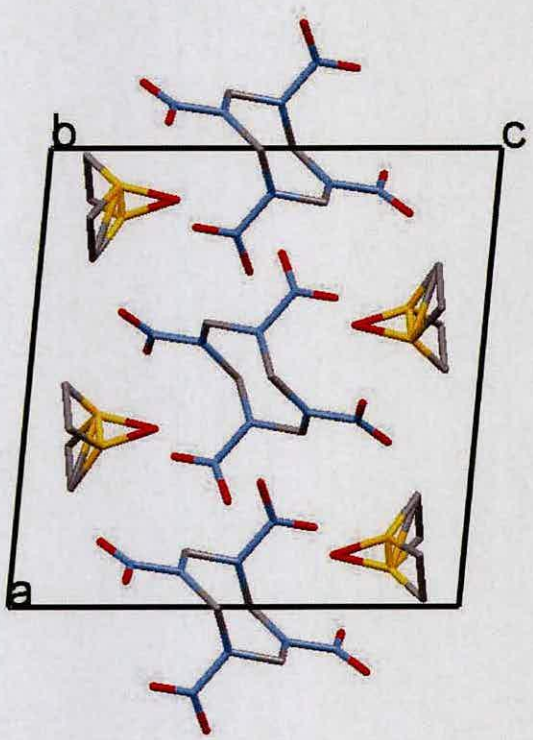

Figure 3.24 Crystal structure of DMSO HMX solvate viewed down the *b*-axis

Figure 3.25a illustrates the view down the *c*-axis, and shows that the HMX-DMSO solvate consists of chains of HMX and DMSO molecules running in the

direction of the (011) plane, related by the inversion centres in the centre of the HMX molecules, with HMX molecules sitting at the edges and centre of the unit cell. In the solvate the DMSO molecules effectively replace one chain of HMX molecules relative to β-HMX. This can be seen in Figure 3.26.

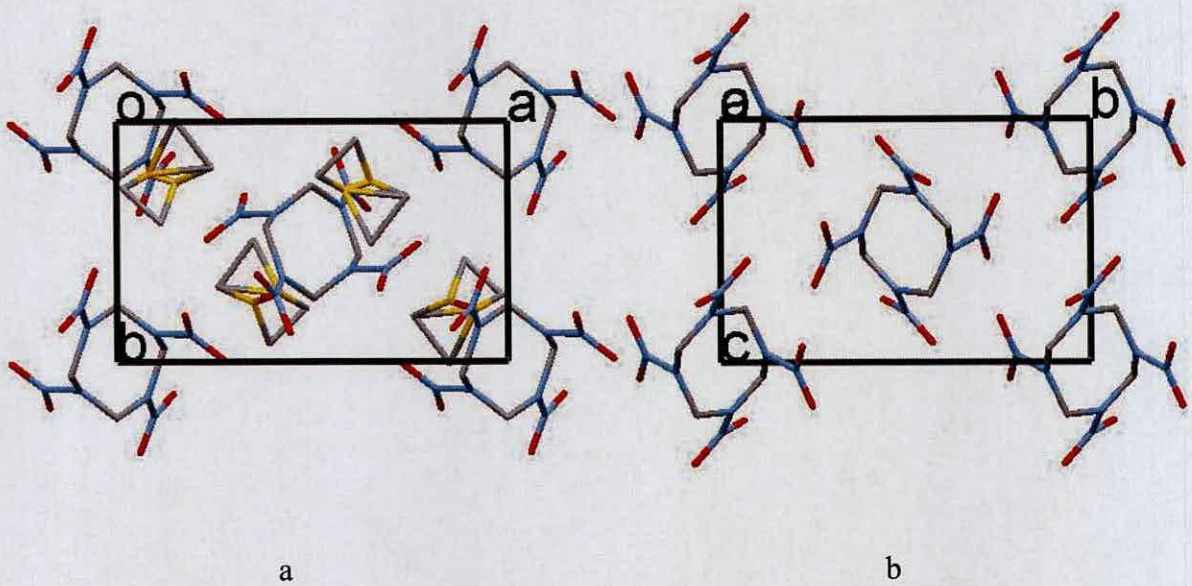

a b

Figure 3.25. (a). HMX-DMSO solvate viewed down the *c*-axis, (b. β-HMX viewed down the *a*-axis.

Since the pressure of formation of the HMX-DMSO solvate is relatively low, it seemed prudent to check whether this solvate could be grown under ambient conditions. Several attempts were made to grow crystals from various concentrations of HMX-DMSO solutions, with many crystals grown which were suitable for X-ray diffraction. However, all crystals proved to be β-HMX. This may however be due to the fact that desolvation occurred during the time taken for the crystal to be loaded onto a diffractometer. Further work could be undertaken

investigating this solvate under ambient conditions, perhaps by loading a crystal in a capillary.

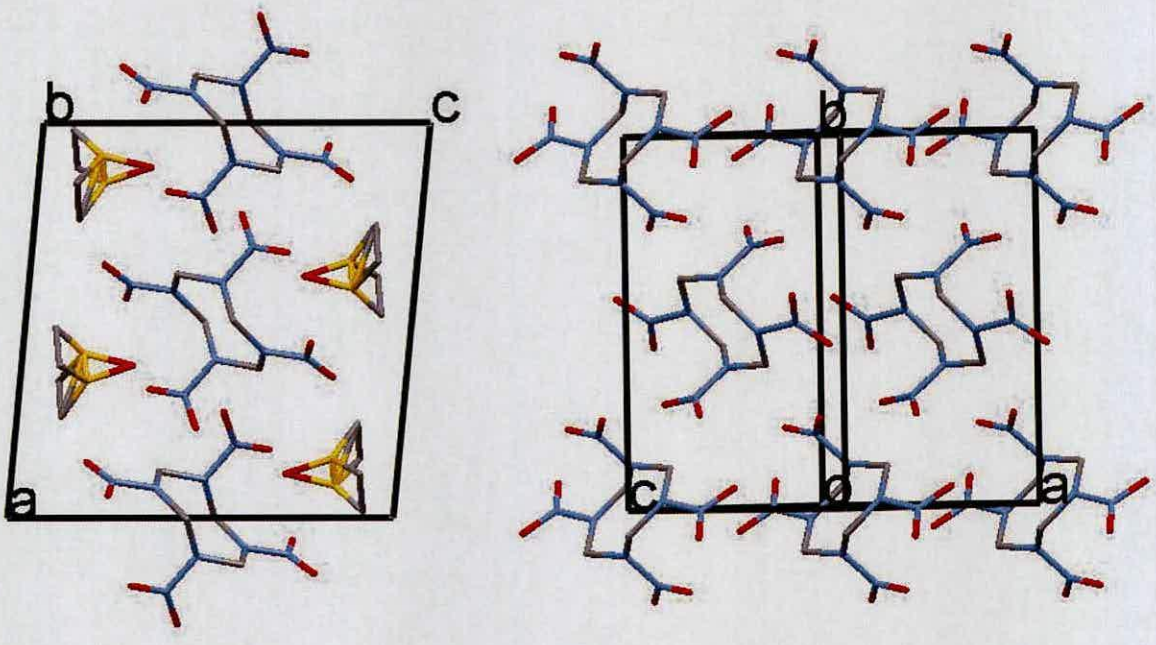

a b

Figure 3.26 (a). HMX-DMSO solvate viewed down the *b* –axis, (b). β-HMX viewed down the *b*-axis

3.6 Conclusions: HMX

Inspection of the intermolecular contacts present in the structure reveal that the possible driving force for the formation of this HMX-DMSO solvate is the short S-O…H-C interactions, which are in the region of 2.3-2.6 Å. This is in agreement with other HMX solvates, for example in both the HMX-DMF and HMX-NMP solvates, the C-H…O-C interactions are the strongest. The behaviour of HMX with solvents could be a very rich area for study both ambient and high-pressure recrystallisation. For example there are several reported solvates of HMX which have yet to be structurally characterised [14,16]. This work would hopefully add to

the understanding of the intermolecular interactions in HMX which may be important in its stability and decomposition.

3.7 General Remarks

It is evident from this study that the advances made in high pressure techniques provide information that has not previously been available. The high-pressure phase of γ-RDX has been structurally characterised for the first time. High-pressure recrystallisation from solvents has been shown to be an excellent technique for formation of a range of solvates, providing structural characterisation for the (1:2) HMX-DMSO solvate for the first time. Equation of state data has been obtained for α-RDX, γ-RDX and β-HMX using powder neutron diffraction. This study underlines the extent to which high pressure provides an additional dimension for the exploration of polymorphism and solvate formation. Hopefully this work will lead to further studies of energetic materials under pressure, and improve prediction and control of polymorphism in such materials.

3.8 References

[1] J. Akhavan, *The Chemistry of Explosives*, 2nd Edition; Royal Society of Chemistry. 2004.

[2] W.C. McCrone, *Anal. Chem.*,1950, **22**, 954.

[3]. C.S Choi, and E. Prince, *Acta Cryst.*, 1972, *B***28**, 2857.

[4] N. Goto, H. Yamawaki, K. Tonokura, K. Wakabayashi, M. Yoshida, and M. Koshi, *Mat. Sci. Forum.*, 2004, **465**, 189.

[5] D. C. Sorescu, B. M. Rice and D. L. Thompson, *J. Phys. Chem.*, 1999, **103**, 6783.

[6] S. J. P. Palmer, and J. E. Field, *Proc. R. Soc. London, Ser. A.*, 1982, **383**, 399

[7] Z. A. Dreger and Y. M. Gupta, *Phys. Chem. B.*, 2007, **111**, 3893.

[8] J. A. Ciezak, T. A. Jenkins, Z. Lui and R. Hemley, *J. Phys. Chem. A.*, 2007, **111**, 59.

[9] N. Goto, H. Fujihisa, H. Yamawaki, K. Wakabayashi, Y. Nakayama, M. Yoshida, M. Koshi, *J. Phys. Chem. B.*, 2006, *E*, 4

[10] H. H. Cady, A. C. Larson, D. T. Cromer, *Acta Cryst.*, 1963, **16**, 617.

[11] R. S. George, H. H. Cady, R. N. Rogers and R. K. Rohwer, *Ind. Eng. Chem. Prod. Res. Dev.*, 1965, **4**, 209.

[12] W. Selig, *Propellants Explos.*, 1982, **7**, 70.

[13] T. M. Haller, A. L. Rheingold and T. B. Brill, *Acta. Cryst.*, 1983, **C39**, 1559.

[14] D. M. Hoffman, R. W. Swansiger, *Propellants, Explosives, Pyrotechnics.*, 1999, **24**, 301.

[15] T. M. Haller, A. L. Rheingold and T. B. Brill, *Acta. Cryst.*, 1985, **C41**, 963.

[16] H. Czerski, M. W. Greenway, W. G. Proud, J. E. Field, *J. Applied. Phys.*, 2004, **24**, 409.

[17] B. F. Henson, B. W. Asay, R. K. Sander, S. F. Son, J. M. Robinson, P. M. Dickson, *Phys. Rev. Lett.*, 1999, **82**, 1213.

[18] F. Goetz, T. B. Brill, and J. R. Ferraro, *J. Phys. Chem.*, 1978, **82**, 1912.

[19] A. P. Esposito, D. L. Farber, J. E. Reuagh, J. M. Zaug, *Propellants, Explosives, Pyrotechnics.*, 2003, **28**, 82.

[20] C-S. Yoo and H. Cynn, *J. Phys. Chem.*, 1999, **111**, 10229.

[21] R. W. Shaw, T. B. Brill and D. L. Thompson, *Overviews of Recent Research on Energetic Material, Advanced Series in Physical Chemistry,* World Scientific, Singapore., 2005, **16.**

[22] S. Bulusu,, J. Autera, T. Axenrod, *Journal of Labelled Compounds and. Radiopharmaceuticals*., 1979, **17(5)**, 707.

[23] J. M. Besson, R. J. Nelmes, G. Hamel, J. S. Loveday, G. Weill, S. Hull, *Physica B*., **1992**, 180–181, 907.

[24] W. G. Marshall and D. Francis, *J. Appl. Crystallogr*., 2002, **35**, 122.

[25] D. L. Decker, *J. Appl. Phys*., 1971, **42**, 3239.

[26] A. C. Larson, R. B. Von Dreele, *Los Alamos National Laboratory Report* No. LA-UR-86-748. 1987.

[27] L. Merrill, W. A. Bassett, *Rev. Sci. Instrum*., 1974, **45**, 290.

[28] G. J. Piermarini, S. Block, J. D. Barnett, R. A. Forman, *J. Appl. Phys.,* 1975, **46**, 2774.

[29] S. A. Moggach, D. R. Allan, S. Parsons, L. Sawyer, J. E. Warren, *J. Synchrotron Rad.,* 2005, **12**, 598.

[30] A. Dawson, D. R. Allan, S. Parsons, M. Ruf, *J. Appl. Crystallogr*., 2004, **37**, 410.

[31] Bruker AXS, SAINT, Version 7.01A, Bruker-AXS, Madison, Wisconsin (USA), 2003.

[32] S. Parsons, SHADE. The University of Edinburgh (Scotland), 2004.

[33] G. M. Sheldrick, SADABS, version 2004/1, University of Göttingen (Germany), 2004.

[34] A. Altomare, A., G. Cascarano, C. Giacovazzo, A. Guagliardi, *J. Appl. Cryst.* 1993, *26*,343.

[35] P.W. Betteridge J. R. Carruthers, R. I. Cooper, C. K. Prout, D. J. Watkin, *J. Appl. Cryst.*, 2003, **36**, 1487.

[36] R. J. Hultgren, *Chem. Phys.*, 1936, **4**, 84.

[37] C.S. Choi, E. Prince, *Acta Crystallogr.*, 1972, *B***28**, 2857.

[38] V. Favre-Nicolin, R. Cerny, *J. Appl. Cryst.*, 2002, **35**, 734.

[39] T. Vladimiroff and B. M. Rice, *J. Phy. Chem. A.*, 2002, **106**, 10437.

[40] B. Olinger, B. Roof and H. Cady, *Symposium International Sur Le Comportement Des Milieux Denses Sous Hautes Pressions Dynamiques, Commissariat a l'Energie Atomique Centre d'Etudes de Vajours:* Paris, France, 1978, **3**.

[41] C-S. Yoo, H. Cynn, W. M. Howard and N. Holmes, *Proc. 11th Int. Detonation. Symposium USAS.*, 1998.

[42] R. Menikoff and T.D. Sewell, *High Press. Res.*, 2001, **21**, 121.

Chapter 4

Restricted Annex

Chapter 5

High-Pressure Studies of Ammonium Perchlorate and Ammonium Nitrate

Chapter Five: High-Pressure Studies of Ammonium Perchlorate and Ammonium Nitrate

5.1 Introduction

5.1.1 Ammonium Perchlorate

Ammonium perchlorate (AP), $[NH_4]^+[ClO_4]^-$, is a widely used energetic oxidiser in solid rocket motors and explosive compositions. When mixed with a polymeric binder and aluminium powder it forms a powerful, but smoky propellant that is used by launch vehicles such as the NASA Shuttle and the ESA Ariane-5.

Under ambient conditions of temperature and pressure, ammonium perchlorate adopts an orthorhombic crystal structure (*Pnma*), in which the NH_4^+ ions freely rotate [1,2,3]. Despite numerous reports of anomalies in a variety of physical properties of AP in the temperature range 10-298 K, a definitive study using neutron diffraction, inelastic neutron scattering, and Raman spectroscopy has shown that there is no evidence for any phase transition in this temperature range [4]. On heating to above 511-513 K, ammonium perchlorate undergoes an orthorhombic-to-cubic phase transition in which almost unrestricted rotational orientation of the perchlorate ions is observed [5].

With respect to the high-pressure behaviour of AP, several studies have been performed, but the results are rather ambiguous, and often tend to be contradictory. P.W. Bridgman was the first to study AP under extreme pressures and reported a change in volume at 3.1 GPa, when AP was subject to shear experiments at elevated temperatures [6]. A strong pressure dependence on the orthorhombic-to-cubic transition was observed when AP was compressed to 0.4 GPa [7]. Foltz *et al.*

studied AP using optical methods up to pressures of 26 GPa and reported no evidence for any high-pressure phases [8]. A combination of shock compression and X-ray powder diffraction measurements have been recorded at pressures up to 5.0 GPa. A change in the powder pattern was reported at 4.70 GPa, and the authors suggested that on the basis of its complexity that the pattern was characteristic of a monoclinic or triclinic unit cell [9].

Infrared studies of AP showed a change in the v_1 mode of the perchlorate group between 1.0 and 2.4 GPa [10]. This was assigned to the orthorhombic-to-cubic transition. Single-crystal shock-wave studies revealed no obvious phase transformations, but suggested that if any phase transition did occur that it would be accompanied with a negligible change in volume or with very slow kinetics [11, 12].

Investigation of the effects of pressure on AP up to 5.6 GPa were performed by Peiris *et al*, using energy dispersive X-ray powder diffraction and vibrational spectroscopy [13]. Discontinuities in the Raman spectra were observed at 0.9 GPa and 3.0 GPa, and these were attributed to phase transitions. New peaks were observed in the X-ray powder pattern above 0.9 GPa, which could not be indexed either to the known orthorhombic ambient phase or to any new phase. At 2.9 GPa further changes in the X-ray powder pattern were seen, but this pattern could not be indexed. An equation of state was obtained from the energy dispersive X-ray powder pattern, and a bulk modulus of 16.0(2) GPa was calculated.

In view of the remaining uncertainties about not only the high-pressure phase behaviour of ammonium perchlorate, but also the crystal structures of the proposed

high-pressure phases, it was decided to study this energetic material at high pressure using a combination of spectroscopic and diffraction techniques.

5.1.2 Ammonium Nitrate

Ammonium nitrate (AN), $[NH_4]^+[NO_3]^-$ is an energetic oxidiser, which forms an explosive mixture when combined with hydrocarbons such as diesel or kerosene. Ammonium nitrate is readily available as a fertiliser, and AN mixtures have been used by terrorist organisations for the construction of improvised bombs.

AN is an excellent example of a highly polymoprhic energetic material. At ambient pressure, five known temperature phases are known, and have been structurally characterised [14]. Form IV is stable under ambient conditions of temperature and pressure, but a known transition occurs at 305 K to a significantly less dense form III. Studies by Bridgman showed that under hydrostatic conditions AN does not undergo a phase transition at pressures up to 5.0 GPa [15]. However, under shear stress a shear-induced transition was observed at 2.94 GPa. Adams *et al.* have also observed this transition at 3.0 GPa using infrared spectroscopy under non-hydrostatic conditions in a non-gasketed diamond-anvil cell [16]. Shock-loading experiments up to *ca.* 20 GPa have suggested the presence of a shock-induced phase transition at a shock pressure of 3.5 GPa with a large associated volume change, indicating the presence of a previously unidentified high-pressure phase [17]. None of the previous studies was able to provide any structural information on any of the high-pressure phases.

It was therefore decided to explore the high-pressure behaviour of AN under both hydrostatic and non-hydrostatic conditions.

5.2 High-Pressure Powder Raman Studies: Ammonium Perchlorate

5.2.1 Experimental

High-pressure Raman studies were performed using a a Jobin-Yvon LabRam 300 instrument equipped with a 50 mW He-Ne laser of wavelength 632.8 nm. A Merrill-Bassett DAC equipped with 600 μm culet diamonds and a tungsten gasket was used to produce high pressures. A powdered sample of AP (Sigma-Aldrich, 99.999%, checked by powder X-ray diffraction) was loaded into the DAC, together with a 4:1 mixture of methanol:ethanol and a ruby chip. The pressure applied to the sample was determined by the ruby fluorescence method [18] using the 632.8 nm line from a He-Ne laser. The fluorescence was detected using the Jobin-Yvon LabRam 300.

5.2.2 Results

Scans with acquisition times of 30 mins were collected at incremental pressure steps between 0.4 GPa and 5.1 GPa. Figure 5.1 shows the Raman spectra plotted at selected pressures. From ambient pressure to 3.6 GPa, no significant changes were observed in the spectra. At 4.0 GPa, a shoulder was observed on the energy band at *ca.* 460 cm^{-1} associated with the bending of the ClO_4^- unit. Since this vibrational mode corresponds to the degenerate Cl-O bending motion (symmetry T_2), it suggests that the local symmetry of the ClO_4^- ion has been altered, thus reducing

the degeneracy of the T_2 mode. Such a change is consistent with a phase transition. These observations prompted a study by powder neutron diffraction.

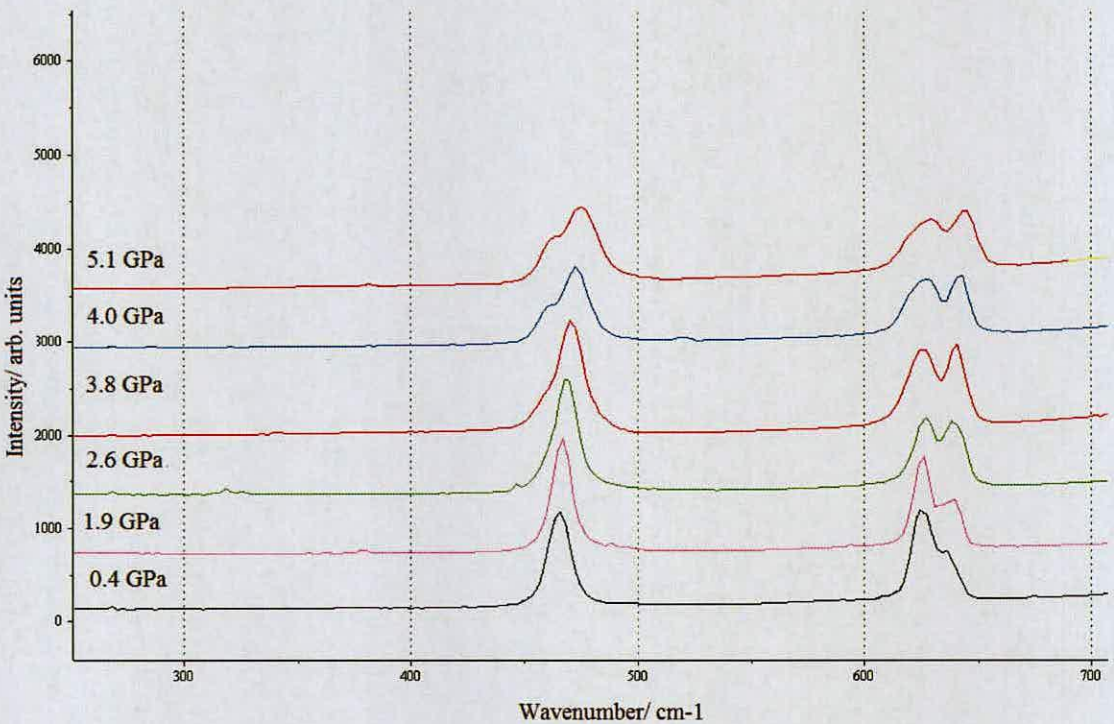

Figure 5.1 Raman spectra of ammonium perchlorate with increasing pressure

5.3 High-Pressure Powder Neutron Studies: Ammonium Perchlorate

5.3.1 Experimental

Deuteration of AP was achieved by repeated recrystallisation from deuterium oxide. 5.0 g of sample was dissolved in 15 cm^3 of D_2O, followed by evaporation of the solvent under vacuum until precipitation occurred. This was repeated twice. A lightly ground sample of AP was loaded with NaCl as a pressure calibrant (*ca.* 30% by volume) and then loaded into an encapsulated TiZr gasket [19] together with a

small quantity of a 4:1 methanol:ethanol mixture. The gasket was then loaded into a Paris-Edinburgh cell [20] at the ISIS Neutron Facility, Rutherford Appleton Laboratory, UK. Time-of-flight neutron powder diffraction patterns were then recorded using the $2\theta = 90°$ detectors of the PEARL diffractometer with a 'transverse' (through-anvil) scattering geometry. Full Rietveld analysis was performed for each data set using GSAS [21].

5.3.2 Results

High-pressure powder neutron patterns were collected at increasing pressure steps between 0.01 GPa and 8.13 GPa (Figure 5.2). Indexing of the pattern recorded at 0.01 GPa was possible and confirmed the presence of the known ambient phase I.

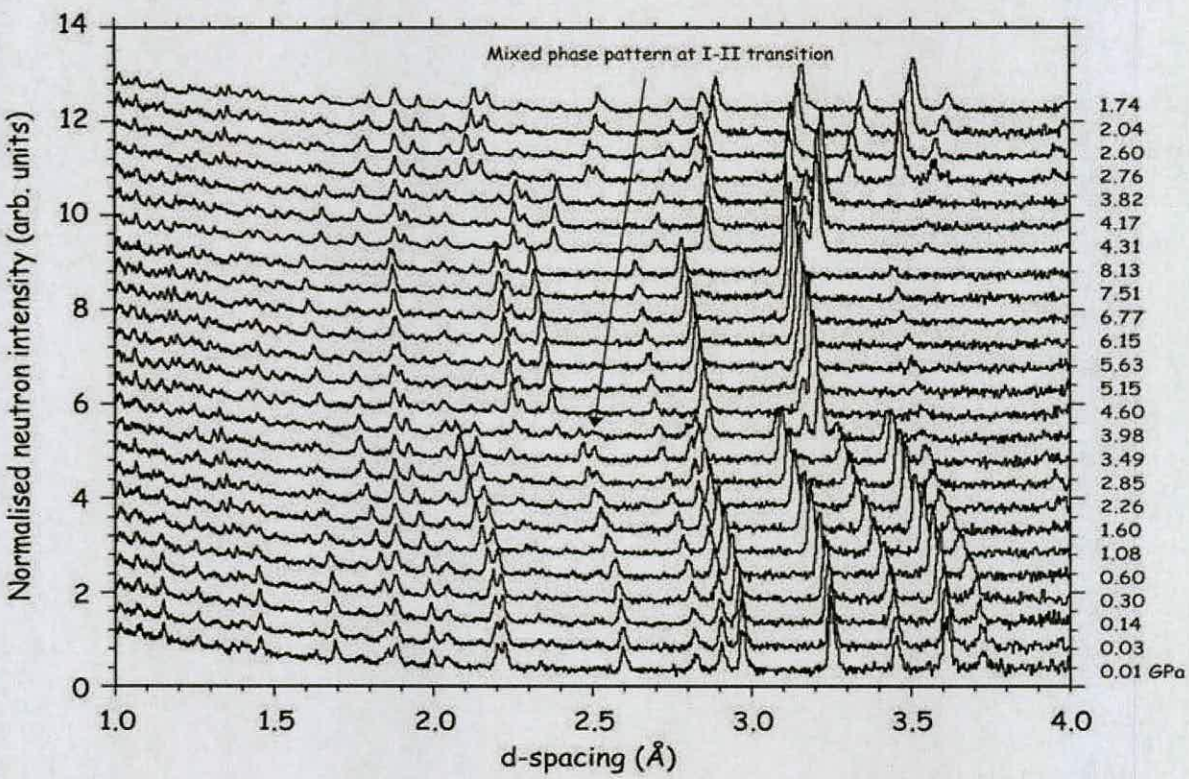

Figure 5.2. Neutron powder patterns of ammonium perchlorate as a function of increasing pressure collected at 298 K.

Figure 5.3 shows the best fit of the model obtained by Rietveld refinement at 0.01 GPa (wRp = 0.033). This phase persisted up to 3.49 GPa. On increasing the pressure to 3.98 GPa new peaks were observed to grow in the diffraction pattern in addition to those associated to phase I. On increasing the pressure to 4.60 GPa, the Bragg peaks associated with phase I disappeared completely. This new powder pattern could be indexed to an orthorhombic unit cell, with a = 9.2185(14) Å, b = 5.8108(9) Å, c = 7.4504(13) Å. On the basis of systematic absences in the diffraction pattern, the space group of the high-pressure phase was tentatively assigned as *Pnma* although $P2_12_12_1$ was an alternative possibility. Single-crystal X-ray diffraction studies were therefore performed in order to resolve this potential ambiguity, and also to discover whether a single-crystal would survive the transition intact.

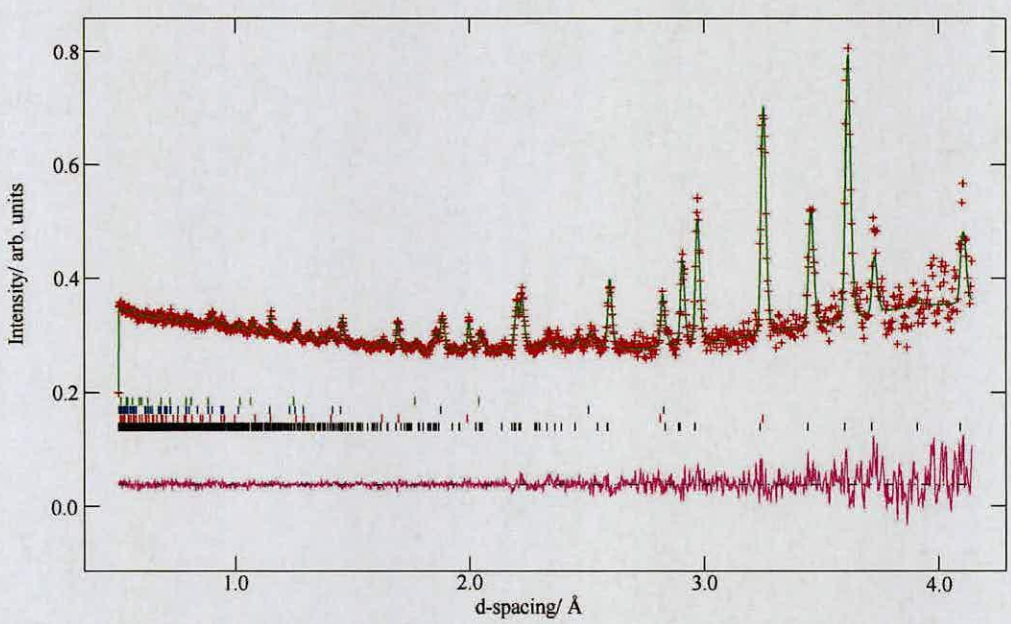

Figure 5.3 Neutron powder diffraction pattern of AP at 0.01 GPa. The crosses denote the observed intensities and the solid lines those calculated from the best-fit model of the Rietveld refinement. The tick marks represent the calculated peak positions, (black tick marks signify AP, the red marks correspond to the NaCl internal pressure marker, and the blue and green tick marks represent tungsten carbide and nickel, respectively). The line below them represents the deviation between observed and calculated intensities.

5.4 High-Pressure Single-Crystal X-Ray Studies: Ammonium Perchlorate

5.4.1 Experimental

A Merrill-Basset DAC was used to provide high pressures for single-crystal X-ray diffraction [22] equipped with 600 μm culet diamonds and a tungsten gasket. A single-crystal and small ruby chip were loaded into the DAC. A mixture of 4:1 methanol:ethanol was used as a pressure-transmitting medium. The pressure applied to the sample was determined by the ruby fluorescence method [18] using a 441.4 nm excitation line from a Hg-Cd laser. The fluorescence was detected by a Jobin-Yvon LabRam 300.

Studies were performed at the STFC Daresbury Laboratory Synchrotron Radiation source on station 9.8 (λ = 0.6765 Å) using a Bruker APEX II diffractometer at 293(2) K. High-pressure data sets were collected in ω-scans in 10 settings of 2θ and φ with a frame and step size of 1s and 0.2˚respectively [23]. Data collection used the procedures outlined by Dawson *et al* [24]. Integration of intensities was performed using SAINT (Bruker Nonius) [25] implementing the dynamic masking procedures. Further data treatment for absorption corrections was performed using SHADE [26] and SADABS [27]. Structures were solved by direct methods using SIR92 [28] and full-matrix least-squares structure refinement against $|F|^2$ was performed using *CRYSTALS* [29]. Hydrogen atoms were geometrically placed and allowed to ride as their parent atom. MERCURY [30] was used to visualise all structures.

5.4.2 Results

The DAC was initially pressurised to *ca.* 0.5 GPa. Indexing confirmed the known orthorhombic phase. The pressure was then increased to *ca.* 4.2 GPa. Indexing confirmed the new orthorhombic unit cell observed in the powder neutron diffraction compression studies and confirmed the space group to be *Pnma*. Structure solution using direct methods with subsequent full-matrix least-squares structure refinement was possible at both pressures.

Structure solution of the high-pressure powder neutron diffraction data was then achieved. The Rietveld plot at 4.60 GPa is illustrated in Figure 5.4 (wRp = 0.050). All atoms were refined with isotropic displacement parameters. All distances were restrained to the values observed in the ambient structure of AP. Tetrahedral bond angle restraints for both the ammonium and perchlorate groups were used.

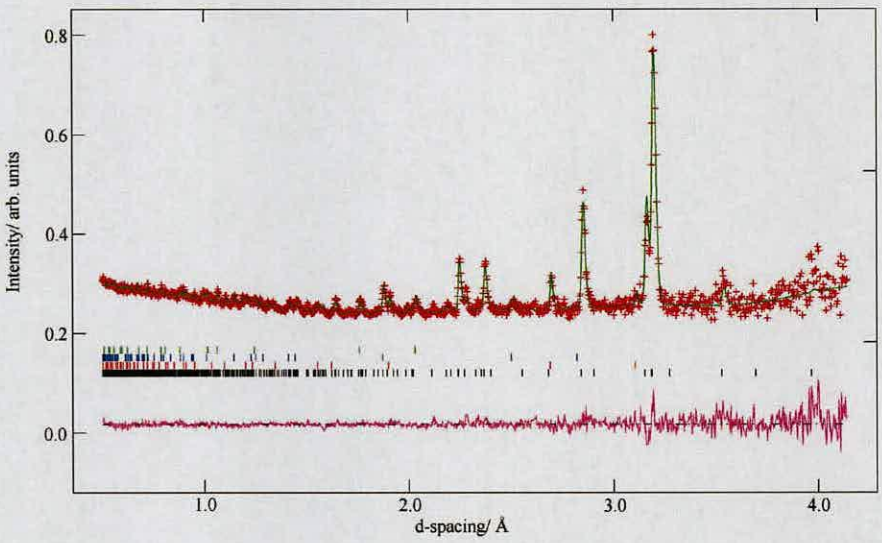

Figure 5.4 Neutron powder diffraction pattern of AP at 4.60 GPa. The crosses denote the observed intensities and the solid lines those calculated from the best-fit model of the Rietveld refinement. The tick marks represent the calculated peak positions, (black tick marks signify AP, the red marks correspond to the NaCl internal pressure marker, and the blue and green tick marks represent tungsten carbide and nickel, respectively). The line below represents the deviation between observed and calculated intensities.

5.5 Discussion: Ammonium Perchlorate

5.5.1 Phase I

The structure of ammonium perchlorate at ambient pressure has been previously determined to be orthorhombic *Pnma*, with one ammonium ion, and one perchlorate ion in the asymmetric unit (Figure 5.5). Unit cell parameters obtained from powder neutron diffraction studies at 0.01 GPa are given in Table 5.1. Unit cell parameters of phase I with increasing pressure are given in Table 5.3, page 169.

Crystal System	orthorhombic
Space group	*Pnma*
***a*/Å**	9.2185(14)
***b*/Å**	5.8108(9)
***c*/Å**	7.4504(13)
***α*/°**	90
***β*/°**	90
***γ*/°**	90
***V*/Å^3**	399.07(7)
Z	4
D_c/g cm^{-3}	2.0221
T/K	293(2)

Table 5.1 Unit cell parameters for phase I

Figure 5.6 shows the crystal structure of phase I. The structure comprises chains of alternating ammonium and perchlorate ions running parallel to the *a*-axis. Under ambient conditions, each perchlorate ion is surrounded by 7 ammonium ions, and each ammonium ion is surrounded by 7 perchlorate ions, with the N...O distances of these seven neighbours lying within 3.20 Å. O1 and O3 atoms each

form three hydrogen bonds (< 2.70 Å) to neighbouring ions, whilst O2 forms only one hydrogen bond at a distance of 1.98 (2) Å.

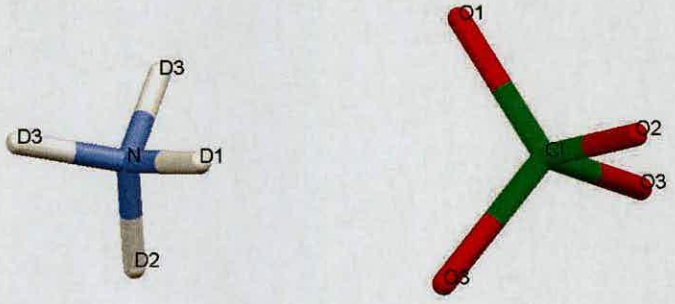

Figure 5.5. Labelled asymmetric unit of phase I of ammonium perchlorate

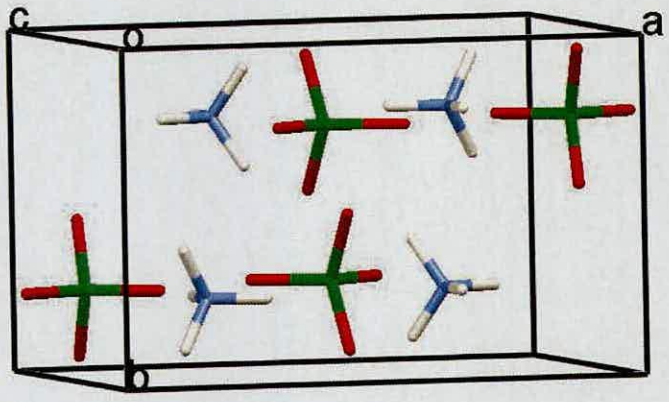

Figure 5.6. Crystal structure of ammonium perchlorate under ambient conditions viewed down the *c*-axis.

Structural refinement of all neutron powder diffraction patterns between 0.01 GPa and 3.49 GPa reveal that there were no significant changes in the structure of

phase I with increasing pressure. However the cations and anions move closer together thereby reducing the sizes of voids in the structure (Figure 5.7).

Previous studies had shown that at ambient pressure and temperature the ammonium ions are freely rotating. Inspection of the deuterium isotropic displacement parameters (u_{iso}) with increasing pressure reveal that they become progressively smaller. It is clear that the essentially free rotation observed under ambient conditions becomes more restricted with increasing pressure, thus mirroring the effects of cooling. However, even at 3.49 GPa the deuterium atoms of the ammonium ions are still undergoing substantial motion about their equilibrium positions. No significant changes in the hydrogen bonding interactions were observed in the pressure range 0.01-3.49 GPa.

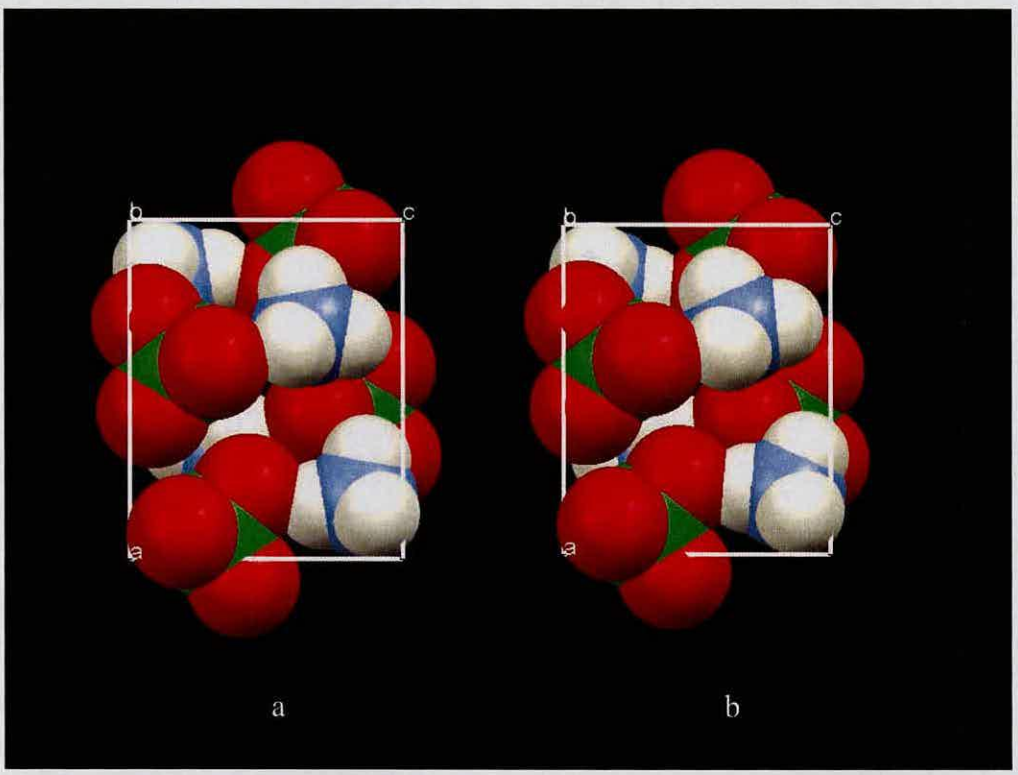

Figure 5.7. Space fill plots of phase I of ammonium perchlorate at (a) 0.01 GPa and (b) 3.49 GPa showing closing of central void with increasing pressure

5.5.2 Phase II

The high-pressure structure of AP, designated phase II, is orthorhombic, with a space group of *Pnma*. The asymmetric unit comprises one ammonium ion and one perchlorate ion. Unit cell parameters from powder neutron diffraction data are shown in Table 5.2. Unit cell parameters of phase II with increasing pressure are given in Table 5.3, page 169.

Crystal System	orthorhombic
Space group	*Pnma*
***a*/Å**	7.4577(4)
***b*/Å**	6.3347(12)
***c*/Å**	7.1182(17)
***α*/°**	90
***β*/°**	90
***γ*/°**	90
***V*/Å^3**	336.28(8)
Z	4
***D*$_c$/g cm^{-3}**	2.400
T/K	293(2)

Table 5.2 Unit cell parameters for phase II at 3.98 GPa

The crystal structure comprises chains of alternating ammonium and perchlorate ions as in phase I (Figure 5.8). In phase II the centroid represented by the central ammonium ion has twelve nearest neighbouring centroids (eight $[ClO_4]^-$ ions and four $[ND_4]^+$ ions) that lie within 4.3 Å and these are arranged in a manner that approximates to hexagonal close packing (Figure 5.9). This more efficient packing arrangement is shown in Figures 5.10 and 5.11.

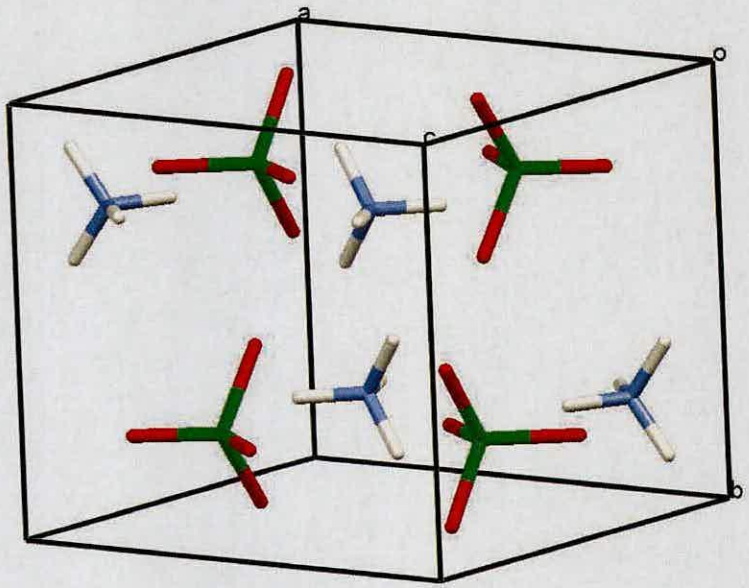

Figure 5.8 Crystal structure of phase II of AP.

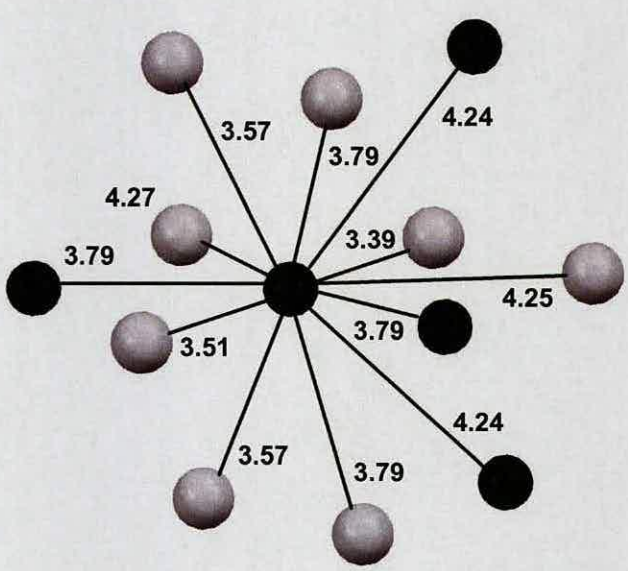

Figure 5.9. Environment of an ammonium ion in phase II of AP showing centroids formed by ND_4^+ (black centorids) and ClO_4^- ions (white centroids -distances in Å).

Viewed down the *b*-axis, both phases display chains of molecules running parallel to the *a*-axis (Figure 5.10). This can be also seen in Figure 5.11, which shows a projection down the *c*-axis.

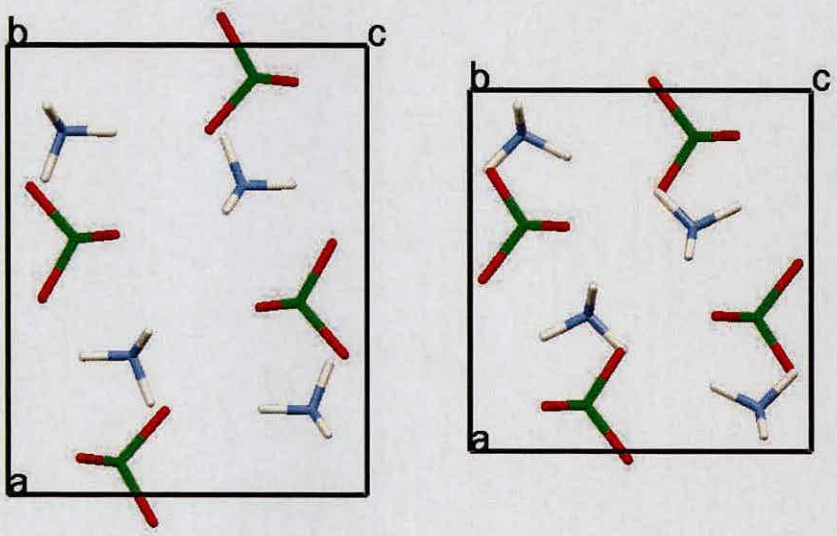

Figure 5.10. Crystal structure of (a) phase I (b) phase II of AP viewed down the *b*-axis

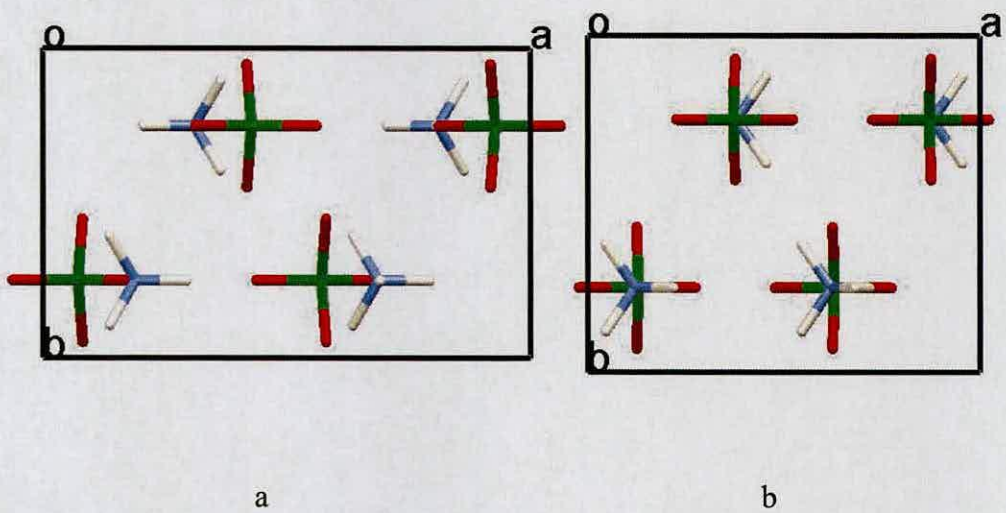

Figure 5.11. Crystal structure of (a) phase I (b) phase II of AP viewed down the *c*-axis

Viewed down the *c*-axis, both phases comprise chains of molecules running parallel to the *a*-axis. In phase I the ammonium ions and perchlorate ions are offset from one another, whereas in phase II the ions form a column of alternating ND_4^+ and ClO_4^- groups along the direction of the *c*-axis.

Figure 5.12 shows the space fill plots for phases I and II. A consequence of the transition is that there is a marked reduction in the central void. This correlates well with the observation of a significant increase in density is observed over the transition.

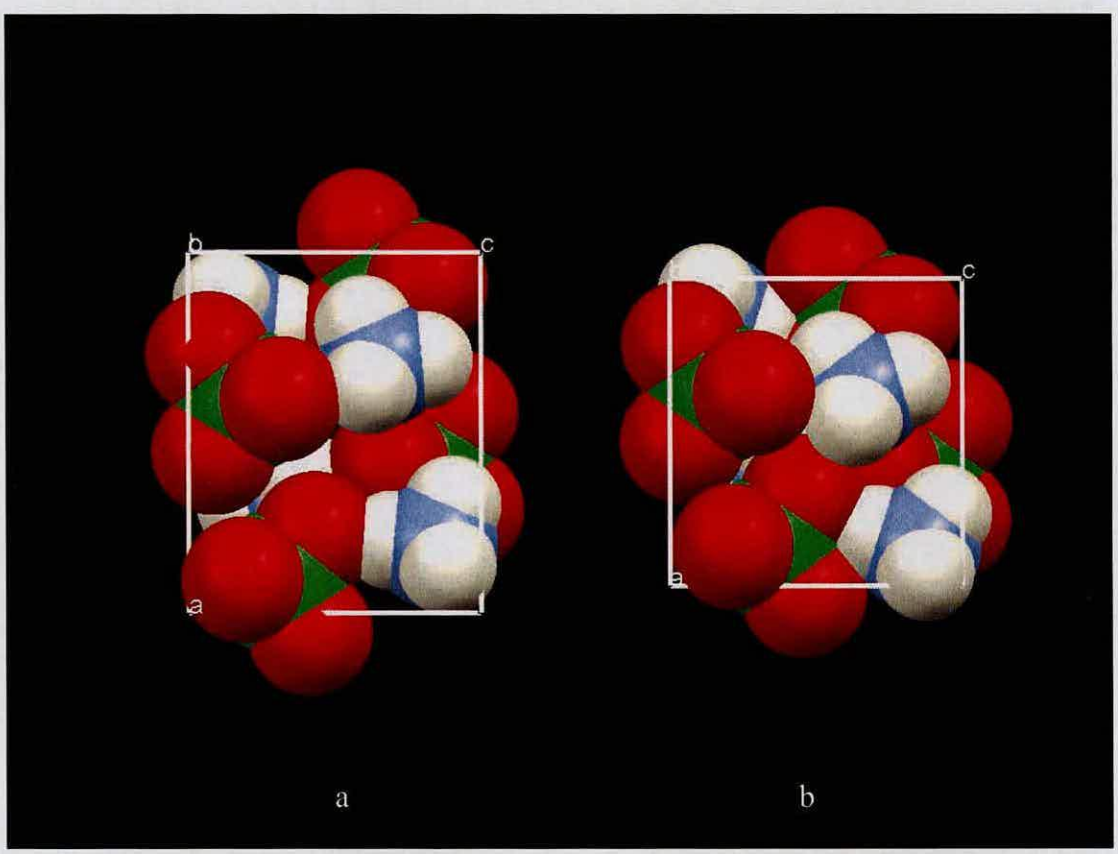

Figure 5.12. Space fill plot of (a) phase I of AP at 3.49 GPa (b) phase II of AP at 3.98 GPa, viewed down the *b*-axis.

With increasing pressure there are no significant changes to the structure apart from the cations and anions moving closer together. Inspection of the isotropic displacement parameters (u_{iso}) of phase II associated with the deuterium atoms reveal that they become progressively smaller with increasing pressure. Over the pressure range 0.01 → 8.0 GPa, no significant changes are observed in the hydrogen bonding interactions apart from D3…O3, which decreases over the transition from 2.21(20) Å to 1.81(18) Å (Figure 5.13). The change in D3…O3 in the crystal structure with increasing pressure is shown in Figure 5.14. All bond length errors represent ±σ.

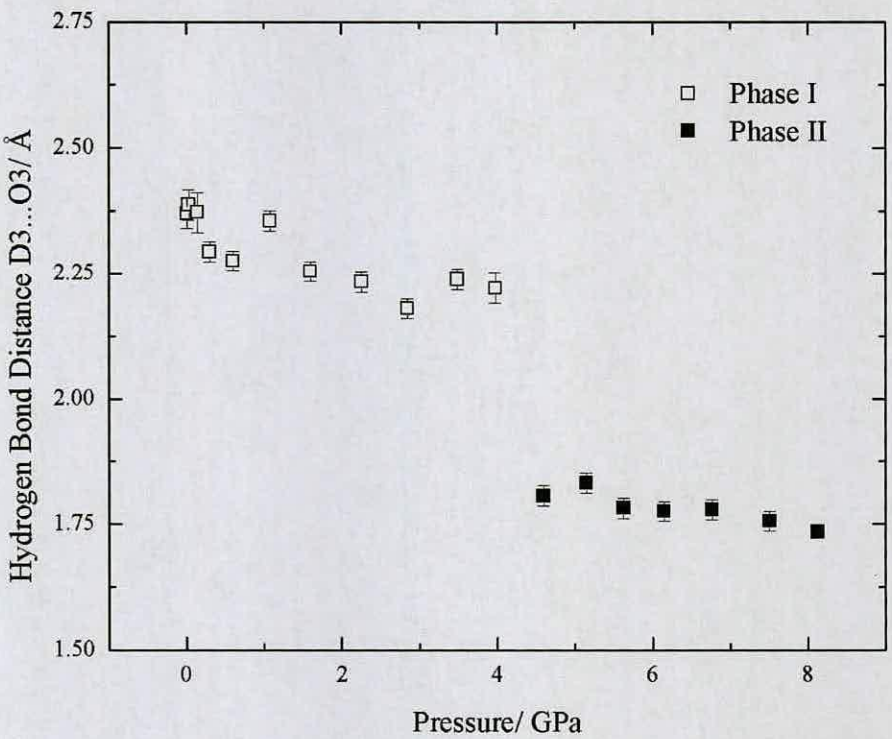

Figure 5.13. Variation in hydrogen bonding interaction D3…O3 with increasing pressure.

Figure 5.15 shows the variation of lattice parameters over the pressure range 0.01 to 8.13 GPa, and they are listed in Table 5.3. Over the transition there is as 13.8% decrease in the *a*-axis, and a 11.6% increase in the *b*-axis, and the *c*-axis changes only very slightly. The D3...O3 interaction has a significant component along the *a*-axis and the shortening of this bond at the transition manifests itself in the decrease in the *a*-lattice parameter.

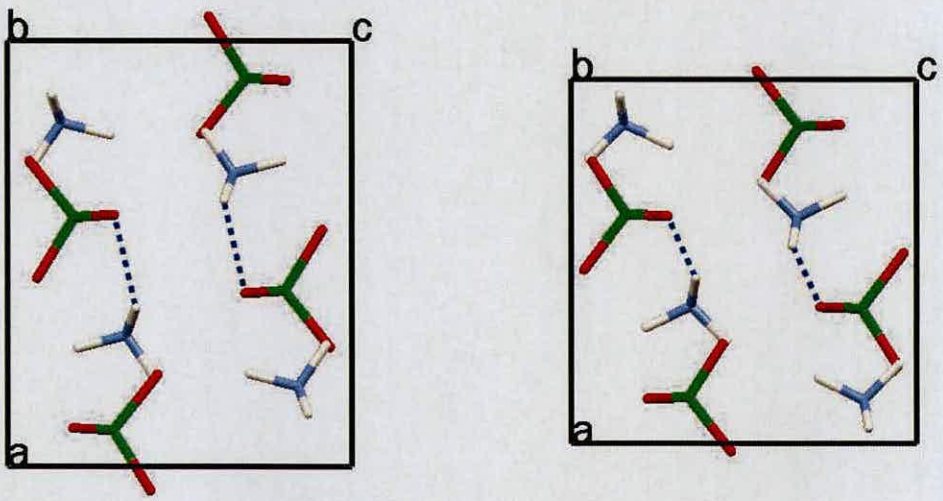

a b

Figure 5.14. (a) phase I of AP at 3.49 GPa, (b) phase II of AP at 3.98 GPa, viewed down the *b*-axis, showing the variation in hydrogen bonding distance D3...O3 (shown in blue).

Figure 5.16 illustrates the change of volume of both phase I and phase II. Over the transition, there is a 3.3% decrease in volume, thus confirming speculation from earlier studies that any phase transition would have only a small change in volume associated with it [12].

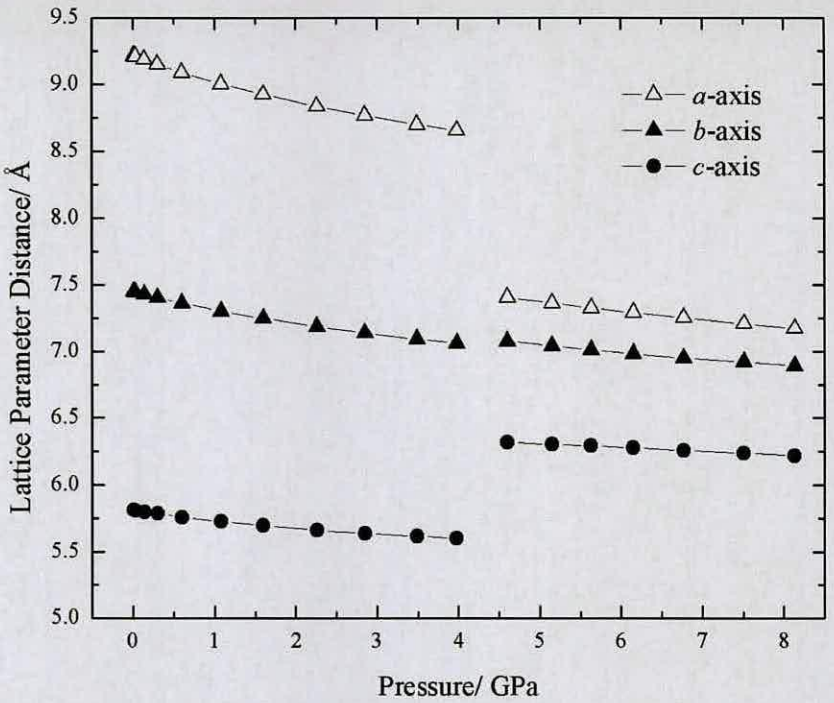

Figure 5.15. Variation of lattice parameters of ND_4ClO_4 with increasing pressure.

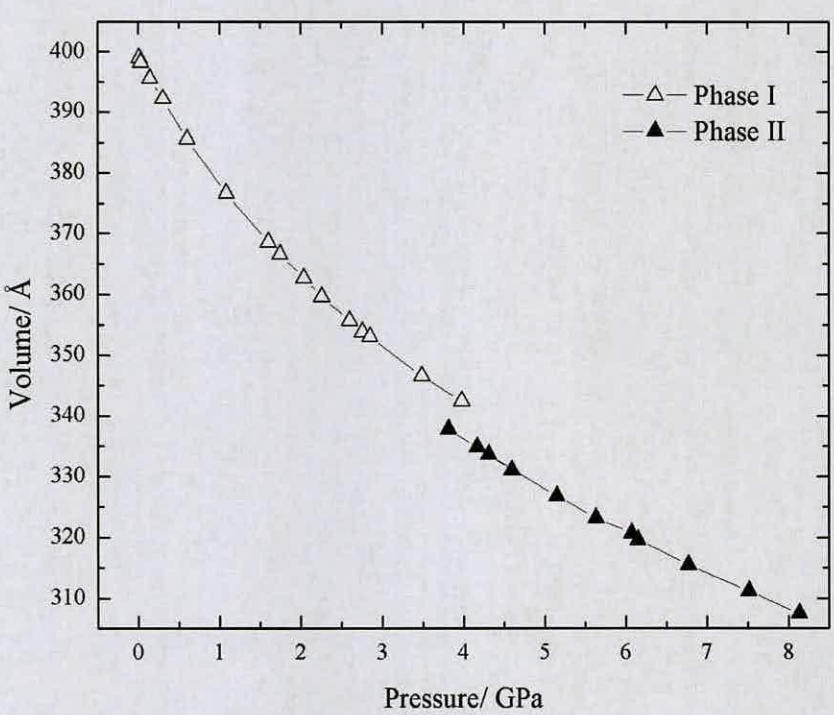

Figure 5.16. Variation of unit cell volume of ND_4ClO_4 with increasing pressure.

The unit cell volume of both phase I and phase II of AP can be fitted to a 3rd order Birch-Murnaghan equation of state. For phase I this gives values of B_0 = 14.91(25) GPa, and B_0'= 7.23(23) GPa, which are in good agreement with previous studies [9, 13]. For phase II B_0 = 22.4(26) GPa, and B_0' = 4.4(5) GPa, indicating that the phase II is significantly less compressible than phase I.

On slow decompression of the sample the high-pressure phase persisted to 3.82 GPa, and transformed back to phase I at 2.76 GPa.

P (GPa)	*a* (Å)	*b* (Å)	*c* (Å)	V (Å^3)
Phase I				
0.01	9.2185(14)	5.8108(9)	7.4504(13)	399.07(7)
0.03	9.2133(13)	5.8075(8)	7.4447(11)	398.34(6)
0.14	9.1868(13)	5.7969(8)	7.4292(11)	395.64(6)
0.30	9.1538(12)	5.7875(8)	7.4038(11)	392.23(6)
0.60	9.0899(11)	5.7621(7)	7.3624(9)	385.62(5)
1.08	9.0054(10)	5.7277(7)	7.3018(9)	376.63(5)
1.60	8.9276(10)	5.6970(7)	7.2472(9)	368.60(5)
2.26	8.8375(10)	5.6634(6)	7.1848(9)	359.60(5)
2.85	8.7699(11)	5.6400(7)	7.1380(10)	353.06(6)
3.49	8.6998(11)	5.6170(7)	7.0908(9)	346.50(5)
3.98	8.6565(21)	5.6022(13)	7.0605(18)	342.40(9)
Phase II				
3.98	7.4577(14)	6.3347(12)	7.1182(17)	336.28(8)
4.60	7.4070(11)	6.3209(9)	7.0734(11)	331.17(6)
5.15	7.3646(11)	6.3051(9)	7.0396(11)	326.88(6)
5.63	7.3267(11)	6.2937(10)	7.0093(12)	323.21(6)
6.15	7.2918(11)	6.2780(9)	6.9815(11)	319.60(5)
6.77	7.2528(13)	6.2587(11)	6.9498(11)	315.47(5)
7.51	7.2074(17)	6.2404(13)	6.2404(13)	311.22(5)
8.13	7.1728(17)	6.2222(14)	6.2222(14)	307.55(5)

Table 5.3. Lattice parameters and density of ND_4ClO_4 as a function of pressure

5.6 Conclusions: Ammonium Perchlorate

A phase transition in ammonium perchlorate has been observed at 4.0 GPa using powder neutron diffraction, Raman spectroscopy and single-crystal X-ray diffraction. The differences in the reported transition pressure between this study and other studies may possibly be attributed to the fact that the neutron diffraction study used perdeuterated ammonium perchlorate. However, this seems unlikely on the basis that the transition pressure observed in the present Raman and X-ray studies on NH_4ClO_4 is very similar to the transition pressure observed for powder neutron diffraction studies on ND_4ClO_4. It seems more likely that the explanation lies in the rather different experimental conditions for each study. Several shock-wave studies have suggested that there is no pressure induced transition, or if there is, it either involves a small volume change or is kinetically slow under the conditions of the experiment. This study has shown that the volume change associated with the phase transition is indeed small.

In particular, the choice of pressure-transmitting medium may be responsible for the difference in the transition pressures between this work and previous studies. One of the most important variables in isothermal direct compression experiments is the pressure-transmitting medium. A mixture of 4:1 methanol:ethanol was selected on account of it providing hydrostatic conditions up to *ca.* 10 GPa. Past experience has shown that pressure-induced phase transitions can be suppressed when fluids such as Fluorinert-FC75 become non-hydrostatic. Recent work by Angel *et al.* [31] studying the effect of high pressure on the width of the (101) reflection of a quartz single-crystal have demonstrated that Fluorinert-FC75 remains hydrostatic only up to

ca. 2 GPa. On the other hand, there have been studies which have shown that conditions of non-hydrostatic pressures can induce phase transitions, e.g. ammonium nitrate. The previous study of ammonium perchlorate by Bridgman which reported a transition at 3.1 GPa used non-hydrostatic shear stresses at elevated temperatures [6]. As such, Bridgman's conditions were very different from those used in the current study.

The study by Peiris *et al.* [13] is the study which involves conditions closest to our own. Energy dispersive X-ray techniques were used in conjunction with either sodium chloride or Fluorinert-FC75 as a pressure-transmitting medium. The authors reported a change in intensities over the range 2.9-3.3 GPa, with the appearance of a new pattern above 3.3 GPa. The rather lower transition pressure in this study is presumably a result of the non-hydrostatic conditions associated with the pressure-transmitting media used. Comparison of these published patterns with an equivalent calculated energy dispersive pattern from our structure of phase II indicated that several of the peaks attributable to phase II are present, although there are several differences in intensity and some additional peaks. The origin of these peaks is not clear, but it may be that the non-hydrostatic conditions caused a transition to a different high-pressure phase. Another possibility is that the high energy X-ray beam used in the energy dispersive experiments may have induced partial decomposition of the sample. Previous work has shown that AP is susceptible to irradiation with X-rays leading to the formation of radical species [32] and plastic deformation of crystals [33], and both of these phenomena might also encourage other phase transitions.

5.7 High-Pressure Powder Neutron Studies: Ammonium Nitrate

5.7.1 Results

High-pressure powder neutron diffraction patterns were collected for ammonium nitrate-d_4 as described in section 5.3.1 on the PEARL beamline at incremental pressure up to 7.85 GPa (Figure 5.17). Deuteration of AN was achieved by repeated recrystallisation from deuterium oxide. Indexing of the first powder pattern confirmed the presence of form IV, with lattice parameters given in Table 5.4.

Crystal System	orthorhombic
Space group	*Pnma*
***a*/Å**	7.4577(4)
***b*/Å**	6.3347(12)
***c*/Å**	7.1182(17)
***α*/°**	90
***β*/°**	90
***γ*/°**	90
***V*/Å^3**	336.28(8)
Z	2
***D$_c$*/g cm^{-3}**	1.73
T/K	293(2)

Table 5.4 Unit cell parameters of ammonium nitrate form IV.

A plot of the Rietveld refinement obtained from the data collected at 0.14 GPa is illustrated in Figure 5.18 (wRp = 0.0474). All subsequent powder patterns could be indexed to the same orthorhombic cell. The use of 4:1 MeOD/EtOD as a pressure-transmitting fluid ensured that hydrostatic conditions were maintained over this pressure range.

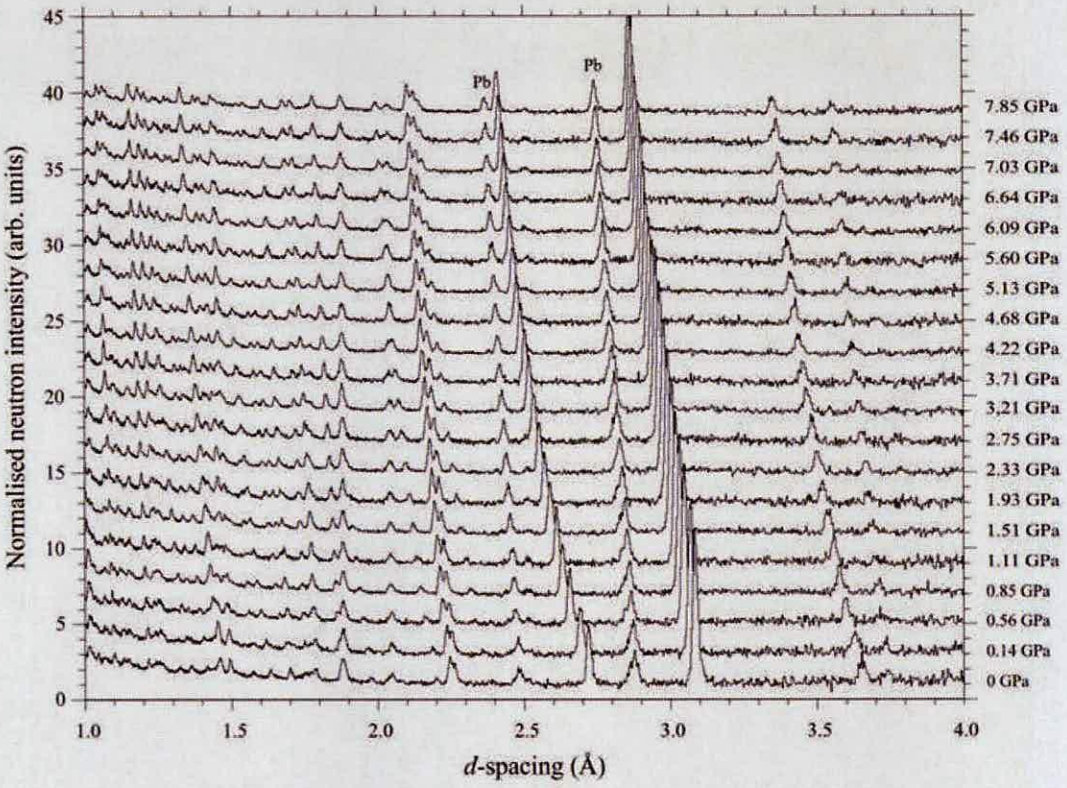

Figure 5.17. Sequence of powder neutron diffraction patterns for ND_4NO_3

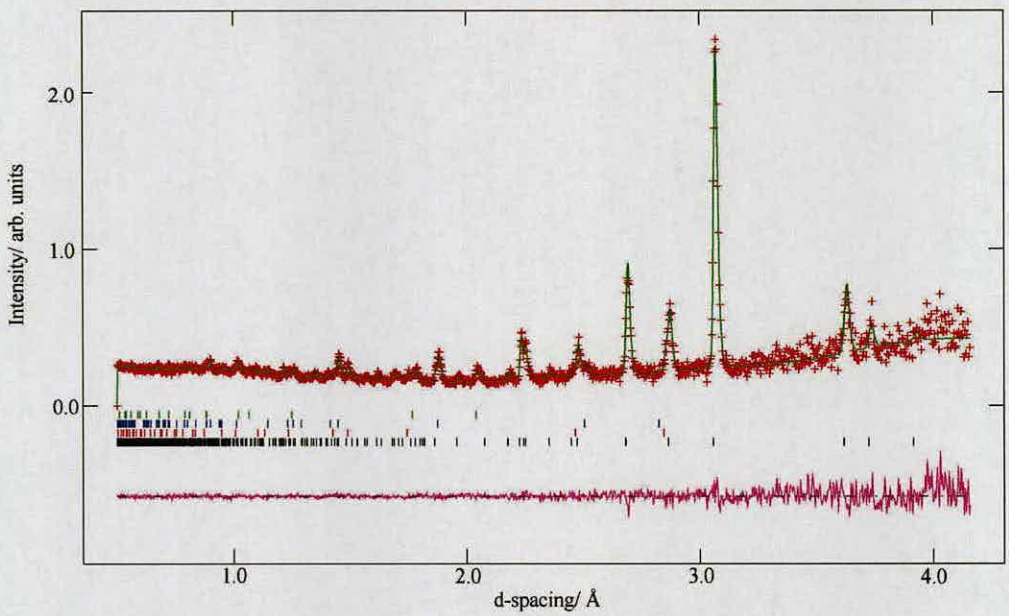

Figure 5.18 Powder neutron pattern at 0.14 GPa of ND_4NO_3. The crosses denote the observed intensities and the solid lines those calculated from the best-fit model of the Rietveld refinement. The tick marks represent the calculated peak positions, (black tick marks signify ammonium nitrate, the red marks correspond to the lead internal pressure marker, and the blue and green tick marks represent tungsten carbide and nickel, respectively). The line below them represents the deviation between observed and calculated intensities.

Figure 5.19 illustrates the variation of lattice parameters over the entire pressure range, and these values are tabulated in Table 5.5. Between 0.00 GPa and 7.85 GPa, the *a*-, *b*-, and *c*- axes decrease by 4.7 %, 11.4% and 5.2%, respectively. Figure 5.20 shows the variation of volume with increasing pressure. The V(p) variation could be fitted to a 3rd order Birch-Murnaghan plot, with $V_0 = 152.9(3)$ Å^3, $B_0 = 16.6(7)$ GPa, and $B_0' = 7.7(4)$. Full-profile Rietveld refinement was possible for all of the powder neutron diffraction patterns.

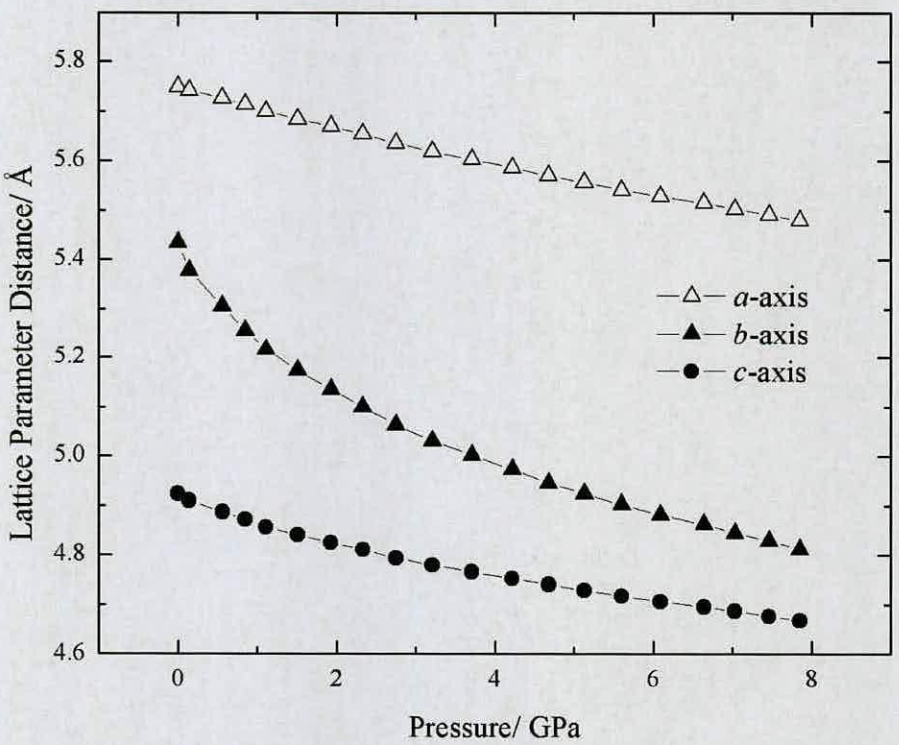

Figure 5.19. Variation of lattice parameters of form IV AN-d_4 with increasing pressure

P (GPa)	*a*/ Å	*b*/ Å	*c*/ Å	*V*/ Å^3
0	5.75015(77)	5.43427(43)	4.92382(61)	153.859(21)
0.14	5.74283(72)	5.37822(45)	4.90994(57)	151.649(20)
0.56	5.72666(67)	5.30605(40)	4.88679(54)	148.490(18)
0.85	5.71365(48)	5.25701(30)	4.87208(39)	146.341(13)
1.11	5.70037(63)	5.21674(40)	4.85685(52)	144.430(17)
1.51	5.68490(46)	5.17350(28)	4.84110(37)	142.381(12)
1.93	5.66998(60)	5.13596(38)	4.82526(47)	140.515(16)
2.33	5.65429(44)	5.09965(29)	4.81082(36)	138.720(12)
2.75	5.63604(54)	5.06262(36)	4.79430(43)	136.797(14)
3.21	5.61888(43)	5.03118(29)	4.77960(34)	135.117(11)
3.71	5.60352(55)	5.00213(37)	4.76644(43)	133.601(14)
4.22	5.58716(42)	4.97371(27)	4.75315(33)	132.085(11)
4.68	5.57048(52)	4.94639(34)	4.74095(41)	130.631(13)
5.13	5.55668(44)	4.92382(27)	4.72891(34)	129.383(11)
5.6	5.54137(56)	4.90256(36)	4.71777(46)	128.167(14)
6.09	5.52764(43)	4.88125(27)	4.70612(34)	126.980(11)
6.64	5.51564(58)	4.86296(36)	4.69576(46)	125.951(14)
7.03	5.50322(44)	4.84543(27)	4.68687(34)	124.978(11)
7.46	5.49139(57)	4.82899(36)	4.67658(46)	124.013(14)
7.85	5.48024(45)	4.81297(28)	4.66846(35)	123.136(11)

Table 5.5 Unit cell parameters of form IV AN-d_4 with increasing pressure.

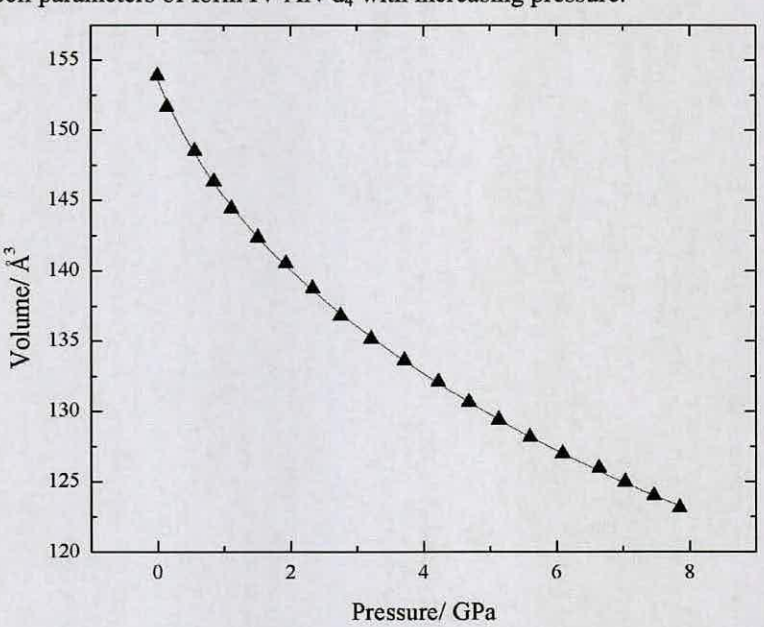

Figure 5.20. Variation of unit-cell volume of form IV AN-d_4 with increasing pressure

5.8 Discussion: Ammonium Nitrate Hydrostatic Studies

The crystal structure of ammonium nitrate is a two-dimensional network of hydrogen bonds between the nitrogen atoms of the ammonium group and the oxygen atoms of the nitrate ions. The asymmetric unit comprises one ammonium ion and one nitrate ion (Figure 5.21). Figure 5.22 shows the crystal structure of AN viewed down the *b*-axis.

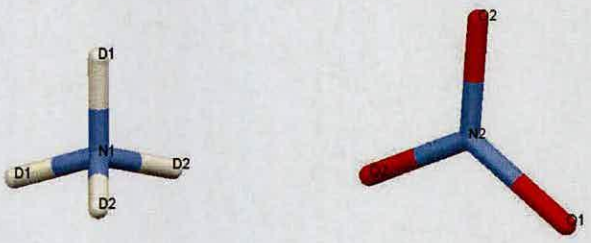

Figure 5.21. Labelled asymmetric unit of form VI of AN

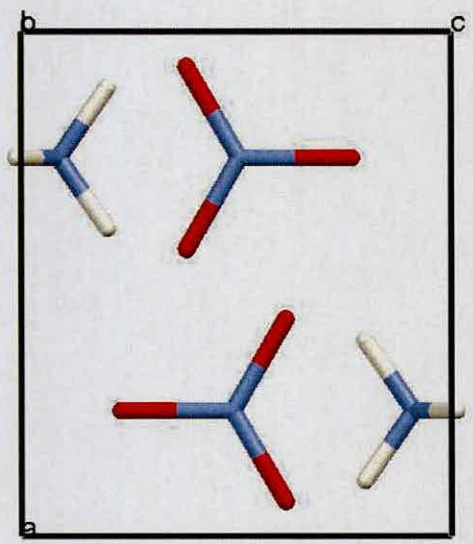

Figure 5.22. Crystal structure of form VI of AN viewed down the *b*- axis.

The hydrogen bonded sheets in AN can be seen more clearly in Figure 5.23, which shows an extended crystal structure of AN viewed down the *a*-axis.

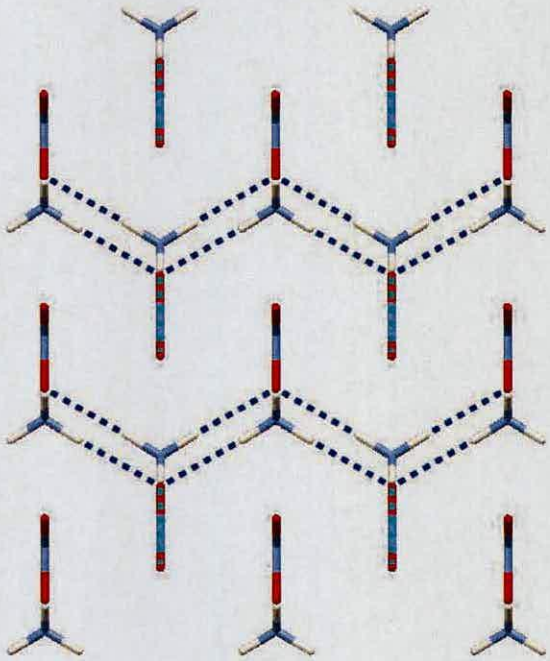

Figure 5.23. Sheets of ammonium ions and nitrate ions viewed down the *a*-axis.

Over the pressure range, there were no changes in either the primary bond lengths or angles for the ND_4^+ and NO_3^- ions. Instead, the application of pressure had the most significant effect on the hydrogen bonding network of AN. The hydrogen bonding network consists of three hydrogen bonding interactions. The variation of these distances with increasing pressure is shown in Figures 5.24, 5.25 and 5.26. All three hydrogen bond lengths, D1...O1, D1...O2, and D2...O1 decrease with increasing pressure. The bond length D2...O1 decreases by 15.9 % over the entire pressure range, significantly more than the two other intermolecular

interactions. This is shown in Figure 5.27. Both the D1…O2 and D2…O1 interactions have a significant component along the *b*-axis and so explains why this axis is the most compressible over this pressure range. All bond length errors represent ±σ.

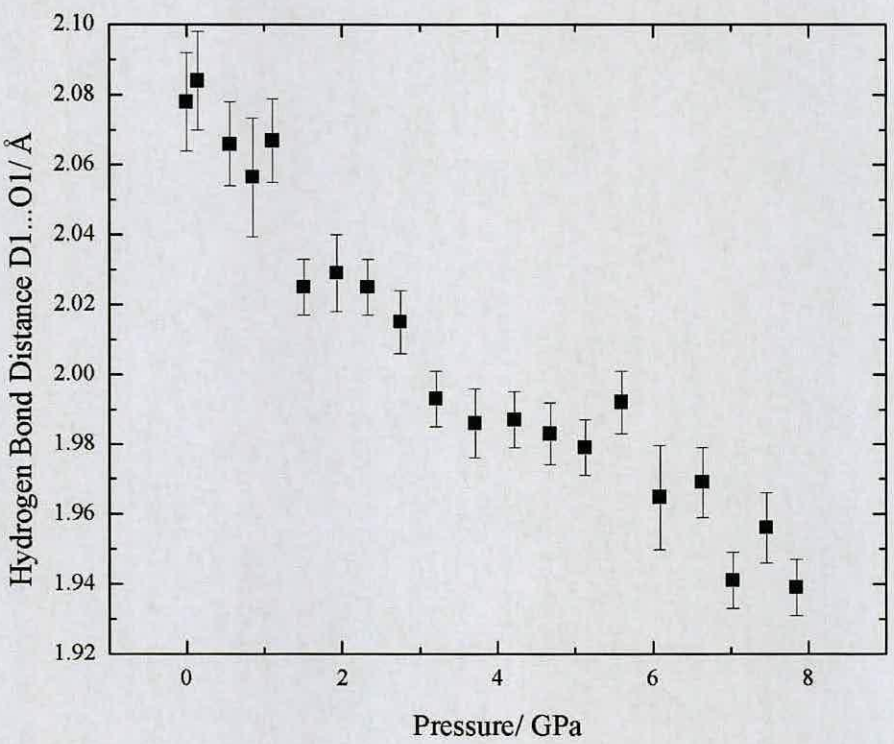

Figure 5.24. Variation of hydrogen bond length D1…O1 in ND_4NO_3

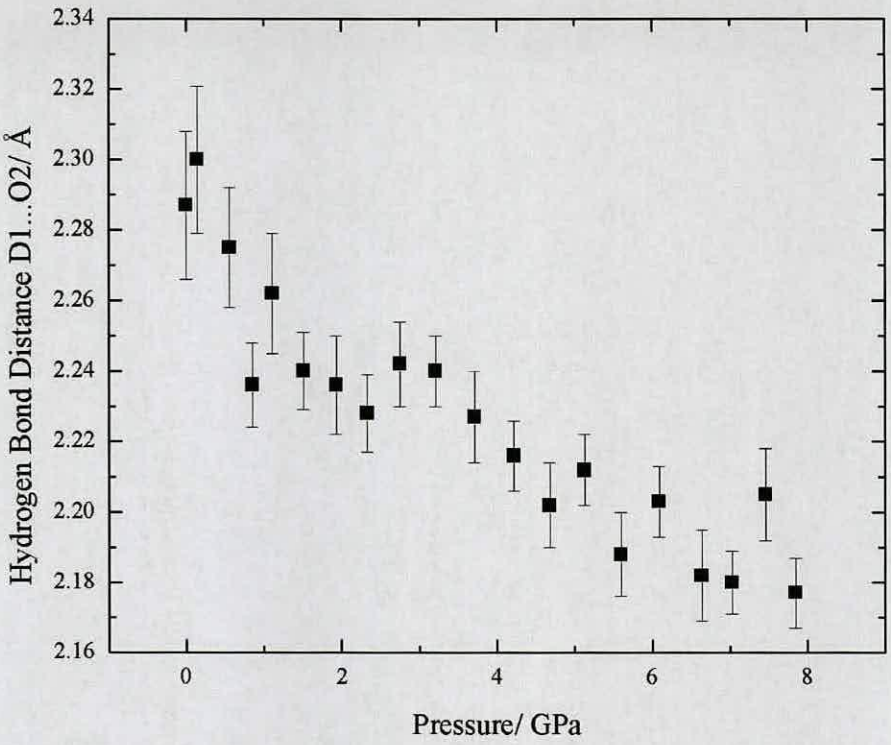

Figure 5.25. Variation of hydrogen bond length D1…O2 in ND_4NO_3

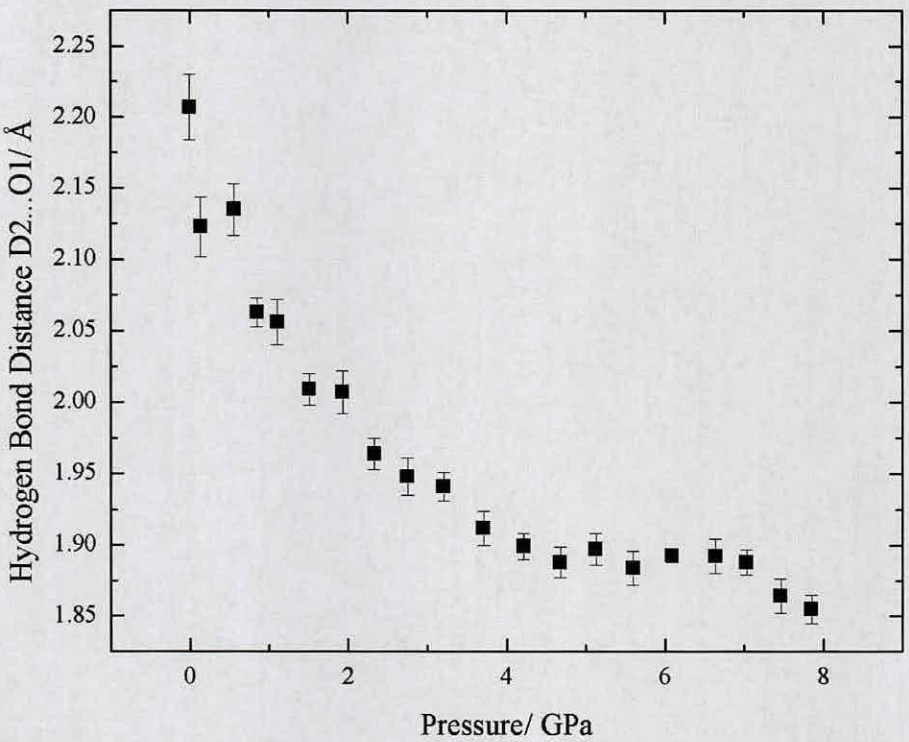

Figure 5.26. Variation of hydrogen bond length D2…O1 in ND_4NO_3

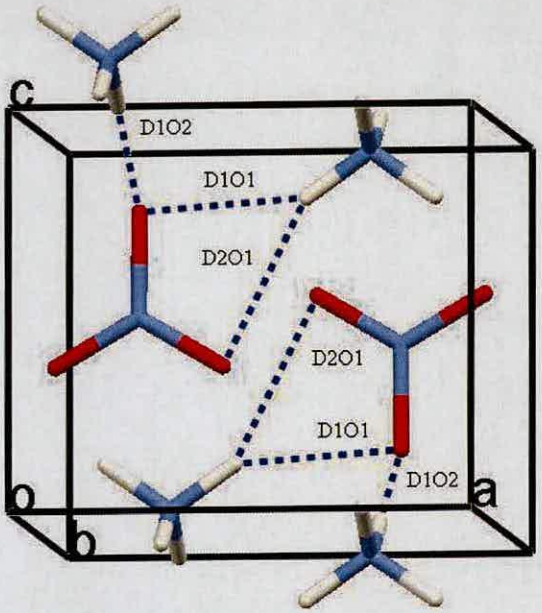

Figure 5.27. Views of crystal structure of ND_4NO_3 showing hydrogen bonds present

5.9 High Pressure Powder X-Ray Studies: Ammonium Nitrate Under Non-hydrostatic Conditions

5.9.1 Experimental

High pressures were generated using a DAC. High pressure powder X-ray diffraction experiments were conducted using a Laue focusing monochromator equipped with an image plate on Station 9.5 at the Daresbury Laboratory (STFC) using apparatus as described by Lennie *et al.* [34]

5.9.2 Results

Although direct compression studies under hydrostatic conditions revealed no phase transitions, reports in the literature suggested that under non-hydrostatic condition, or conditions of high shear, a phase transition did occur [15,16,17]. Studies were initially conducted using Fluorinert-FC75 as a pressure-transmitting medium, with the expectation that conditions would become non-hydrostatic above 1.2 GPa. Powder patterns were obtained between 0.4 GPa and 7.1 GPa (Figure 5.28). The variation of intensities of each pattern can be attributed to preferred orientation of the crystallites exacerbated by the small diameter of the X-ray beam. Inspection of the patterns revealed no distinct changes over the entire range, indicating no phase transition. Further studies were performed on a powdered sample of AN using a diamond anvil cell, in the absence of any pressure-transmitting medium. Powder patterns were collected at incremental pressure steps (Figure 5.29). Significant broadening of the Bragg peaks were observed, especially at higher pressures. However, no changes in the powder pattern up to a pressure of 5.6 GPa were observed.

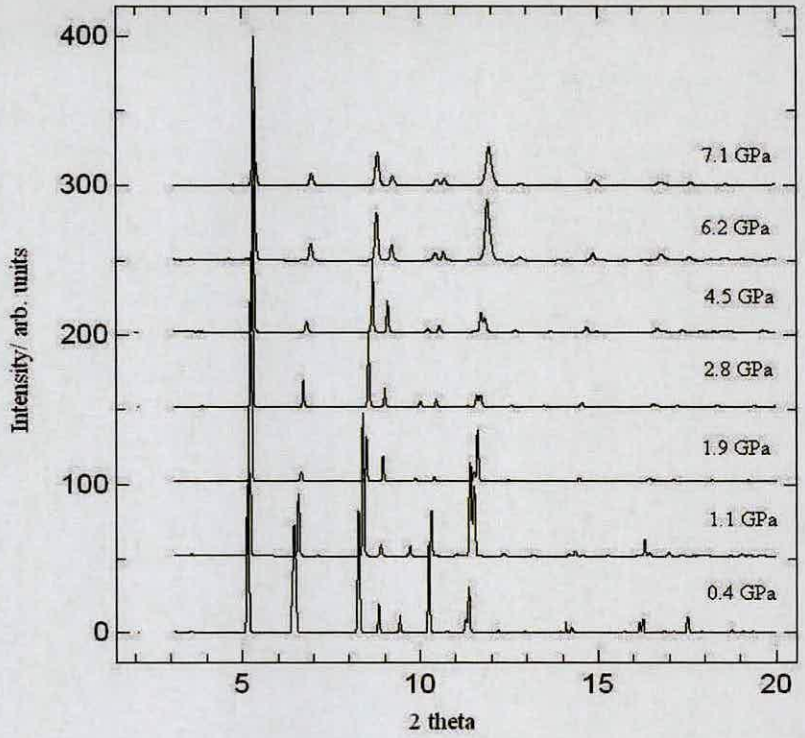

Figure 5.28. Sequence of X-ray powder diffraction patterns for ND_4NO_3 at 298 K using Fluorinert-FC-75 as a pressure-transmitting-medium.

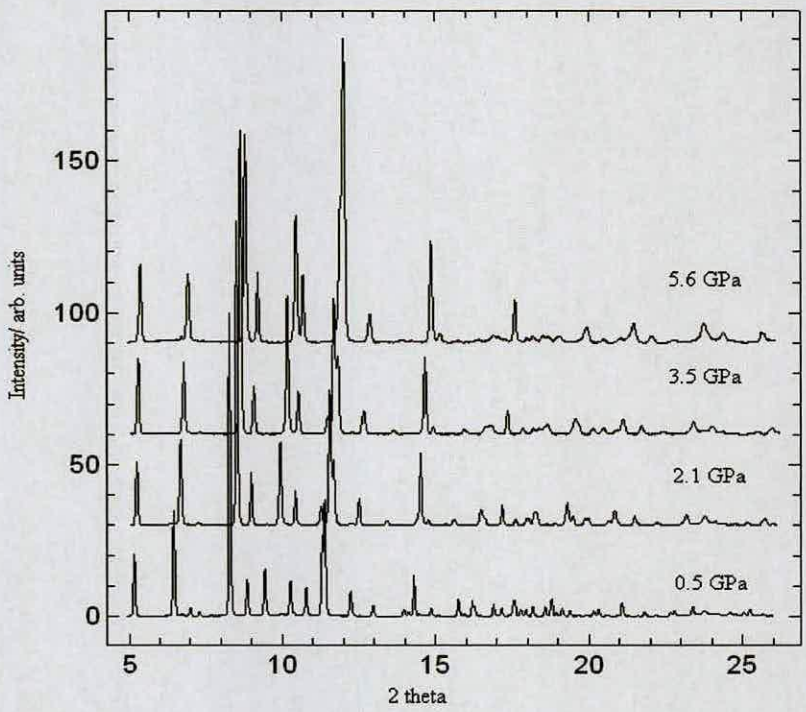

Figure 5.29. Sequence of X-ray powder diffraction patterns for ND_4NO_3 at 298 K, in the absence of a pressure-transmitting-medium.

5.10 Conclusions: Ammonium Nitrate

High-pressure compression studies of AN have been performed under both hydrostatic and non-hydrostatic conditions. The hydrostatic results confirm previous studies that AN does not undergo a phase transition over this pressure interval.

Under non-hydrostatic conditions, it was anticipated that a phase transition might have been induced, but this was not observed. This is presumably because both Fluorinert-FC75 and AN are relatively soft materials and so direct compression in a gasketed cell does not reproduce the conditions encountered when AN is simply compressed between two un-gasketed diamonds as described in the study by Adams *et al* [16]. However, there was some reluctance to perform this experiment on account of the high probability of breaking one or both of the diamonds, but this is a potential area for further exploration.

5.11 References

[1] K. Venkatesen, *Proc. Indian Acad. Sci.*, 1957, *A***46**, 134.

[2] H. G. Smith, H. A. Levy, *Acta Cryst.*, 1962, **15**, 1201.

[3] H. J. Prask, C. S. Choi, *J. Chem. Phys.*, 1974, **61**, 3523.

[4] H. J. Prask and C. S. Choi, N. J. Chesser, and G. J. Rosasco, *J. Chem. Phys.*, 1988, **88**, 5106.

[5] M. Stammler, R. Bruenner, W. Schmidt, and D. Orcutt, *Adv. X-ray Anal.,* 1976, **9**, 170.

[6] P. W. Bridgman, *Proc. Am. Acad. Arts Sci.,* 1937, **72**, 45.

[7] P. W. Richter, C. W. F. T. Pistorius, *J. Solid State Chem.*, 1971, **3**, 434.

[8] M. F. Foltz and J. L. Maienschein, *Mater.Lett.,* 1995, **24**, 407.

[9] F. W. Sandstrom, P. A. Persson and B. Olinger, *Proc. AIP Conf.*, 1994, **309**, 1409.

[10] T. B. Brill and F. Goetz, Laser Raman studies of solid oxidizer behaviour. *Papers in Aeronautics and Astronautics.*, T. L. Boggs, B. T. Zinn, Eds.; American Institute of Aeronautics and Astronautics, 1978, **63,** 3.

[11] G. Yuan, R. Feng, Y. M. Gupta and K. J. Zimmerman, *J. Appl. Phys.*, 2000, **88**, 2371.

[12] J. M. Winey, Y. A. Gruzdkov, Z. A. Dreger, B. J. Jensen and Y. M. Gupta, *J. Appl. Phys.*, 2002, **91**, 5650.

[13] S. M. Peiris, G. I. Pangilinan, T. P. Russell, E. F. Westrum, Jr. and B. H. Justice, *J. Phys. Chem. A.*, 2000, **104**, 1118.

[14] C. S. Choi and H. J. Prask, *J. Appl. Cryst.*, 1980, **13**, 403.

[15] P. W. Bridgman, *Proc. Amer. Acad. Arts Sci.,* 1937, **71**, 387.

[16] D. M. Adams and S. K. Sharma, *J. Chem. Soc., Faraday Trans 2.*, 1976, **72**, 2069.

[17] F. W. Sandstrom, P. A. Persson and B. Olinger, *AIP Conference Proceedings*, 1994, **309**, 1409.

[18] G. J. Piermarini, S. Block, J. D. Barnett, R. A. Forman, *J. Appl. Phys.,* 1975, **46**, 2774.

[19] W. G. Marshall and D. Francis, *J. Appl. Crystallogr.*, 2002, **35**, 122.

[20] J. M. Besson, R. J. Nelmes, G. Hamel, J. S. Loveday, G. Weill, S. Hull, *Physica B.*, 1992, **180–181**, 907.

[21] A. C. Larson, R. B. Von Dreele, *Los Alamos National Laboratory Report* No. LA-UR-86-748., 1987.

[22] L. Merrill, W. A. Bassett, *Rev. Sci. Instrum.*, 1974, **45**, 290.

[23] S. A. Moggach, D. R. Allan, S. Parsons, L. Sawyer, J. E. Warren, *J. Synchrotron Rad.*, 2005, **12**, 598.

[24] A. Dawson, D. R. Allan, S. Parsons, M. Ruf, *J. Appl. Crystallogr.*, 2004, **37**, 410.

[25] Bruker AXS, SAINT, Version 7.01A, Bruker-AXS, Madison, Wisconsin (USA), 2003.

[26] S. Parsons, SHADE. The University of Edinburgh (Scotland), 2004.

[27] G. M. Sheldrick, SADABS, version 2004/1, University of Göttingen (Germany), 2004.

[28] A. Altomare, A., G. Cascarano, C. Giacovazzo, A. Guagliardi, *J. Appl. Cryst.*, 1993, **26**,343.

[29] P.W. Betteridge J. R. Carruthers, R. I. Cooper, C. K. Prout, D. J. Watkin, *J. Appl. Cryst.*, 2003, **36**, 1487.

[30] I. J. Bruno, J. C. Cole, P. R. Edgington, M. Kessler, C. F. Macrae, P. McCabe, J. Pearson, R. Taylor, *Acta. Cryst.*, *B***58**, 389.

[31] R. Angel, *Private communication*, 2007.

[32] B. G. Hegde, A. Rastogi, R. Damle, R. Chandramani and S.V. Bhat, *J. Phys. C.*, 1997, **9**, 3219.

[33] H. L. Bhat, P.J. Herley, D. B. Sheen and J. N. Sherwood, *Appl. X-Ray Topogr. Methods Mater. Sci.*, 1984, **401**.

[34] A. R. Lennie, D. Laundry, M. A. Roberts, G. Bushnell-Wye, *J. Synchrotron Radiation.*, 2007, **14**, 433-438.

Chapter 6

High-Temperature and High-Pressure Studies of Hydroxylammonium Perchlorate

Chapter Six: High-Temperature and High-Pressure Studies of Hydroxylammonium Perchlorate

6.1 Introduction

Hydroxylammonium perchlorate, $[NH_3OH]^+[ClO_4]^-$ (HAP), is an energetic oxidiser used in torpedo propulsion systems. It has been used in The Spearfish Torpedo, a heavy acoustic homing torpedo used by the submarines of the Royal Navy.

The room temperature phase of HAP (phase A) has been characterised by single-crystal X-ray and neutron diffraction [1,2]. The neutron study revealed very large thermal motion of the hydrogen atoms [2]. In addition, two highly metastable forms of HAP formed on warming have been previously identified [1]. A high-temperature phase transition has been reported above 328 K, with the formation of a new phase of HAP, labelled as phase B by the authors. It was reported that the *c*-axis of phase A increases by 3/2 and becomes the *b*-axis of phase B. The full determination of the crystal structure of phase B was not attempted due to its instability - a single crystal deteriorated in the X-ray beam even when held at temperatures in the range 333-363 K. It was also reported that a second metastable phase C formed when phase B was allowed to cool from the melt. Lattice parameters have been reported for these two metastable forms but owing to their instability neither form has been fully structurally characterised. The effects of high pressure on HAP have not been reported in the literature.

The aims of the present studies were therefore to structurally characterise the metastable phases B and C, and to investigate the effects of high pressure on the structure of HAP.

6.2 Synthesis

Hydroxylammonium perchlorate (HAP) was prepared from the reaction between barium perchlorate and hydroxylammonium sulfate, according to equation 6.1 [3]. A solution of barium perchlorate (Sigma Aldrich, 2.5g) was dissolved in 12.5 cm^3 deionized water at ambient temperatures and added to a solution of hydroxylammonium sulphate (Sigma Aldrich, 5g) dissolved in 8.7 cm^3 deionized water.

$$(NH_3OH)_2SO_4(aq) + Ba(ClO_4)_2(aq) \rightarrow 2(NH_3OH)(ClO_4)(aq) + BaSO_4(s) \qquad \text{Equation 6.1}$$

The white precipitate of barium sulphate was filtered off to give an aqueous solution of hydroxylammonium perchlorate. Two small portions of this solution were tested separately with aqueous $BaCl_2$ and aqueous Na_2SO_4 to ensure that no excess SO_4^{2-} or Ba^{2+} remained in solution. The resulting solution was then evaporated at ambient temperature to give a white crystalline powder under vacuum. This powder was then recrystallised three times from D_2O (15 cm^3) under nitrogen. Approximately 3.0 g of HAP was obtained. $[ND_3OD][ClO_4]$ is a deliquescent white solid with a melting point of 383 K. All experiments were conducted with this deuterated sample.

6.3 High-Temperature Powder Neutron Studies

6.3.1 Experimental

Powder neutron diffraction patterns were collected at 293 K and at 343 K using the high-resolution powder diffractometer HRPD [4] at the ISIS spallation source. Approximately 2 g of powder was loaded into a thin-walled suprasic (quartz) ampoule which was subsequently flame-sealed under a pressure of *ca* 50 mmHg He gas. The ampoule was then inserted into a thin walled vanadium can. The can was connected to the centre stick of a standard ISIS cryofurnace and the whole cryofurnace was evacuated to 5 $x10^{-4}$ mbar. The sample temperature was measured using a chromel/alumel thermocouple mounted on the surface of the can approximately 2 cm from the centre of the neutron beam. During all runs the temperature variation was less than 2 K. Data were collected in time-of-flight mode. Initial data analysis was carried out using Le Bail refinement [5], with subsequent full Rietveld analysis was carried out at each temperature using GSAS [6].

6.3.2 Results

The powder neutron diffraction pattern obtained at 293 K could be indexed to the known phase A. The unit cell parameters are given in Table 6.1. The pattern obtained at 343 K could be indexed to a monoclinic unit cell a = 7.52125(18) Å, b = 7.12694(17) Å, c = 24.36608(18) Å, with the most likely space group being $P2_1/n$. The Rietveld refinement of the data at 293 K is given in Figure 6.1 (wRp = 0.0570).

	Phase A[2]	Phase A at 293 K
Crystal System	orthorhombic	orthorhombic
Space group	$P2_1cn$	$P2_1cn$
***a*/Å**	7.52(2)	7.49447(33)
***b*/Å**	7.14(1)	7.12149(27)
***c*/Å**	15.99(2)	15.98189(28)
***α*/°**	90	90
***β*/°**	90	90
***γ*/°**	90	90
***V*/Å^3**	858.55(10)	852.983(9)
Z	8	8
D_c/g cm^{-3}	2.10	2.08
Temp/ K	293	293(2)

Table 6.1 Unit cell parameters of phase A of HAP from previous studies [2] and this work.

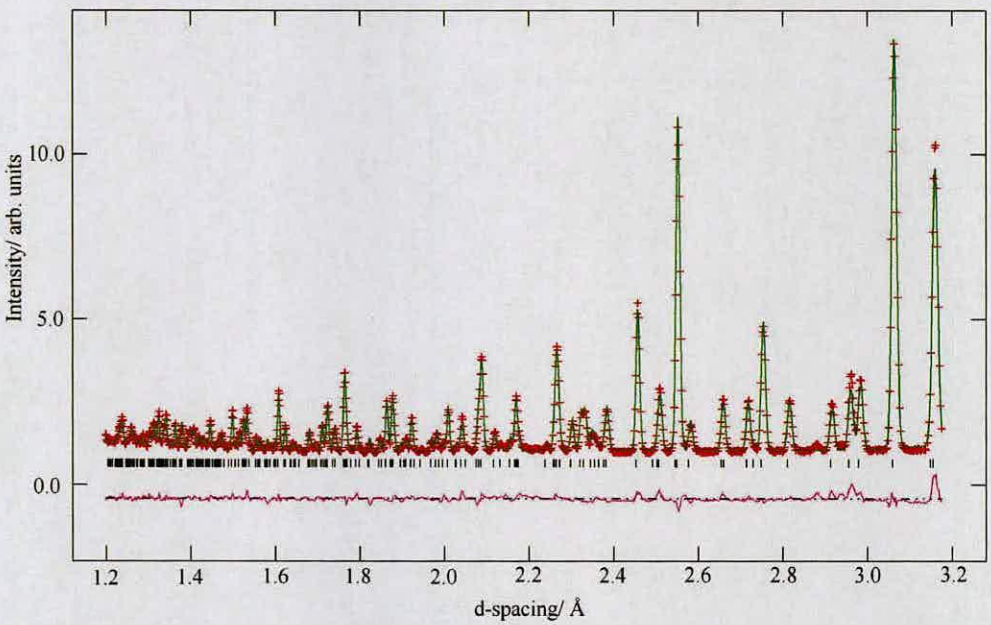

Figure 6.1. Neutron powder diffraction patterns of HAP at 293 K. The crosses denote the observed intensities and the solid lines those calculated from the best-fit model of the Rietveld refinement. The tick marks represent the calculated peak positions and the line below them represents the deviation between observed and calculated intensities

	Phase B [1]	Phase B* (Neutron)
Crystal System	monoclinic	monoclinic
Space group	$P2_1/n$	$P2_1/n$
***a*/Å**	7.52(3)	7.52125(18)
***b*/Å**	24.28(3)	7.12694(17)
***c*/Å**	7.13(3)	24.36608(18)
***α*/°**	90	90
***β*/°**	95(1)	90
***γ*/°**	90	95.1184(32)
***V*/Å^3**	1301.4(3)	1305.89(5)
Z	12	12
D_c/g cm^{-3}	2.08	2.082
T/K	343	343(2)

Table 6.2. Lattice parameters for phase B of HAP. [1] Dickens *et al.* *this work - powder neutron diffraction unit cell parameters for phase B are given in a non-standard settings for ease of comparison between phase A and phase B.

The lattice parameters (Table 6.2) are in good agreement with those proposed by Dickens *et al.* [1]. The unit cell volume implied a structure with z = 12 thus representing a very challenging problem for structure solution using *ab initio* methods. For this reason, single-crystals X-ray diffraction was performed.

6.4 High-Temperature Single-Crystal X-Ray Studies

6.4.1 Experimental

Due to the deliquescent nature of HAP, conventional studies could not be performed. Thus a sample of HAP-d_4 was loaded into a capillary. A single crystal was then grown *via* laser heating at 333 K. Single-crystal data sets were collected on a Bruker SMART APEX CCD diffractometer equipped with an Oxford Cryostream temperature device, using Mo-Kα radiation, λ = 0.71073 Å. Data collection followed the procedures outlined by Dawson *et al.* [7]. Integration of intensities was

performed using SAINT [8]. Absorption corrections were performed using SADABS [9]. Structure solution was achieved *via* direct methods using SIR 92 [10], and full matrix least-squares refinement against $|F|^2$ was performed using CRYSTALS [11]. Hydrogen atoms were placed geometrically and allowed to ride as the parent atom.

Dickens *et al.* [1] reported that it was possible to grow crystals of a metastable phase C when phase B was cooled from the melt. Several attempts were made to grow a single crystal of phase C in this manner. Different cooling rates, and different samples of phase A of HAP were used, but the formation of phase C proved elusive. There may be several reasons for this unsuccessful growth of phase C. One possibility is the use of perdeuterated HAP precludes the formation of phase C. Examples are known where different phase behaviour is observed between deuterated and non-deuterated compounds [12]. Another possibility is the influence that impurities may have on the crystallisation process and hence which polymorph is produced. Given the very high affinity of HAP for water, it is likely that different amounts of water are present in this study and those used by Dickens [1].

6.4.2 Results

Indexing of the reflections from the single crystal of HAP grown at 333K gave a monoclinic unit cell with dimensions similar to that of the neutron data (Table 6.3). Structure solution using direct methods with subsequent full matrix least-squares structure refinement identified the crystal as *phase B of HAP*. Refinement of the powder neutron data was then possible using the X-ray structure as a model.

Rietveld refinement of the powder neutron data at 343 K (wRp = 0.0491) can be seen in Figures 6.2.

	Phase B [1]	Phase B* (Neutron)	Phase B* (single-crystal X-ray)
Crystal System	monoclinic	monoclinic	monoclinic
Space group	$P2_1/n$	$P2_1/n$	$P2_1/n$
***a*/Å**	7.52(3)	7.52125(18)	7.496(4)
***b*/Å**	24.28(3)	7.12694(17)	7.078(4)
***c*/Å**	7.13(3)	24.36608(18)	24.117(11)
***α*/°**	90	90	90
***β*/°**	95(1)	90	90
***γ*/°**	90	95.1184(32)	94.86(3)
***V*/Å^3**	1301.4(3)	1305.89(5)	1275.1(11)
Z	12	12	12
D_c/g cm^{-3}	2.08	2.082	2.086
T/K	343	343(2)	333(2)

Table 6.3. Lattice parameters for phase B of HAP. [1] Dickens *et al.* *this work - powder neutron diffraction and single-crystal diffraction unit cell parameters for phase B are given in a non-standard settings for ease of comparison between the two polymorphs

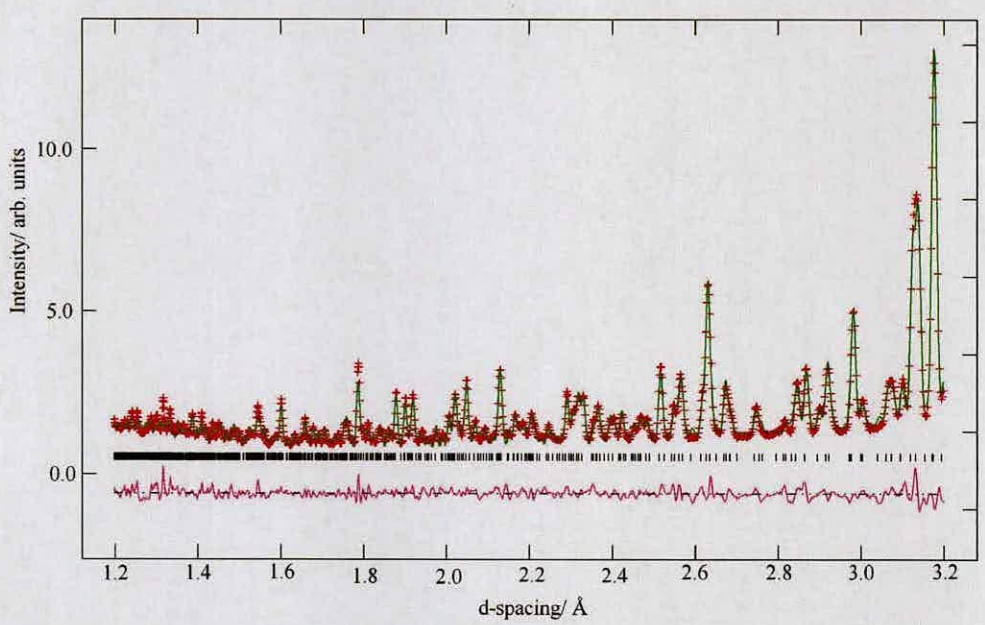

Figure 6.2. Neutron powder diffraction patterns of HAP at 343 K. The crosses denote the observed intensities and the solid lines those calculated from the best-fit model of the Rietveld refinement. The tick marks represent the calculated peak positions and the line below them represents the deviation between observed and calculated intensities

6.5 Discussion: Structures of Phases A and B of Hydroxylammonium Perchlorate

Phase A of HAP is orthorhombic, space group $P2_1cn$ with cell dimensions given in Table 6.2, with two perchlorate ions and two hydroxylammonium ions in the asymmetric unit, as illustrated.

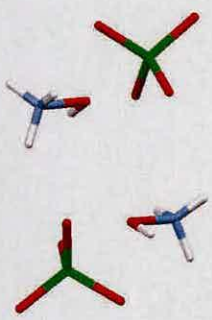

Figure 6.3. Asymmetric unit of phase A of hydroxylammonium perchlorate

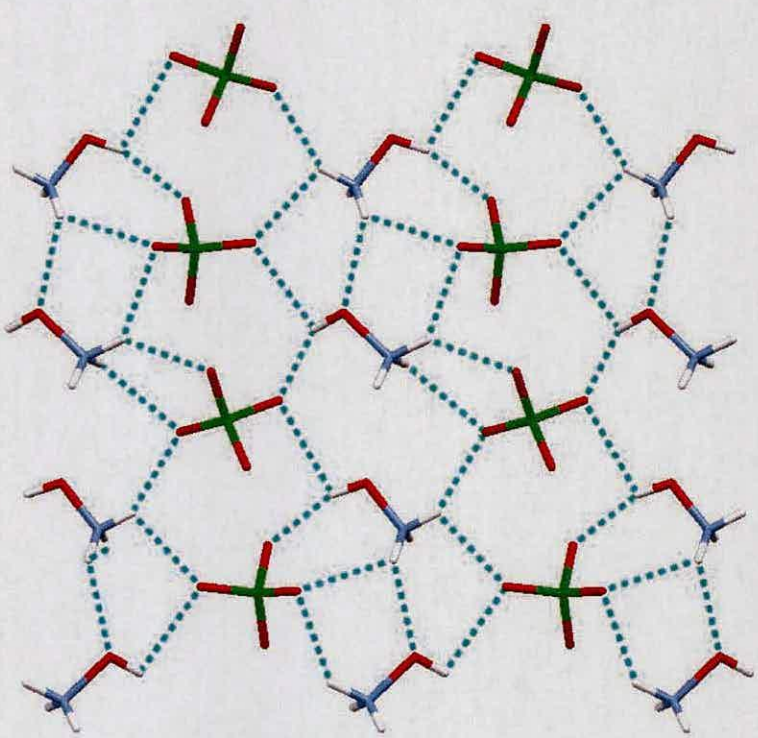

Figure 6.4. Section of HAP phase A crystal structure viewed down the *a*-axis.

The asymmetric unit of phase A can be expanded to form a "sheet", consisting of chains of hydroxylammonium ions and perchlorate ions held together by hydrogen bonding interactions (ranging between 1.85 and 2.5 Å). This is illustrated in Figure 6.4, with hydrogen bonding interactions are shown in blue. The crystal structure of HAP is thus a layered structure, consisting of infinite "sheets" lying above one another. This can be observed in Figure 6.5, where it can be seen that the hydrogen bonding interactions link the "sheets" together. The layers of "sheets" are held together by weaker N-H....O interactions.

The asymmetric unit of phase B can be seen in Figure 6.6, comprising three perchlorate ions and three hydroxylammonium ions. This asymmetric unit can be expanded to form a "sheet" comparable to that of phase A (Figure 6.7).

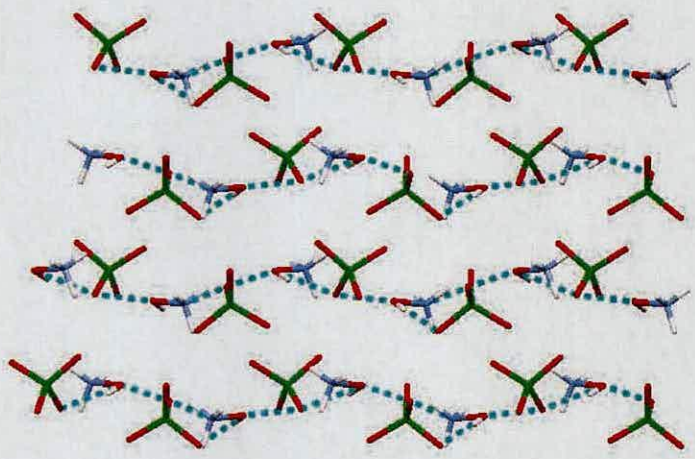

Figure 6.5. Section of phase A crystal structure viewed down the *b*-axis

Figure 6.6. Asymmetric unit of phase B of HAP.

However, phase B of HAP does not form a layered structure. Instead, the molecules instead organise themselves in a "ribbon like" arrangement. This can be seen more clearly in Figure 6.8, where one "sheet" is coloured in black. These "sheets" do not form layers, but stack on top of one another in a "ribbon like" structure. The "ribbon like" packing enables hydrogen bonding interactions to exist between each ribbon.

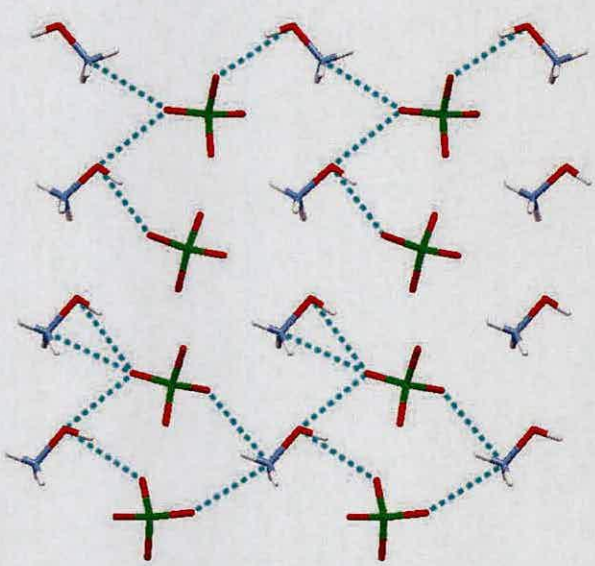

Figure 6.7. Crystal structure of phase B of HAP viewed down crystallographic axis *a*

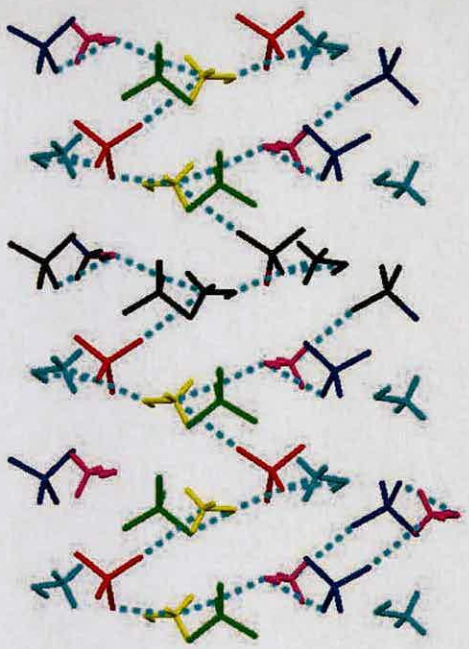

Figure 6.8. Section of crystal structure of phase B HAP viewed down the a-axis. Ions are coloured by symmetry equivalence

Comparison of the crystal structures of phase A and B of hydroxylammonium perchlorate can be seen in Figures 6.9-6.12. There are eight formula units per unit cell in phase A and 12 formula units per unit cell in phase B. There is a marked similarity in the crystal structures of phase A and phase B. As such, phase B is given in the non-standard setting of $P2_1/n$ with the *c*-axis unique, for ease of comparison between the two phases. Examination of the two structures reveals that the *a*- and *b*-axes do not alter significantly, but the *c*-axis in phase B is 50% longer.

A projection down the *a*-axis of phase A and phase B shows similar packing arrangements, with chains of hydroxylammonium ions and perchlorate ions running parallel to the *c*-axis (Figure 6.9).

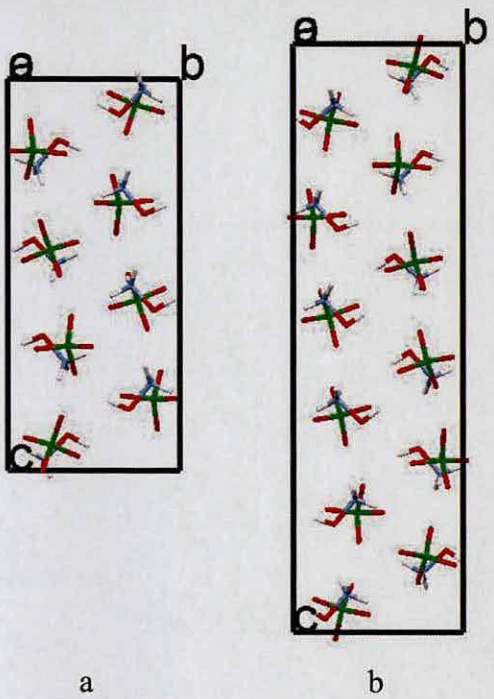

Figure 6.9. Crystal structure of phase A(a) and B(b) viewed down the *a*-axis

However, the two structures do show a few subtle differences. In both phases, there is the presence of an *n* glide symmetry operation. In phase A, this occurs every two molecules of HAP, whereas in phase B the glide occurs every 3 molecules. This can be observed more clearly in Figure 6.10, where glides are shown in purple (with the *n* glide perpendicular to the *c*-axis, and the *c* glide perpendicular to the *b*-axis), 2_1 screw axes in red, and inversion centres shown in black. This manifests itself in a slightly different packing motif in the two structures. Inspection of the chains of perchlorate and hydroxylammonium ions running parallel to the *c*-axis, shows that two consecutive NH_3OH^+ have the same orientation, which then changes as a result of the *n* glide. In phase B, three consecutive NH_3OH^+ groups have the same orientation, before changing as a result of the *n* glide.

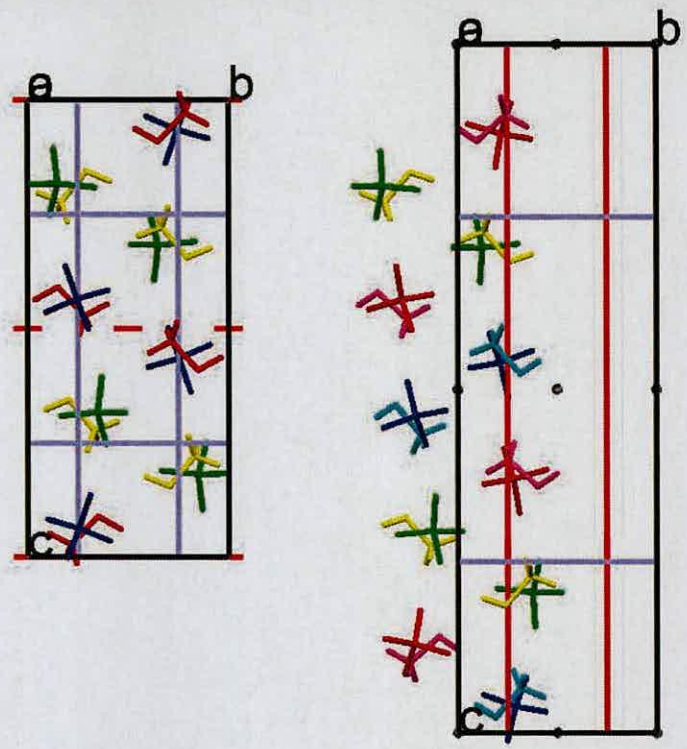

a b

Figure 6.10. Crystal structure of phase (a) and B(b) viewed down the *a*-axis, showing symmetry elements present in each phase

The other point of note is that in phase B there is the presence of an inversion centre, instead of the 2_1 screw axis present in phase A. It is this symmetry element that is responsible for the difference in packing.

Viewing the structures of phase A and B along the *b*-axis illustrates a marked similarity (Figure 6.11). However closer inspection shows that there are some differences. As mentioned earlier, in phase A the chains of NH_3OH^+ ions and perchlorate ions lie in the plane of the *c* glide. In phase B, there is the presence of an inversion centre between the chains running parallel to the *c*-axis.

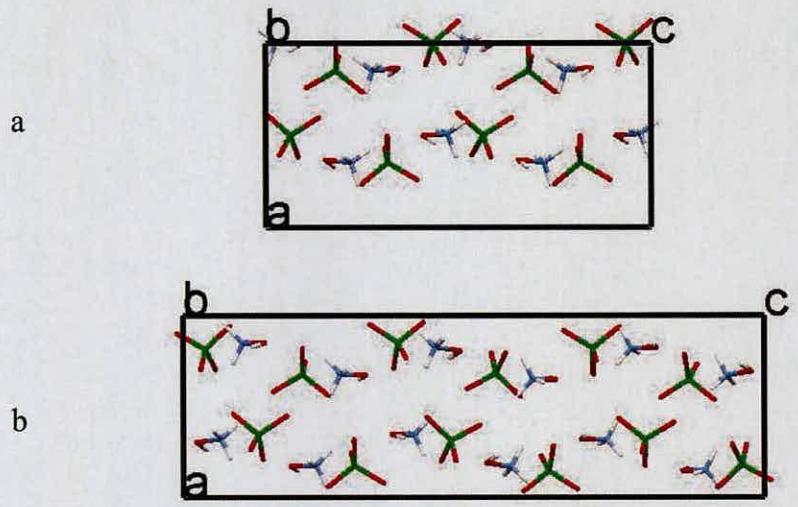

Figure 6.11. Crystal structure of phase A(a) and phase B(b) of HAP viewed down the *b*-axis

A consequence of the inversion centre is that the perchlorate ion circled in Figure 6.12 in phase A, "twists" to the right in phase B. A result of this is that O10 is able to move closer to the molecules in the next layer. Thus O10 is now able to participate in the hydrogen bonding network forming a hydrogen bond with H193 (shown in red in Figure 6.12). However, the consequence of the "twisting" perchlorate group is that O9 is no longer able to contribute to the hydrogen bonding between the "sheets" (shown in blue in Figure 3.12), effectively ending the layers of hydrogen bonding seen in phase A. Thus the "ribbon like" packing observed in phase B is a result of the "twisting" of the circled perchlorate group, which changes the direction of the hydrogen bonding network.

Another point to note is that there are no significant changes in the interatomic distances associated with the perchlorate or hydroxylammonium groups

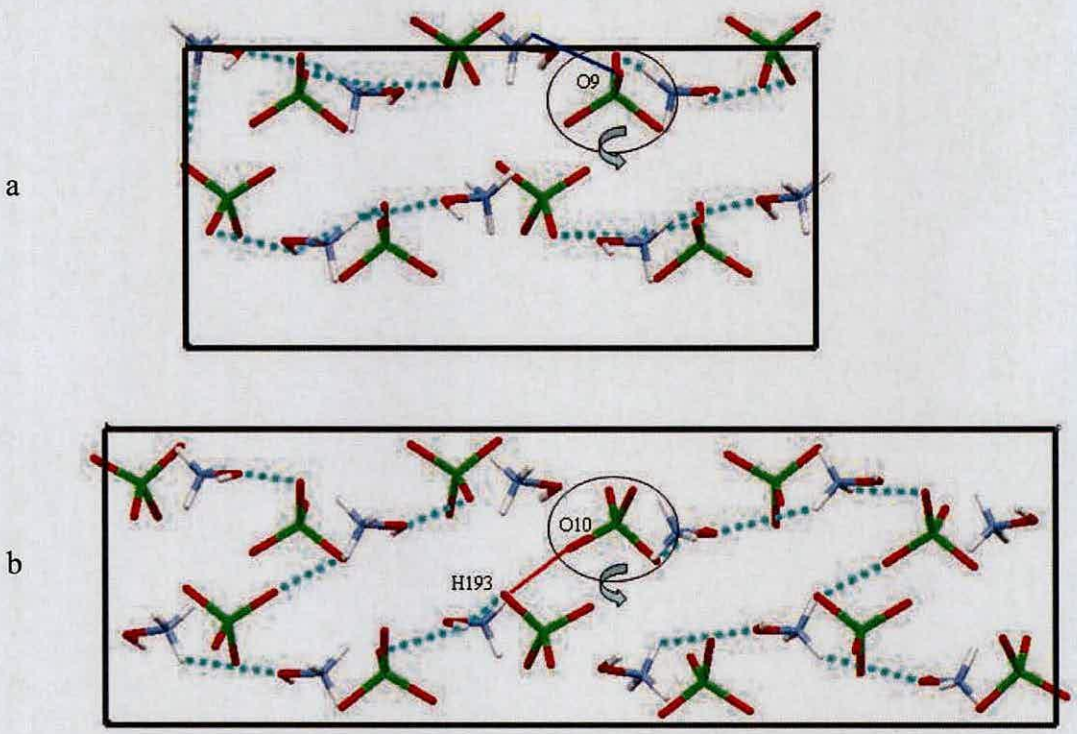

Figure 6.12. Crystal structure of phase A(a) and phase B(b) of HAP viewed down the *b*-axis, illustrating symmetry elements present in both phases.

6.6 High-Pressure Powder Raman Spectroscopy

6.6.1 Experimental

High-pressure Raman studies were performed using a a Jobin-Yvon LabRam 300 instrument equipped with a 50 mW He-Ne laser of wavelength 632.8 nm. Scans with acquisition times of 30 mins were performed in incremental pressure steps between 1.0 GPa and 7.2 GPa. High pressures were generated using a Merrill-Bassett diamond anvil cell (DAC) [13] equipped with 600 μm culet diamonds and a

tungsten gasket. A powdered sample and small ruby chip were loaded into the DAC, together with the pressure-transmitting medium HT70 [14]. The pressure applied to the sample was determined by the ruby fluorescence method [15] using a 632.8 nm excitation line from a He-Cd laser. The fluorescence was detected by the Jobin-Yvon LabRam 300.

Due to the deliquescent nature of HAP, loading of the powdered sample of deuterated HAP was undertaken in a glove box. The pressure-transmitting medium HT70 was used on account of the solubility of HAP in standard pressure-transmitting fluids, such as a 4:1 mixture of MeOH/ EtOH.

6.6.2 Results

It was not possible to obtain an ambient pressure data point, due to the fact that the DAC was loaded in a glove box. Figure 6.13 shows the sequence of Raman spectra with increasing pressure. From 1.0 GPa to 2.4 GPa, the vibrational frequencies increase with pressure. Above 2.4 GPa, a shoulder appears on the band at 930 cm^{-1}. This band is the degenerate Cl-O (T_2) stretching mode. Splitting of this band therefore implies a reduction in the local symmetry of the ClO_4^- ion thereby removing the degeneracy of the T_2 mode. This could be indicative of a phase transition. No further changes, other than pressure induced broadening were observed until 5.5 GPa, were some indication of splitting of the band near 1000 cm^{-1} is seen. At 6.9 GPa, this splitting is very noticeable. This may be evidence for a further phase transition.

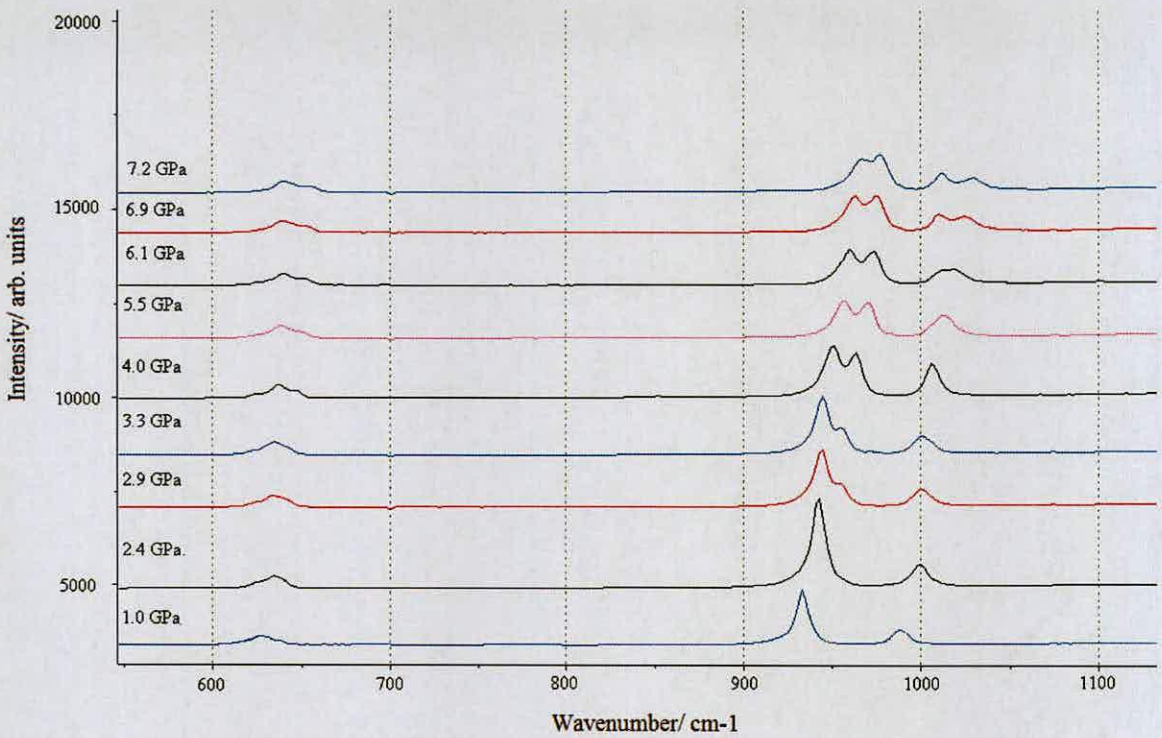

Figure 6.13. Raman spectra of HAP as a function of pressure and intensity

6.7 High-Pressure Powder X-Ray Studies

6.7.1 Experimental

High pressures were generated using a DAC as described earlier. High-pressure powder X-ray diffraction experiments were conducted using a Laue focusing monochromator equipped with an image plate on Station 9.5 at the STFC Daresbury Laboratory Synchrotron Radiation Source. The apparatus has been described by Lennie *et al.* [16]

6.7.2 Results

Powder patterns were obtained at increasing pressures between 0.5 GPa and 6.4 GPa (Figure 6.14). It proved possible to fit the first powder pattern to the known

phase A of HAP using a Le Bail [5] refinement in GSAS [6], and this phase persisted until 1.9 GPa. The unit cell parameters for the first three data points are given in Table 6.4.

	0.5 GPa	**1.0 GPa**	**1.9 GPa**
Crystal System	orthorhombic	orthorhombic	orthorhombic
Space group	$P2_1cn$	$P2_1cn$	$P2_1cn$
***a*/Å**	7.50(13)	7.43(8)	7.41(13)
***b*/Å**	7.05(18)	7.01(18)	6.98(8)
***c*/Å**	16.04(8)	16.00(9)	15.93(36)
***α*/°**	90	90	90
***β*/°**	90	90	90
***γ*/°**	90	90	90
***V*/Å^3**	849.7(25)	834.6(18)	824.8(21)
D_c/g cm^{-3}	2.10	2.12	2.15
T/K	293(2)	293(2)	293(2)

Table 6.4 Unit cell parameters for phase A of HAP at 0.5, 1.0 and 1.9 GPa

Inspection of Table 6.4 shows that the *c*-axis is the most compressible over the pressure range 0.5 to 1.9 GPa. This could be expected, since it is the *c*-axis in phase A of HAP which alters as a result of temperature. On increasing the pressure to 2.3 GPa new peaks were observed to grow in the powder pattern indicating a new phase. This pressure of transition is in good agreement with the changes seen in the Raman data. Unfortunately indexing of this new pattern was not achievable-possibly due to broadening of the Bragg peaks. Pressure was further increased to 3.1 GPa, and a further change in the powder pattern was seen, showing a further change in phase. At this point significant broadening was observed, and again indexing could not be achieved. No further change in the powder patterns was observed up to a

pressure of 6.4 GPa. On account on the lack of indexing and structural information possible from these powder patterns, single-crystal X-ray studies were undertaken.

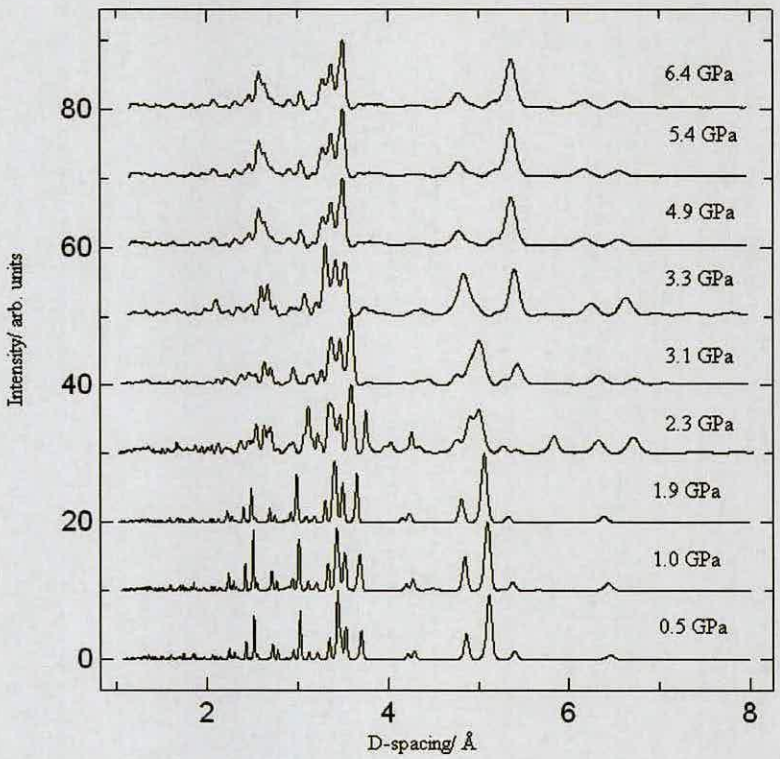

Figure 6.14. Hydroxylammonium perchlorate X-ray powder patterns as a function of pressure and intensity

6.8 High-Pressure Single-Crystal X-Ray Studies

6.8.1 Experimental

A DAC was again utilised to create high pressures. The ruby fluorescence method was used to measure pressure [15]. High-pressure data sets were collected using ω-scans in 12 settings of 2θ and φ with step size 0.3˚ for 30 s [17]. Studies were performed at the STFC Daresbury Laboratory Synchrotron Radiation source on station 9.8 (λ = 0.6765 Å) using a Bruker APEX II diffractometer. All single-crystal data sets were processed according to the procedure described by Dawson *et* al [7].

6.8.2 Results

Indexing of reflections obtained from single-crystal X-ray diffraction at 0.1 GPa confirmed the presence of phase A of HAP. The pressure was then increased to 2.4 GPa. Many more reflections were observed but indexing was not possible suggesting destruction of the crystal. This was confirmed by visual observation that showed the crystal of HAP had cracked in several places. It is clear that the crystal of HAP underwent a destructive transition. The pressure at which the destruction of the single crystal occurred is in good agreement with both Raman and X-ray powder measurements.

6.9 Conclusions

Work has been undertaken on temperature and pressure induced polymorphism of hydroxylammonium perchlorate. A new high temperature phase B of HAP has been identified and structurally characterised for the first time, using both neutron powder diffraction and single-crystal X-ray diffraction.

Further high-pressure phases have been identified. A change in both the Raman spectra and the X-ray powder patterns was seen at approximately 2.4 GPa, indicative of a phase transition. This was also observed in the single-crystal X-ray diffraction studies, where it was apparent that the transition was destructive. A further change in the X-ray powder patterns was seen at 3.1 GPa, and it is likely that this is due to a further transition. A discontinuity was observed in the Raman spectrum at 6.9 GPa, which was not seen in the X-ray powder patterns. This could be evidence for another transition. However, at this pressure significant broadening

of the Raman peaks was observed, which led to a marked loss in resolution, and hence difficulties in identifying changes in other peaks. Furthermore, under these very non-hydrostatic conditions inevitably that sample will be subjected to severe stresses and strains. These also may be responsible for changes in the Raman spectra.

On account of the lack of structural data available for the high-pressure phases of hydroxylammonium perchlorate, further neutron powder diffraction data would be particularly useful. However, this may be hampered by the difficulty of loading such a deliquescent material into a Paris-Edinburgh cell.

6.10 References

[1] B. Dickens, *Acta Cryst.,* 1969, ***B*25**, 1875-1882

[2] E. Prince, B. Dickens, J. J. Rush, *Acta Cryst.*, 1974. ***B*30**, 1167

[3] Process for producing concentrated solutions of hydroxylammonium nitrate and hydroxylammonium perchlorate, United States Patent 4066736.

[4] R. M. Ibberson, W. I .F. David, K. S. Knight, *The High-Resolution Powder Diffractometer (HRPD) at ISIS-a User Guide.* Report RAL-92-031. Rutherford Appleton Laboratory, Chilton, Didcot, England.

[5] A. Le Bail, H. Duroy, J. L. Fourquet, *Mater. Res. Bull.*, 1988, **23**, 447.

[6] A. C. Larson, R. B. Von Dreele, *Los Alamos National Laboratory Report* No. LA-UR-86-748. 1987.

[7] A. Dawson, D. R. Allan, S. Parsons, M. Ruf, *J. Appl. Crystallogr.*, 2004, **37**, 410.

[8] Bruker AXS, SAINT, Version 7.01A, Bruker-AXS, Madison, Wisconsin (USA), 2003.

[9] G. M. Sheldrick, SADABS, version 2004/1, University of Göttingen (Germany), 2004.

[10] A. Altomare, A., G. Cascarano, C. Giacovazzo, A. Guagliardi, *J. Appl. Cryst.*, 1993, **26**, 343.

[11] P.W. Betteridge J. R. Carruthers, R. I. Cooper, C. K. Prout, D. J. Watkin, *J. Appl. Cryst.*, 2003, **36**, 1487.

[12] D. Semmingsen, J. Feder, *J.: Solid State Commun.*, 1974, **15,** 1369.

[13] L. Merrill, W. A. Bassett, *Rev. Sci. Instrum.*, 1974, **45**, 290.

[14] A. J. Davidson, D. Francis, W. G. Marshall, C. R. Pulham, unpublished results, 2006.

[15] G. J. Piermarini, S. Block, J. D. Barnett, R. A. Forman, *J. Appl. Phys.*, 1975, **46**, 2774.

[16] A. R. Lennie, D. Laundry, M. A. Roberts, G. Bushnell-Wye, *J. Synchrotron Radiation.*, 2007, **14**, 433.

[17] S. A. Moggach, D. R. Allan, S. Parsons, L. Sawyer, J. E. Warren, *J. Synchrotron Rad.*, 2005, **12**, 598.

Chapter 7

High-Pressure Studies of Thiourea Dioxide

Chapter 7: High-Pressure Studies of Thiourea Dioxide

7.1 Introduction

The use of high pressure has been shown to be a versatile way of inducing phase transitions and changes in physical properties of a wide variety of materials. This is because high pressure is a particularly effective method for tuning intermolecular and interatomic separations in crystal structures. Since polymorphism in molecular materials often arises through differences in the hydrogen bonding environment of the molecule, the knowledge gained through understanding of the response of hydrogen bonds to pressure may lead to better prediction and control of polymorphism in materials.

While the structures of many elements at high pressure have been extensively studied, there have been relatively few examples of high-pressure structural studies of simple molecular compounds. This represents a remarkable gap in the field of high-pressure, in particular since recent results from groups at Edinburgh and ISIS on simple organic compounds such as amines, ketones, alcohols and mineral acids have shown very rich and interesting phase behaviour [1,2]. For example, recent results obtained for urea and thiourea using high pressure neutron diffraction has shown very rich high-pressure behaviour [3]. In the former case, full structure solutions have been obtained for the previously known phase III and for two completely new and distinct phases IV and V, which are first formed at 2.8 and 7.2 GPa, respectively. In the case of thiourea, a recent X-ray structure of phase VI, a surprisingly complex structure of the ambient-pressure orthorhombic phase V, was confirmed and shown to be unexpectedly persistent in that it appears to be the stable phase of thiourea up to

6 GPa. At higher pressures, phase VI transforms into a completely new orthorhombic phase VII. In the light of these results, work has been extended to study a related molecule, thiourea dioxide. Thiourea dioxide is a reducing agent used in the photographic industries. No previous high pressure studies have been reported on thiourea dioxide.

A particular point of interest of thiourea dioxide is that it possesses an abnormally long C-S bond of 1.891(18) Å. This is longer than both a typical C-S bond length and a typical C=S bond length. Previous work attributed this abnormally long carbon sulfur bond in solution to the presence of two tautomers of thiourea-dioxide (Figure 7.1) [4].

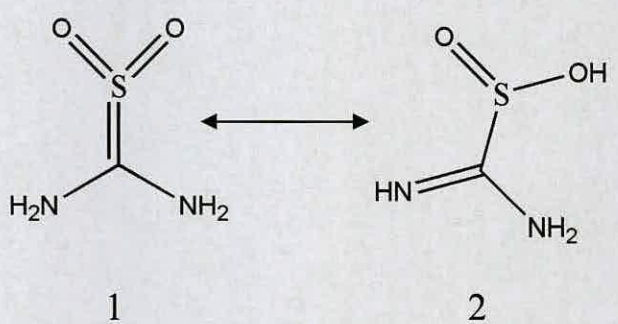

1 2

Figure 7.1 Tautomers of thiourea dioxide

However, this is not observed in the solid state. The bond lengths from an ambient pressure powder neutron study of thiourea dioxide performed at ISIS are shown in comparison with bond lengths for thiourea in table 3.1. The distances obtained for thiourea dioxide are in good agreement with previous studies [4,6].

	Thiourea dioxide [a]	Thiourea [5]
C-S	1.891(18) Å	1.746(9) Å
S-O	1.501(4) Å	N/A
C-N	1.310(4) Å	1.350(4) Å
N-H(2)	1.012(7) Å	1.022(11) Å
N-H(1)	1.029(7) Å	1.022(7) Å

Table 7.1 Selected bond lengths for thiourea dioxide [[a] this work] - and thiourea [5]

It seems more likely that the increased length of the C-S bond in thiourea dioxide could be attributed to the hydrogen bonding found in the solid state between the nitrogen and oxygen atoms, i.e. the lack of tautomer 1. This also correlates well with the observation that the S=O distances in thiourea dioxide are longer than the typical bond lengths. A more realistic representation of thiourea dioxide is given in Figure 7.2, demonstrating that the carbon sulfur bond is closer to a single bond in character.

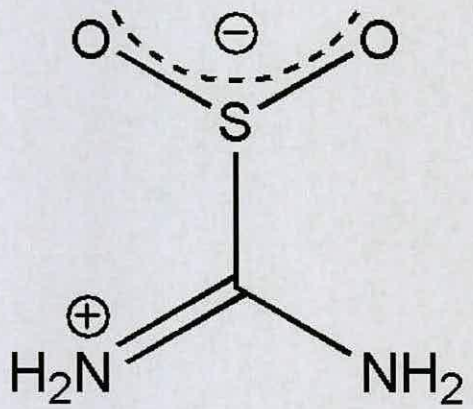

Figure 7.2 Molecular structure of thiourea dioxide under ambient conditions

The molecules in the ambient pressure crystal structure (phase I) of thiourea dioxide are hydrogen bonded in a three-dimensional framework. There are two distinct types of hydrogen bonded interactions, H(1)....O of 1.833(4) Å, and H(2)...O of 1.899(4) Å which are shown in Figure 7.3.

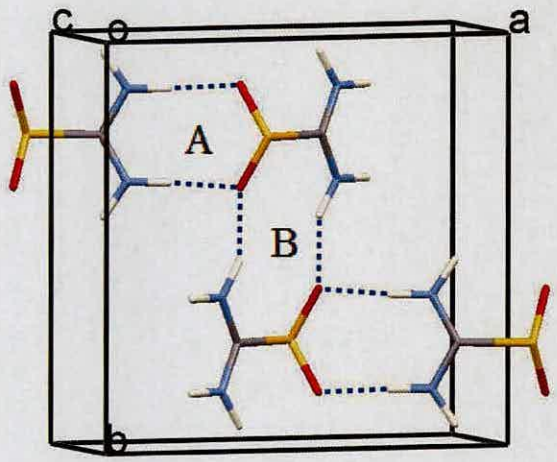

Figure 7.3. Crystal structure of ambient pressure phase I of thiourea dioxide. Hydrogen bonds shown in blue. A corresponds to H(1)....O, B to H(2)...O

7.2 High-Pressure Powder Neutron Studies

7.2.1 Experimental

The thiourea dioxide samples used in this work were obtained from Sigma-Aldrich (99.99%, checked by x-ray powder diffraction). Deuteration was achieved by recrystallisation of 5 g of thiourea dioxide from D_2O (99 at % D). Neutron powder diffraction data were collected using the high flux, medium-resolution time-of-flight diffractometer, HiPr, on the PEARL beamline at the ISIS Neutron Facility, Rutherford Appleton Laboratory. High pressures were generated using a Paris–Edinburgh cell [7]. A lightly ground sample was loaded into an encapsulated TiZr gasket [8]. Pressures were determined from a series of measurements made with NaCl as an internal standard [9]. A 4:1 mixture by volume of deuterated methanol and deuterated ethanol was used as a pressure-transmitting medium. Powder patterns

were recorded in the range from 0.22 GPa to 7.29 GPa. The cell was used in a transverse geometry giving access to scattering angles in the range $83^{\circ} < 2\theta < 97^{\circ}$. Data analysis was performed by use of the Rietveld method using the GSAS suite of programs [10]. All atoms were refined with isotropic displacement parameters. All bond lengths and bond angles were restrained to values observed in the ambient structure of thiourea dioxide [4, 6]. Structures were visualised using the program MERCURY [11].

7.2.2 Results

Diffraction patterns were collected at incremental steps between 0.22 GPa and 7.29 GPa. Figure 7.4 shows powder neutron patterns as a function of pressure and normalised neutron intensity.

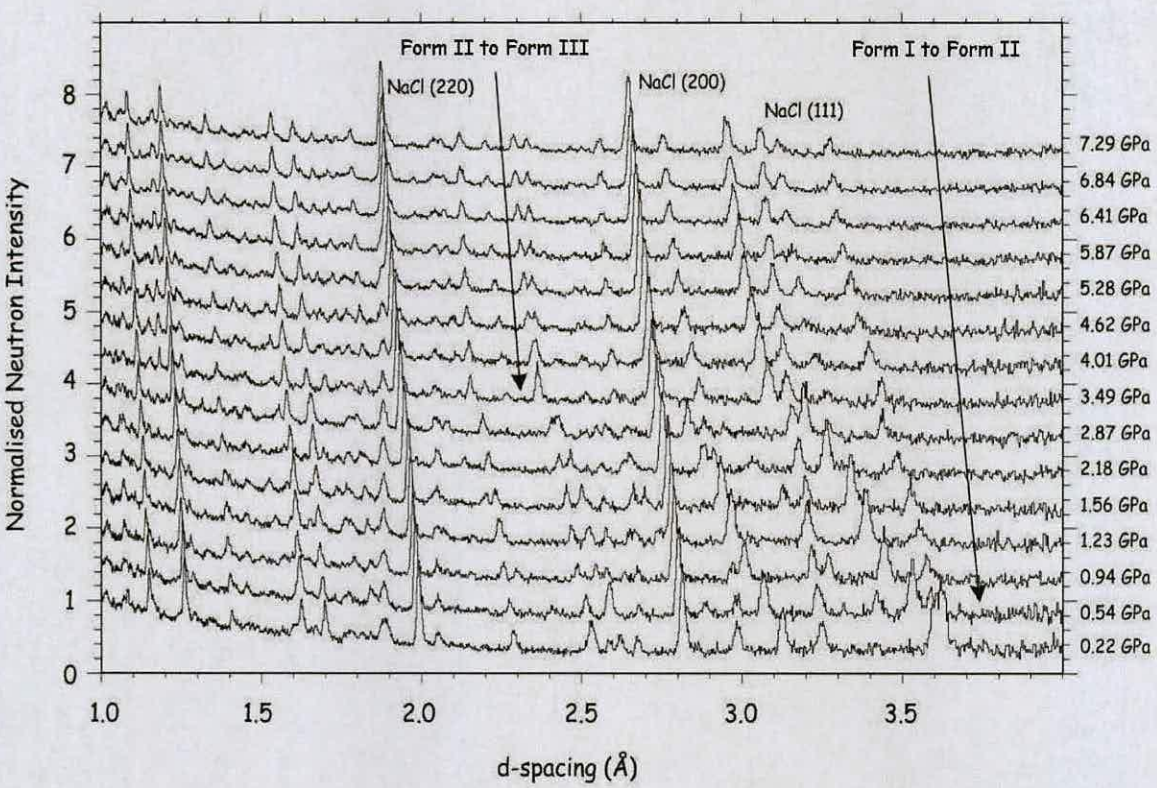

Figure 7.4. Powder neutron patterns of thiourea dioxide as a function of pressure and normalised neutron intensity.

Rietveld refinement of powder pattern at 0.22 GPa confirmed the presence of phase I of thiourea dioxide. On increasing the pressure to 0.54 GPa new peaks were observed to grow into the diffraction pattern (Figure 7.4). Indexing of this pattern confirmed the presence of a *new monoclinic cell*, space group $P2_1/n$ (denoted phase II- Table 7.3). This phase persisted until 2.87 GPa. Structure solution of phase II was performed by Dr. William G. Marshall at the ISIS Neutron Facility. Inspection of the lattice parameters and space groups for phase I and phase II showed that there was a sub-group relationship between $P2_1/n$ and *Pnma*. Thus, the coordinates for the *Pnma* structure were inserted into a $P2_1/n$ test refinement in GSAS. The structure was then successfully refined using heavy damping, and appropriate constraints on the molecular structure.

On increasing the pressure 3.49 GPa, further peaks were observed to appear in the powder pattern. Tentative indexing of this pattern suggested a *further new monoclinic cell* (phase III), space group $P2_1/n$, different from that of phase I and phase II. This was designated phase III. However, structural characterisation was not possible. This is not uncommon, since assignment of space group can often be a complex problem in powder neutron studies, where not only is resolution sacrificed for higher flux, but the constraints of the sample environment restrict the range of d-spacings that can be accessed.

On depressurisation, both transitions were observed. The results of Rietveld refinements for phases I and II can be seen in Figures 7.5 and 7.6.

	Phase I (0.01 GPa)	Phase II (0.54 GPa)
Crystal system	orthorhombic	monoclincic
Space group	*Pnma*	$P2_1/n$
a/ Å	10.6954(30)	10.7050(3)
b/ Å	10.1006(25)	10.0627(32)
c/ Å	3.8496(7)	3.7471(7)
α/ °	90	94.136(30)
β/ °	90	90
γ/ °	90	90
V/ Å^3	415.87(13)	402.59(4)
Z	4	4
D_c/ g cm^{-3}	1.79 (3)	1.95(2)
T/ K	293(2)	293(2)

Table 7.3. Lattice parameters for phases I and II of thiourea dioxide obtained from powder neutron diffraction.

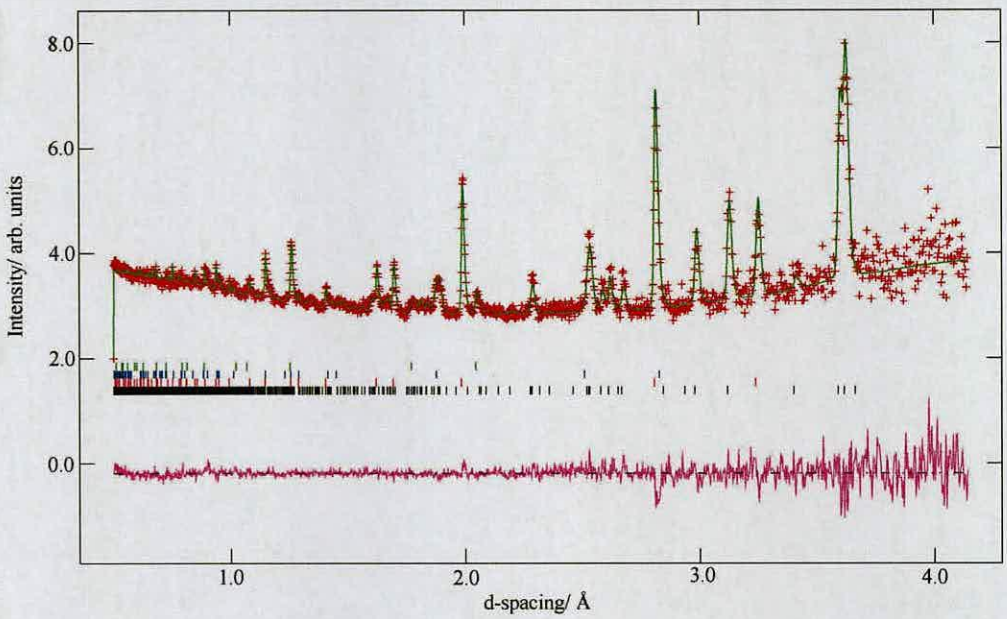

Figure 7.5. powder neutron pattern at 0.01 GPa. The crosses denote the observed intensities and the solid lines those calculated from the best-fit model of the Rietveld refinement. The tick marks represent the calculated peak positions, (black tick marks signify thiourea dioxide, the red marks correspond to the NaCl lead internal pressure marker, and the blue and green tick marks represent tungsten carbide and nickel, respectively). The line below them represents the deviation between observed and calculated intensities.

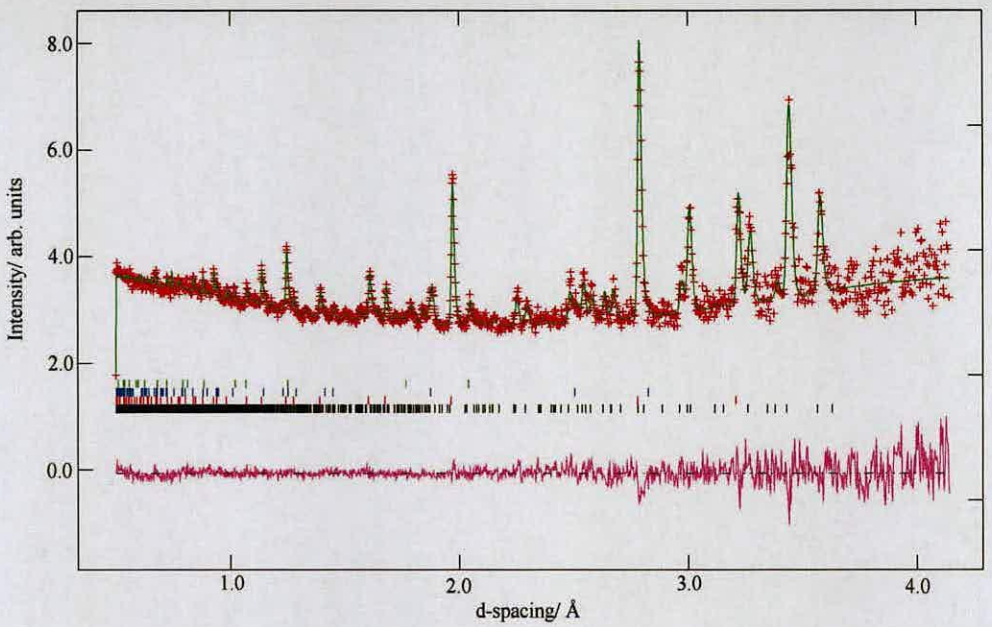

Figure 7.6. Powder neutron pattern at 0.54 GPa. The crosses denote the observed intensities and the solid lines those calculated from the best-fit model of the Rietveld refinement. The tick marks represent the calculated peak positions, (black tick marks signify thiourea dioxide, the red marks correspond to the NaCl internal pressure marker, and the blue and green tick marks represent tungsten carbide and nickel, respectively). The line below them represents the deviation between observed and calculated intensities.

7.3 High-Pressure Single-Crystal X-Ray Studies

7.3.1 Experimental

High-pressure single-crystal studies on a non-deuterated sample of thiourea dioxide were performed at the STFC Daresbury Laboratory on stations 9.8 and 16.2 using synchrotron radiation (λ = 0.6765 Å and λ = 0.8252 Å, respectively) on a Bruker APEX 2 diffractometer. High pressures were produced using a Merrill-Bassett diamond anvil cell (DAC) [12] equipped with 600 μm culet diamonds and a tungsten gasket. The sample and a small ruby chip were loaded into the DAC with a 4:1 mixture of methanol:ethanol as the pressure-transmitting medium. The pressure applied to the sample was determined by the ruby fluorescence method using a 632.8

nm line from a He-Ne laser [13]. The fluorescence was detected by a Jobin-Yvon LabRam 300. High-pressure data sets were collected in ω-scans in 10 settings of 2θ and φ with a frame and step size of 1s and 0.2°, respectively [14].

All single-crystal data sets were processed according to the procedure described by Dawson *et* al [15]. Integration of data sets and global cell refinement were carried out using the program SAINT [16], in which 'dynamic masks' were used in order to prevent integration of areas of the detector shaded by the body of the DAC. An analytical correction for the absorption by the DAC component was then applied using SHADE [17] and an absorption correction for the crystal was applied using SADABS [18]. All structures were solved by direct methods using SIR92 [19] and full-matrix least-squares-refinement against $|F|^2$ were performed using the program CRYSTALS [20].

7.3.2 Results

An initial data set was recorded at 0.1 GPa. Indexing of the reflections obtained confirmed the presence of phase I. Pressure was then increased to 0.9 GPa. Indexing of the reflections verified the existence of phase II, and demonstrated a single-crystal to single-crystal transition between phases I and II. Structure solution of the 0.9 GPa data *via* direct methods with subsequent full matrix least-squares refinement confirmed the structure of phase II, as previously observed in the powder neutron studies.

The pressure was further increased to 4.0 GPa, with no visual change in the crystal observed. Indexing of the reflections obtained confirmed the presence of a new orthorhombic unit cell but with space group *Pbma*. The unit cell parameters of phase III are given in Table 7.4. For ease of comparison between the three phases of thiourea dioxide, phase III is given in the non-standard setting of *Pbcm*. Subsequent structure solution *via* direct methods was then achieved. Refinement of the powder neutron data for phase III using the X-ray structure as a model was then possible, confirming that this was the correct structure. The result of the Rietveld refinement is shown in Figure 7.7.

	Phase I (0.1 GPa)	**Phase II (0.54 GPa)**	**Phase III (3.49 GPa)**
Crystal system	Orthorhombic	Monoclinic	Orthorhombic
Space group	*Pnma*	$P2_1/n$	*Pbma*
a/ Å	10.6954(30)	10.7050(3)	10.3704(26)
b/ Å	10.1006(25)	10.0627(32)	9.4309(19)
c/ Å	3.8496(7)	3.7471(7)	3.3952(5))
α/ °	90	94.136(30)	90
β/ °	90	90	90
γ/ °	90	90	90
V/ Å^3	415.87(13)	402.59(4)	332.06(8)
Z	4	4	4
D_c/ g cm^{-3}	1.79	1.95	2.31
T/ K	293(2)	293(2)	293(2)

Table 7.4. Lattice parameters for phases I, II and III of thiourea dioxide obtained from powder neutron diffraction.

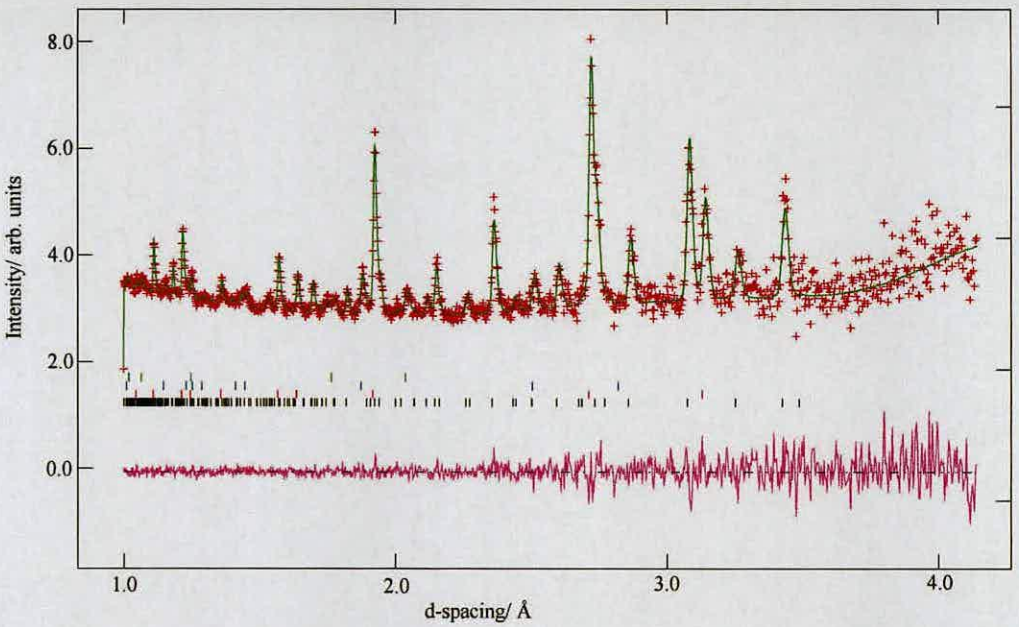

Figure 7.7. Powder neutron patterns of phase III of thiourea dioxide at 3.49 GPa. The crosses denote the observed intensities and the solid lines those calculated from the best-fit model of the Rietveld refinement. The tick marks represent the calculated peak positions, (black tick marks signify thiourea dioxide, the red marks correspond to the NaCl internal pressure marker, and the blue and green tick marks represent tungsten carbide and nickel, respectively). The line below them represents the deviation between observed and calculated intensities.

7.4 Discussion: High-Pressure Phases of Thiourea Dioxide

7.4.1 Phase II

The structure of phase II can be seen in Figure 7.8. The crystal structure comprises of a similar three dimensional hydrogen bonded network to that of phase I.

There is no significant change in the lengths of the primary bonds, in particular the C-S bond, as the pressure is increased to 0.54 GPa. However, between phase I and phase II, there is a loss of the mirror plane running through the carbon sulfur bond of the thiourea dioxide molecule, leading to a descent in space group

from *Pnma* to $P2_1/n$ (Figure 7.9). As the hydrogen atoms are no longer symmetry equivalent in phase II, the numbering scheme is altered (Figure 7.10).

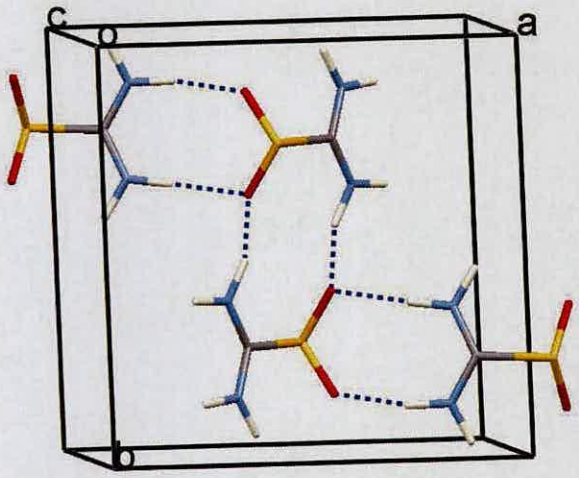

Figure 7.8. Crystal structure of phase II of thiourea dioxide viewed down the *c*-axis

Phase II possesses four distinct hydrogen bonds, D(1)...O(2), D(3)...O1, D(2)....O(1), and D(4)...O(2) the distances of each can be seen in Table 7.5.

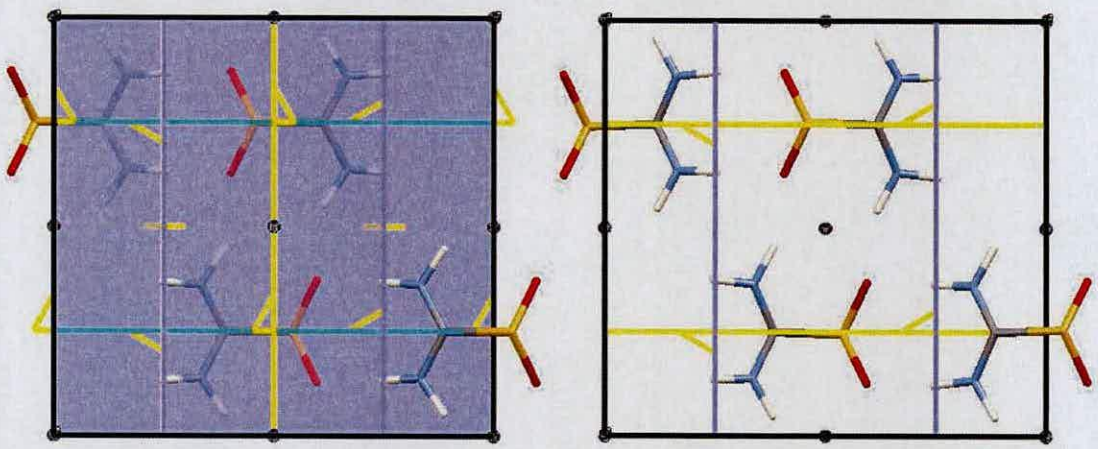

a b

Figure 7.9 (a) Crystal structure of phase I, (b) phase II viewed down the *c*-axis showing symmetry elements. (2_1 screw axis given in yellow, mirror planes in red, glide planes in purple, inversion centres in black).

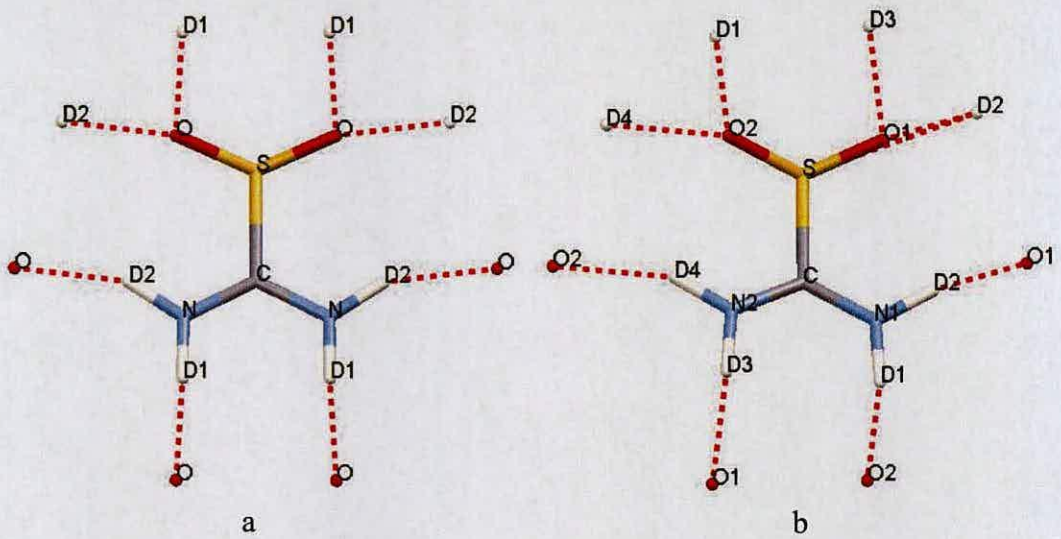

Figure 7.10. Numbering scheme of (a) phase I and (b) phase II of thiourea dioxide showing hydrogen bonding interactions

Hydrogen Bond	Phase I	Phase II
D(1)...O	1.833(4) Å	1.778(2) Å
D(3)...O(1)	N/A	1.887(3) Å
D(2)...O	1.899(4) Å	1.851(3) Å
D(4)...O(2)	N/A	1.920(2) Å

Table 7.5. Hydrogen bond lengths for phase I and II of thiourea dioxide

7.4.2 Phase III

Phase III crystallises in an orthorhombic crystal system, with space group *Pbcm* (Table 7.4). The lattice parameters are reported in a non standard setting to enable easier comparison with phases I and II. The view of the crystal structure down the *c*-axis is shown in Figure 7.11. Phases I and III show several similarities. There is no significant change observed in the C-S bond length between all three

phases. The main difference between the two structures is the presence of an *n* glide in phase I being replaced by a *b* glide in phase III, which allows a more efficient packing arrangement in phase III.

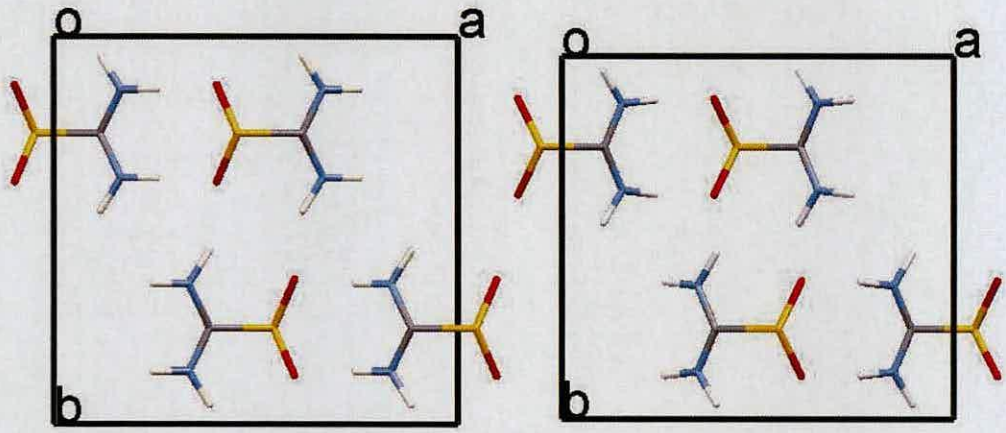

a b

Figure 7.11. Crystal structure of (a) phase I (b) phase III of thiourea dioxide viewed down the *c*-axis

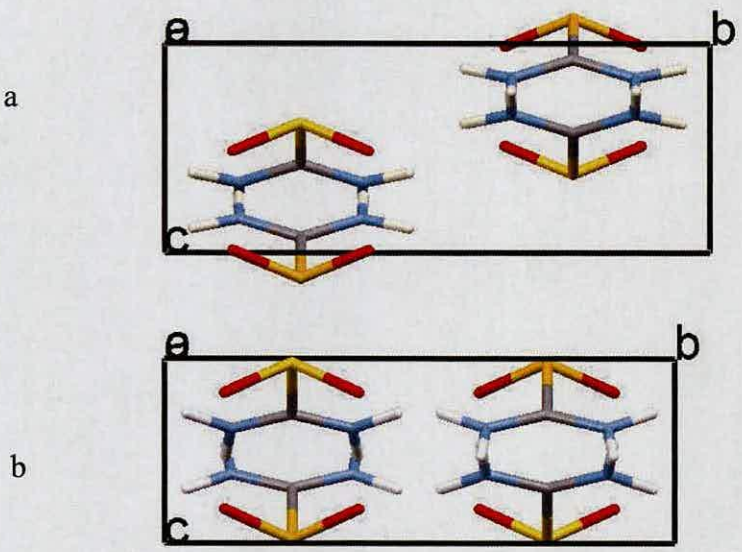

Figure 7.12. Crystal structure of (a) phase I, (b) phase III of thiourea dioxide viewed down the *a*-axis.

Inspection of Figure 7.12 reveals that the packing of the thiourea dioxide molecules in phase I in the direction of the (001) plane is a result of the *n* glide. However, the *b* glide present in phase III causes a more efficient packing arrangement where the thiourea dioxide molecules align themselves parallel to the *b* axis.

These different packing arrangements in phase I and phase III have an affect on the overall crystal structures (Figures 7.13 and 7.14). Phase I adopts a zigzagging array running parallel to the *a*-axis, which are related by the *n* glide. Phase II shows a very similar packing arrangement. On the other hand, in phase III the molecules adopt a herring-bone arrangement that causes phase III to be the most efficiently packed structure of the three phases. This is shown in the space-fill plots for phase I, and III (7.15).

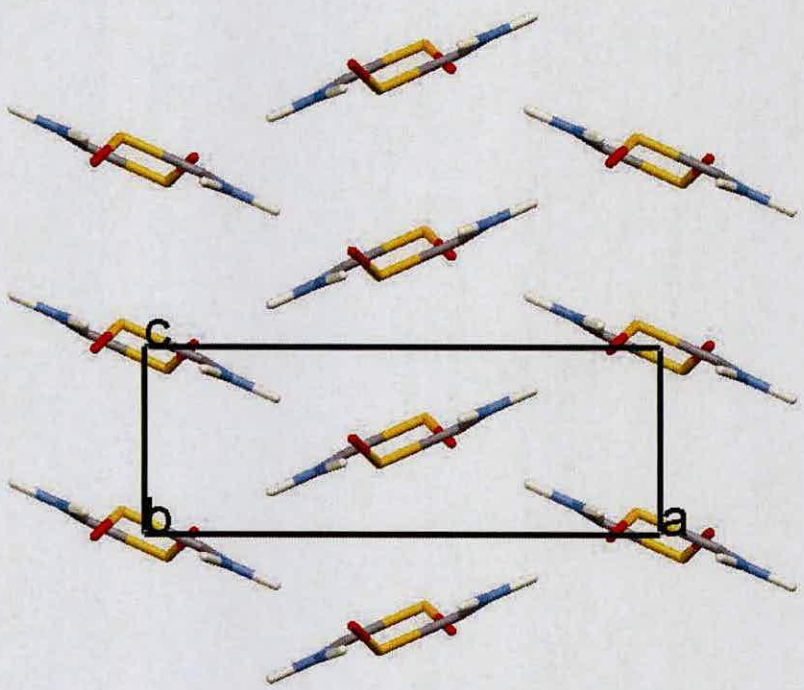

Figure 7.13. Crystal structure of phase I of thiourea dioxide viewed down the *b*-axis

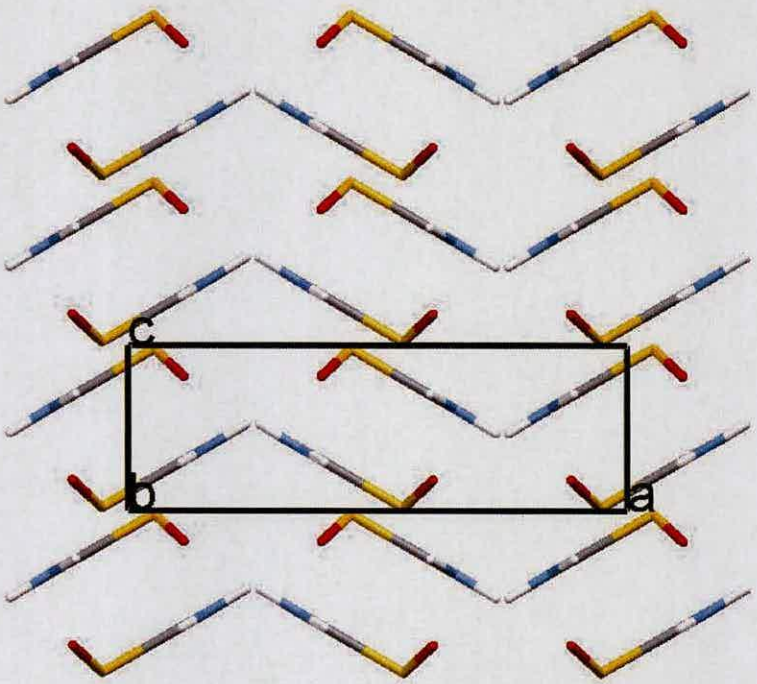

Figure 7.14. Crystal structure of phase III of thiourea dioxide viewed down the *b*-axis

A significant closing of the voids between phase I and phase II can be observed in Figures 7.15, with a further decrease in the voids in phase III. This is also in agreement with the fact that the density of the three phases is in the order I < II< III (Table 7.4).

Another effect of the transition from phase II to phase III is the return of the mirror plane running through the carbon sulfur bond in thiourea dioxide, as the structure changes from monoclinic to orthorhombic. There are two different hydrogen bonding interactions present in phase III, and these are presented in Table 7.6.

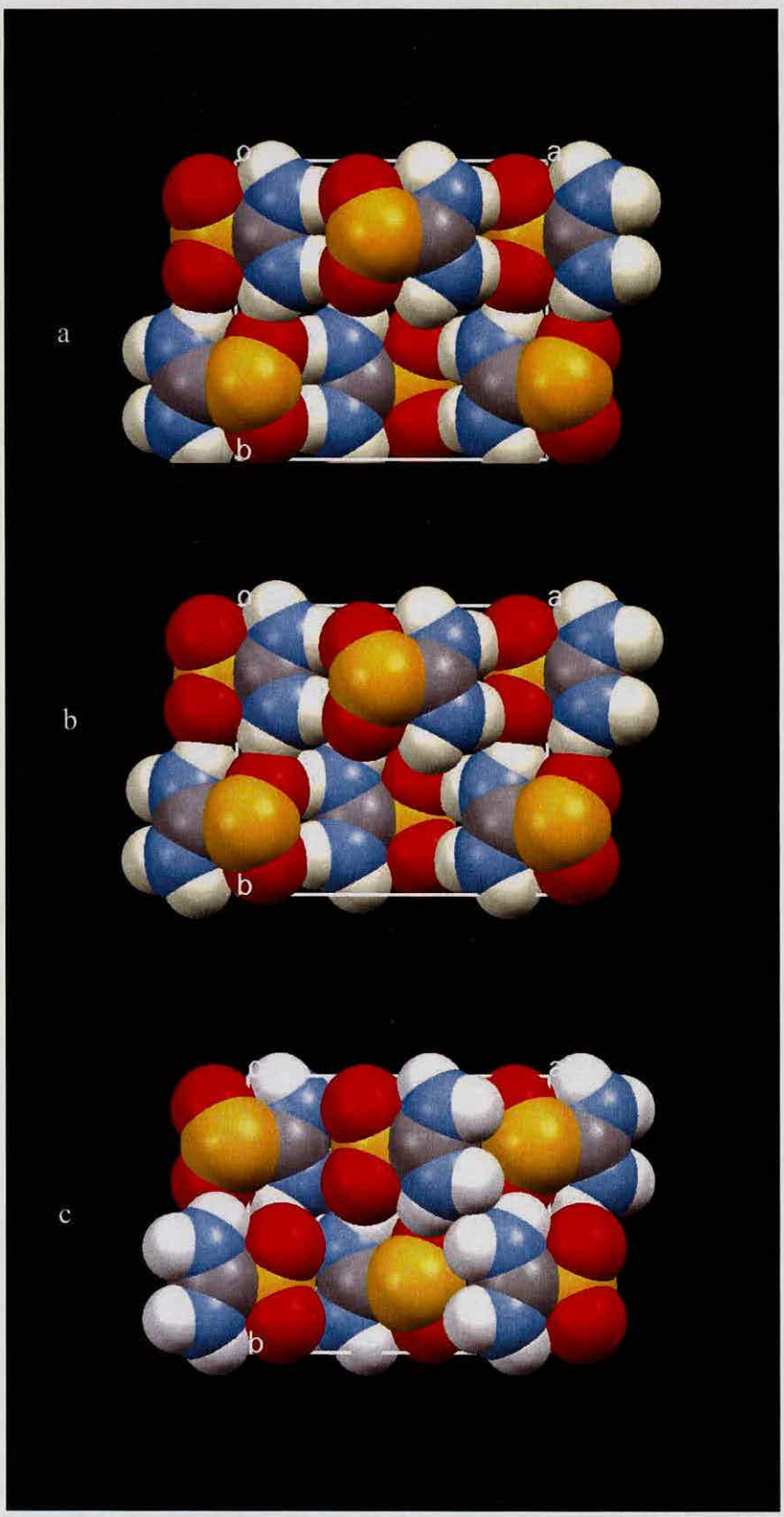

Figure 7.15. Space fill plot of (a) phase I, (b) phase II, (c) phase III of thiourea dioxide viewed down the *c*-axis

Hydrogen Bond	Phase I (0.01 GPa)	Phase III (3.49 GPa)
D(1)...O	1.833(4) Å	1.744(3) Å
D(2)...O	1.899(4) Å	2.292(3) Å

Table 7.6. Hydrogen bond lengths for phase I and III of thiourea dioxide

D(1)...O is shorter in phase III than in phase II, but the D(2)...O interaction increases between the phases. This is illustrated in Figures 7.16 and 7.17 which show the variation of D(1)...O and D(2)...O with increasing pressure. All bond length errors represent ±σ. This lengthening of the D(2)...O interaction is slightly unusual, but consideration of the packing arrangements of thiourea dioxide suggests a possible explanation for this.

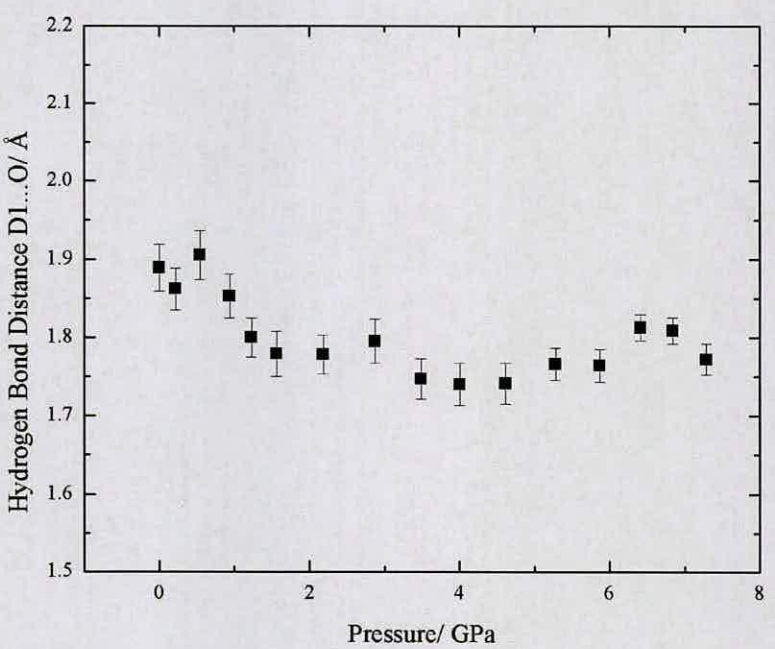

Figure 7.16 Variation of hydrogen bonding distance D(1)...O with increasing pressure

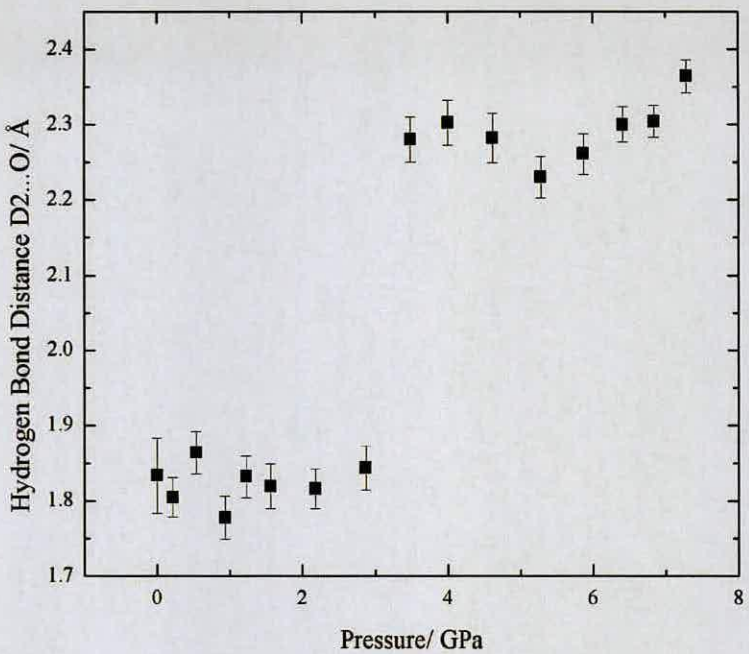

Figure 7.17 Variation of hydrogen bonding distance D(2)…O with increasing pressure

The D(2)...O distance increases slightly between phase II and phase III as a result of the herringbone packing arrangement (Figure 7.18).

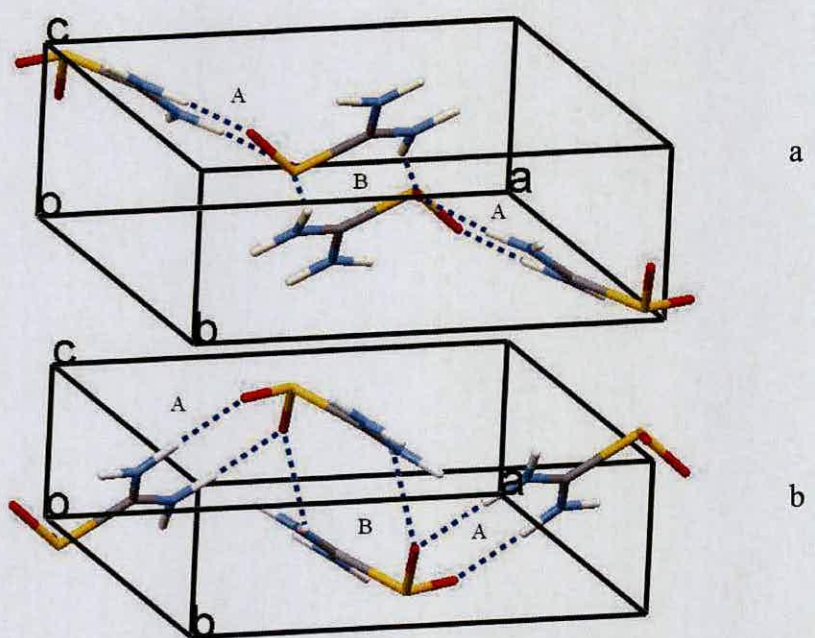

Figure 7.18. Hydrogen bonding network in (a) phase I, (b) phase III of thiourea dioxide. A corresponds to D(1)…O, B corresponds to D(2)...O

The variation in the lattice parameters obtained from powder neutron measurements are shown in Figures 7.19-7.21. Figure 7.19 shows an overall decrease in the *a*-axis with increasing pressure. A continuous decrease of the *c*-axis can also be observed with increasing pressure (Figure 7.20). However, of particular interest is Figure 7.21, which shows the variation of the *b*-axis of thiourea dioxide with increasing pressure. A decrease can be seen between phase I and II until a pressure of 2.9 GPa. At this pressure, an increase in the *b* lattice parameter can be observed. This can be rationalised in terms of the hydrogen bonding network of the three phases of thiourea dioxide. The formation of the efficient herringbone packing arrangement in phase II causes a lengthening of the D(2)...O interaction. This hydrogen bond has a considerable component along the *b*-axis, and thus could explain the marked increase seen in the *b*-axis between 2.9 GPa and 4.0 GPa.

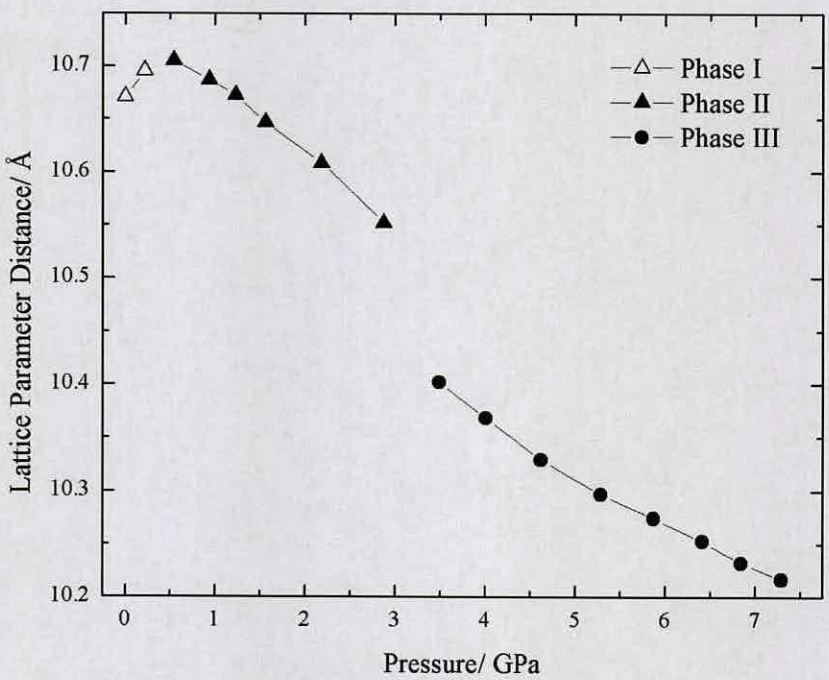

Figure 7.19. Plot of *a*-axis of thiourea dioxide with increasing pressure

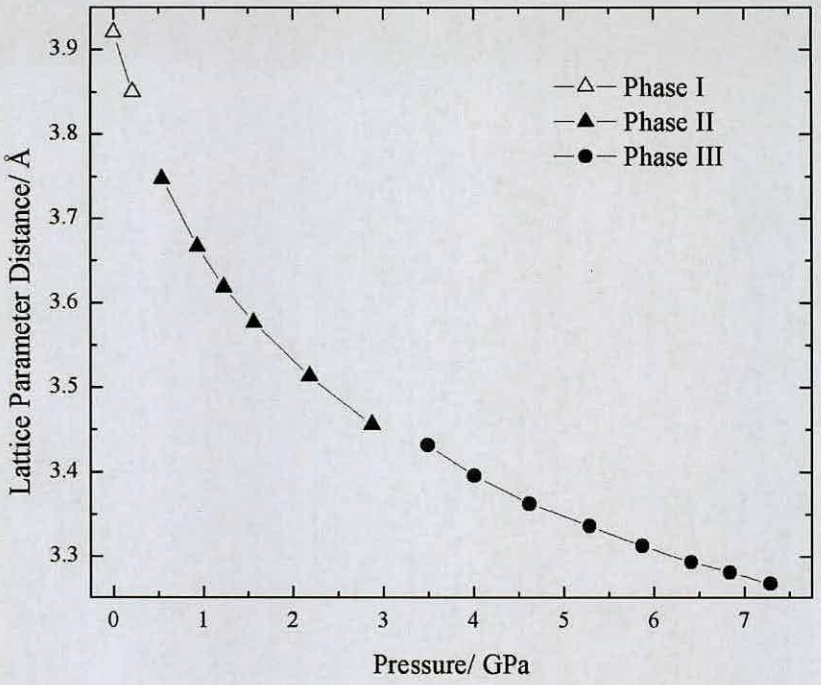

Figure 7.20. Plot of *c*-axis of thiourea dioxide with increasing pressure

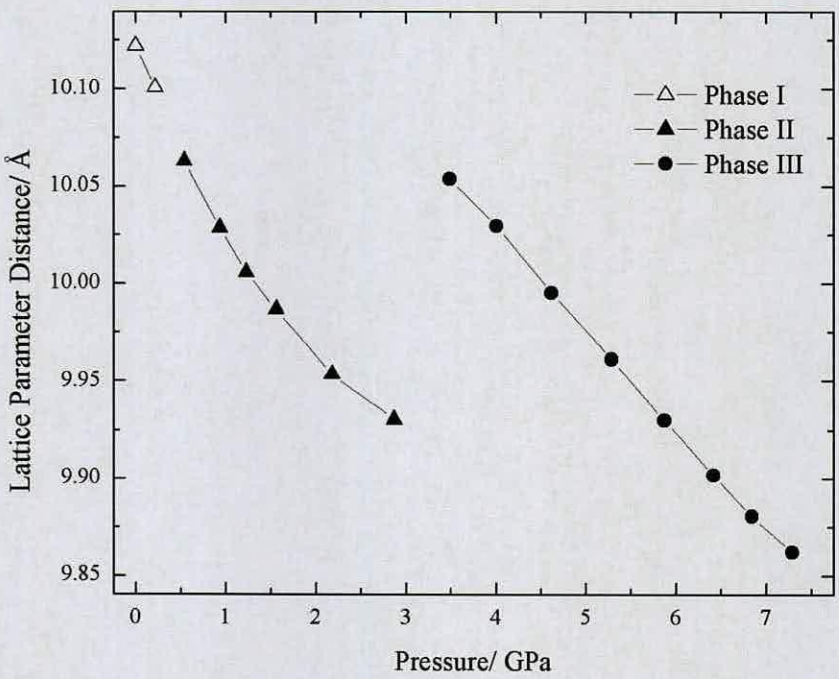

Figure 7.21. Plot of *b*-axis of thiourea dioxide with increasing pressure

The variation of volume with increasing pressure is given in Figure 7.22. A decrease in volume of 3.2% can be seen between phases I and II. However, due to the small number of data points of phase I, it is difficult to conclude whether the transition between phase I and phase II is first or second order. There is a more noticeable decrease in volume (4%) between phases II and III, which is accompanied by a change in lattice parameters, indicating that the phase II → phase III transition is first order transition.

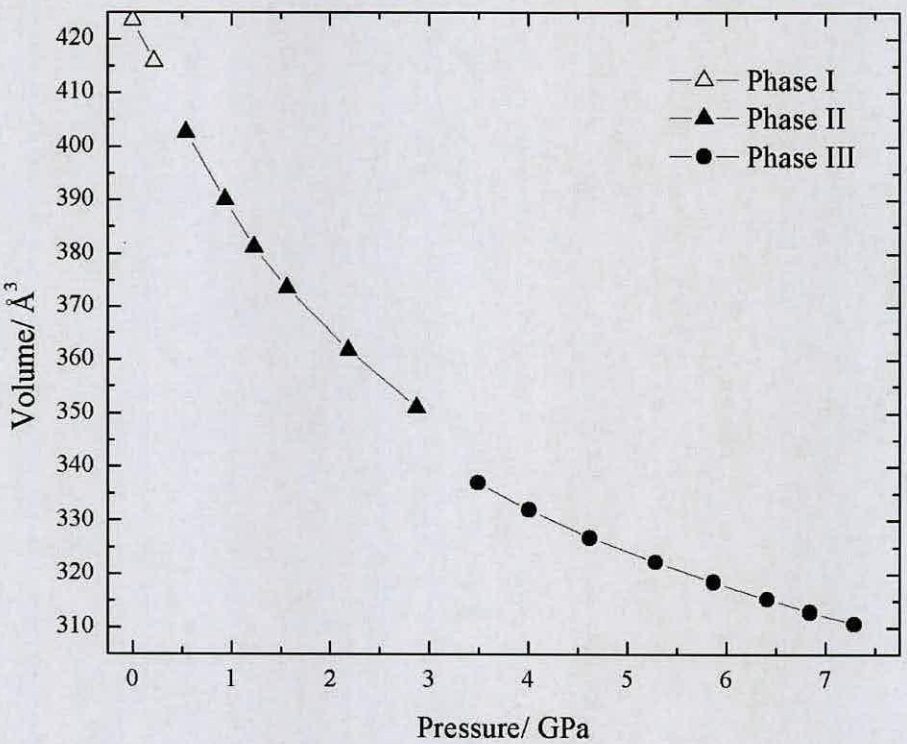

Figure 7.22. Variation in volume of thiourea dioxide with increasing pressure

The unit-cell volume obtained from the neutron diffraction measurements were used for the determination of the bulk modulus, B_o using a third-order Birch–

Murnaghan equation of state (equation 7.1) for phases II and III. An equation of state was not calculated for phase I on account of only two data points being collected.

$$P = (3/2)\, B_0(x^{-7/3}-x^{-5/3})\,[1-(3/4)(4-B_0')(x^{-2/3}-1)] \qquad \text{Equation 7.1.}$$

Equation 7.1. x denotes the volume ratio V/V_o, V_o the volume at zero pressure, and B_o and B_0' the initial isothermal bulk modulus and its pressure derivative, respectively.

A least-squares fit to the measured data of phase II value of $B_o = 9.81(2)$ GPa for the bulk modulus. A least squares analysis for the pressure range 3.1 GPa to 7.29 GPa gives a value of $B_o = 27.65(10)$ for phase III. The ambient-pressure unit-cell volume V_o was treated as a refinable parameter, yielding a value of 426.59(6)Å^3 for phase II, and 372.51(16) Å^3 for phase III of thiourea dioxide. Thus the fact that phase III is less compressible than phase II is in good agreement that phase III is also the densest structure.

7.5 Conclusions

Two new high pressure structures of thiourea dioxide have been structurally characterised at 0.54 GPa and 3.1 GPa, using neutron powder diffraction and single-crystal X-ray diffraction. These three structures are closely related, with no significant change observed in the unusual C-S bond length. However, the three different phases display different hydrogen bonding networks. Phase III is much less compressible than phase II.

This study underlines how high pressure techniques are an excellent way of studying not only polymorphism in simple molecular compounds, but in addition

provides a manner to tune and explore intermolecular interactions in such compounds.

7.6 References

[1] Allan, D. R., Clark, S. J., Dawson, A., McGregor, P. A., Parsons, S. *Acta Cryst.*, 2002, *B***58**, 1018.

[2] Allan, D. R., Clark, S. J., Ibberson, R. M., Parsons, S., Pulham, C. R. *Chem. Commun.*, 1999, **8**, 751.

[3] W. G. Marshall, (2003). *ISIS annual report*

[5] R. A. L. Sullivan, A.Hargreaves, *Acta. Cryst.,* 1962, **15**, 675.

[5] M. M. Elcombe, J. C. Taylor, *Acta. Cryst.,* 1968, **A24**, 405.

[6] I. C. Chen, Y. Wang, *Acta Cryst.*, 1984, *C***40**, 1937.

[7] J. M. Besson, R. J. Nelmes, G. Hamel, J. S. Loveday, G. Weill, S. Hull, *Physica B.*, 1992, **180–181**, 907.

[8] W. G. Marshall and D. Francis, *J. Appl. Crystallogr.*, 2002, **35**, 122.

[9] D. L. Decker, *J. Appl. Phys.*, 1971, **42**, 3239.

[10] A. C. Larson, R. B. Von Dreele, *Los Alamos National Laboratory Report* No. LA-UR-86-748., 1987.

[11] I. J. Bruno, J. C. Cole, P. R. Edgington, M. Kessler, C. F. Macrae, P. McCabe, J. Pearson, R. Taylor, *Acta. Cryst.*, *B***58**, 389.

[12] L. Merrill, W. A. Bassett, *Rev. Sci. Instrum.*, 1974, **45**, 290.

[13] G. J. Piermarini, S. Block, J. D. Barnett, R. A. Forman, *J. Appl. Phys.,* 1975, **46**, 2774.

[14] S. A. Moggach, D. R. Allan, S. Parsons, L. Sawyer, J. E. Warren, *J. Synchrotron Rad.*, 2005, **12**, 598.

[15] A. Dawson, D. R. Allan, S. Parsons, M. Ruf, *J. Appl. Crystallogr.*, 2004, **37**, 410.

[16] Bruker AXS, SAINT, Version 7.01A, Bruker-AXS, Madison, Wisconsin (USA), 2003.

[17] S. Parsons, SHADE. The University of Edinburgh (Scotland), 2004.

[18] G. M. Sheldrick, SADABS, version 2004/1, University of Göttingen (Germany), 2004.

[19] A. Altomare, A., G. Cascarano, C. Giacovazzo, A. Guagliardi, *J. Appl. Cryst.*, 1993, **26**,343.

[20] P.W. Betteridge J. R. Carruthers, R. I. Cooper, C. K. Prout, D. J. Watkin, *J. Appl. Cryst.*, 2003, **36**, 1487.

Chapter 8

Conclusions, General Remarks and Future Directions

Chapter Eight: Conclusions, General Remarks and Future Directions

The work presented in this thesis has demonstrated that the significant recent advances in the techniques for the collection and analysis of high-pressure data can lead to the full structural characterisation of a range of materials under extreme conditions. HMX, RDX, TATP, ammonium nitrate, ammonium perchlorate, hydroxylammonium perchlorate and thiourea dioxide have been studied using high-pressure diffraction techniques. Structural information has been obtained at elevated pressures and temperatures for the first time, including the structure solution and refinement of a variety of new high-pressure phases and solvates. A key factor of this success has been the combination of a range of techniques that include single-crystal X-ray diffraction, powder X-ray diffraction, powder neutron diffraction and Raman spectroscopy.

Of particular importance has been the successful determination of the structure of the high-pressure γ-form of RDX. This lends confidence that these high-pressure methods may be used to study relatively complex energetic compounds where conformational flexibility may be very important.

Comparisons with previous high-pressure studies highlight several discrepancies. Some of these inconsistencies may reflect the importance of hydrostatic and non-hydrostatic conditions on the occurrence of phase transitions, which has been highlighted by the case of ammonium nitrate. However, it is also clear that the existing literature on energetic materials should be treated with caution and some reported results may be erroneous.

High-pressure techniques have been shown to be an excellent tool for probing polymorphism in a range of materials. This is underlined by the high pressure study of the simple molecular compound thiourea dioxide. Two novel high pressure phases have been identified, which display different hydrogen bonding networks.

The discovery of a range of new high-pressure polymorphs and solvates stems from several reasons. High-pressure conditions encourage denser structures in which molecules pack together more efficiently, leading to closure of voids in the structure. This means that changes in the relative orientations of molecules in a solid are very likely to occur, thereby giving rise to different motifs of intermolecular interactions. These interactions are themselves sensitive to distance, and hence to the effects of pressure. The strengths of these intermolecular interactions are susceptible to the relatively modest pressures used in these studies.

Further work to investigate the high-pressure behaviour of energetic materials will very likely lead to rich and interesting phase behaviour. Of particular interest could be to study ammonium nitrate under genuine non-hydrostatic conditions, including shear-stress strain. In addition, further crystallisations both at high pressure and at ambient conditions could lead to new polymorphs and solvates of HMX in particular, but also of other energetic materials.

Appendix

Appendix A: Crystallographic Data

Crystallographic Information Files for the structures described in Chapters 3,5,6 and 7 are on the attached CD.

Chapter 3: RDX and HMX

X-ray Data	**γ-RDX at 5.2 GPa**
Crystal data	
Chemical formula	C3 H6 N6 O6
M_r	222.12
Cell setting, space group	Orthorhombic, $Pca2_1$
Temperature (K)	293(2)
a, b, c (Å)	12.5650(19), 9.4769(6), 10.9297(9)
V (Å^3)	1301.5(2)
Z	8
D_x (Mg m^{-3})	2.282
Radiation type	Synchrotron radiation
No. of reflections for cell parameters	1200
θ range (°)	3-23
μ (mm^{-1})	0.216
Crystal form, colour	Block, colourless
Crystal size (mm)	0.06 × 0.15 × 0.20
Data collection	
Diffractometer	Bruker Nonius Apex II
Data collection method	ω
Absorption correction	multiscan
T_{min}	0.49
T_{max}	0.99
No. of measured, independent and observed reflections	4339, 872
Criterion for observed reflections	$I > 2.00u(I)$

R_{int}	0.079
θ_{max} (°)	24.8
Range of h, k, l	$0 \rightarrow h \rightarrow 11$
	$0 \rightarrow k \rightarrow 11$
	$0 \rightarrow l \rightarrow 12$
Refinement	
Refinement on	F^2
$R[F^2 > 2\sigma(F^2)]$, $wR(F^2)$, S	0.070, 0.1723, 0.879
No. of relections	872 reflections
No. of parameters	123
H-atom treatment	Constrained to parent site
Weighting scheme	Calculated $w = 1/[\sigma^2(F^2) + (0.08P)^2 + 0.8P]$ where $P = (\max(F_o^2,0) + 2F_c^2)/3$
$(\Delta/\rho)_{max}$	0.000056
$\Delta\rho_{max}$, $\Delta\rho_{min}$ (e Å^{-3})	0.94, –0.53

Neutron Data	**γ-RDX at 3.9 GPa**
Crystal data	
Chemical formula	C3 D6 N6 O6
M_r	228.071
Cell setting, space group	Orthorhombic, $Pca2_1$
Temperature (K)	293(2)
a, b, c (Å)	12.6319(15), 9.5554(10), 11.0030(22)
V (Å^3)	1328.17(23)
Z	8
D_x (Mg m^{-3})	2.267
wRp	0.0268
Parameters	161
Restraints	86

X-ray Data	**HMX-DMSO (1:2) Solvate at 0.1 GPa**
Crystal data	
Chemical formula	C8 H20 N8 O10 S2
M_r	452.53
Cell setting, space group	Monoclinic, $P2_1/a$
Temperature (K)	293(2)
a, b, c (Å)	11.734(4), 7.109(4), 11.547(2)
B /□	95.620(17)
V (Å^3)	958.5(7)
Z	2
D_x (Mg m^{-3})	1.567
Radiation type	Synchrotron radiation
No. of reflections for cell parameters	709
θ range (°)	8-47
μ (mm^{-1})	0.344
Crystal form, colour	Block, colourless
Crystal size (mm)	0.05 × 0.10 × 0.15
Data collection	
Diffractometer	Bruker Nonius Apex II
Data collection method	ω
Absorption correction	multiscan
T_{min}	0.47
T_{max}	0.94
No. of measured, independent and observed reflections	492, 492
Criterion for observed reflections	$I > 3.00u(I)$
R_{int}	0.065
θ_{max} (°)	20.830
Range of h, k, l	$-10 \rightarrow h \rightarrow 10$
	$0 \rightarrow k \rightarrow 4$
	$0 \rightarrow l \rightarrow 11$
Refinement	
Refinement on	F^2

$R[F^2 > 2\sigma(F^2)]$, $wR(F^2)$, S	0.1639, 0.1941, 0.2201
No. of relections	360 reflections
No. of parameters	69
H-atom treatment	Constrained to parent site
Weighting scheme	Chebychev polynomial
$(\Delta/\rho)_{max}$	0.001318
$\Delta\rho_{max}$, $\Delta\rho_{min}$ (e Å^{-3})	0.81, –0.57

Chapter 4: Restricted Annex

Chapter 5: Ammonium Perchlorate

X-ray data	**Phase II of ammonium perchlorate at 4.2 GPa**
Crystal data	
Chemical formula	$NH_4.ClO_4$
M_r	117.49
Cell setting, space group	Orthorhombic, *Pnma*
Temperature (K)	293(2)
a, b, c (Å)	7.4200 (8), 6.3230 (8), 7.0830 (19)
V (Å^3)	332.31 (10)
Z	4
D_x (Mg m^{-3})	2.348
Radiation type	Synchrotron radiation, Zr edge
No. of reflections for cell parameters	627
θ range (°)	4–24
μ (mm^{-1})	1.00
Crystal form, colour	Block, colourless
Crystal size (mm)	0.20 × 0.20 × 0.15
Data collection	
Diffractometer	Bruker SMART
Data collection method	ω

Absorption correction	Empirical (using intensity measurements) + multiscan
T_{min}	0.56
T_{max}	0.86
No. of measured, independent and observed reflections	1256, 229, 154
Criterion for observed reflections	$I > 2.00u(I)$
R_{int}	0.039
θ_{max} (°)	24.8
Range of h, k, l	$0 \rightarrow h \rightarrow 9$
	$0 \rightarrow k \rightarrow 7$
	$0 \rightarrow l \rightarrow 5$
Refinement on	F^2
$R[F^2 > 2\sigma(F^2)]$, $wR(F^2)$, S	0.083, 0.181, 1.01
No. of relections	187 reflections
No. of parameters	35
H-atom treatment	Constrained to parent site
Weighting scheme	Calculated $w = 1/[\sigma^2(F^2) + (0.0P)^2 + 9.21P]$ where $P = (\max(F_o^2,0) + 2F_c^2)/3$
$(\Delta/\sigma)_{max}$	0.001
$\Delta\rho_{max}$, $\Delta\rho_{min}$ (e Å^{-3})	0.69, –0.98
Extinction method	None
Extinction coefficient	

Neutron data	**Phase II of ammonium perchlorate at 4.6 GPa**
Crystal data	
Chemical formula	$ND_4.ClO_4$
M_r	121.51
Cell setting, space group	Orthorhombic, *Pnma*
Temperature (K)	293(2)
a, b, c (Å)	7.4070(11), 6.3209(9), 7.0734(11)
V (Å^3)	331.17(6)
Z	4

D_x (Mg m^{-3})	2.35
wRp	0.050
Parameters	51
Restraints	12

Chapter Six: Hydroxylammonium Perchlorate

X-Ray Data	**Hydroxyl ammonium perchlorate phase B at 333 K**
Crystal data	
Chemical formula	$NOH_4.ClO_4$
M_r	133.49
Cell setting, space group	Monoclinic, $P2_1/n$
Temperature (K)	343
a, b, c (Å) γ (˚)	7.496(4), 7.078(4), 24.117(11) 94.86(3)
V (Å^3)	1275.1(11)
Z	12
D_x (Mg m^{-3})	2.086
Radiation type	Mo $K\alpha$
No. of reflections for cell parameters	2421
θ range (°)	5-54
μ (mm^{-1})	0.83
Crystal form, colour	Block, colourless
Crystal size (mm)	0.30 × 0.30 × 0.5
Data collection	
Diffractometer	Bruker SMART
Data collection method	ω/2θ
Absorption correction	multiscan

T_{min}	0.20
T_{max}	1.00
No. of measured, independent and observed reflections	4658, 2136, 1286
Criterion for observed reflections	$I > 2.00u(I)$
R_{int}	0.047
θ_{max} (°)	30.8
Range of h, k, l	$-7 \rightarrow h \rightarrow 10$
	$-9 \rightarrow k \rightarrow 5$
	$-27 \rightarrow l \rightarrow 25$
Refinement	
Refinement on	F^2
$R[F^2 > 2\sigma(F^2)]$, $wR(F^2)$, S	0.1317, 0.746, 1.02
No. of relections	1286 reflections
No. of parameters	191
H-atom treatment	Constrained to parent site
Weighting scheme	Chebychev polynomial
$(\Delta/\sigma)_{max}$	0.007
$\Delta\rho_{max}$, $\Delta\rho_{min}$ (e Å^{-3})	0.80, -0.60
Extinction method	Larson 1970 Crystallographic Computing eq 22
Extinction coefficient	360 (90)

Neutron Data	**Hydroxyl ammonium perchlorate phase B at 343 K**
Crystal data	
Chemical formula	$NOD_4.ClO_4$
M_r	137.51
Cell setting, space group	Monoclinic, $P2_1/n$
Temperature (K)	363
a, b, c (Å) γ ( )	7.52125(18), 7.12694(17), 24.36605(32) 95.1184(32)

V (Å^3)	1305.89(5)
Z	12
D_x (Mg m^{-3})	2.082
wRp	0.0491
Parameters	133
Restraints	68

Chapter Seven: Thiourea Dioxide

X-Ray data	**Phase II of thiourea dioxide at 0.90 GPa**	**Phase III of thiourea dioxide at 4.0 GPa**
Crystal data		
Chemical formula	$C(NH_2)_2S(O_2)$	$C(NH_2)_2S(O_2)$
M_r	108.12	108.12
Cell setting, space group	Monoclinic, $P2_1/n$	Orthorhombic, *Pbma*
Temperature (K)	293(2)	293(2)
a, b, c (Å) β(°)	10.7013(10), 10.703(3), 3.7588(5) 93.560(16)	10.347(5), 9.455(8), 3.3925(10) n/a
V (Å^3)	404.40(14)	331.9(3)
Z	4	4
D_x (Mg m^{-3})	1.776	2.164
Radiation type	Synchrotron radiation	Synchrotron radiation
No. of reflections for cell parameters	679	295
θ range (°)	8-48	4–24
μ (mm^{-1})	0.643	0.784
Crystal form, colour	Block, colourless	Block, colourless
Crystal size (mm)	0.10 × 0.15 × 0.15	0.10 × 0.15 × 0.20
Data collection		

Diffractometer	Bruker SMART APEX II	Bruker SMART APEX II
Data collection method	ω	ω
Absorption correction	multiscan	multiscan
T_{min}	0.66	0.248
T_{max}	1.00	1.00
No. of measured, independent and observed reflections	363, 346	740,237,137
Criterion for observed reflections	$I > 2.00u(I)$	$I > 2.00u(I)$
R_{int}	0.043	0.057
θ_{max} (°)	26.35	23.022
Range of h, k, l	$-4 \rightarrow h \rightarrow 4$	$-9 \rightarrow h \rightarrow 10$
	$0 \rightarrow k \rightarrow 13$	$-6 \rightarrow k \rightarrow 5$
	$0 \rightarrow l \rightarrow 6$	$-3 \rightarrow l \rightarrow 3$
Refinement on	F^2	F^2
$R[F^2 > 2\sigma(F^2)]$, $wR(F^2)$, S	0.0790, 0.1482, 1.07	0.1183, 0.2040, 0.89
No. of relections	300	137
No. of parameters	55	15
H-atom treatment	Constrained to parent site	Constrained to parent site
Weighting scheme	Calculated $w = 1/[\sigma^2(F^2) + (0.0P)^2 + 9.21P]$ where $P = (\max(F_o^2,0) + 2F_c^2)/3$	Method = Quasi-unit weights. w = 1.0 or ½ F
$(\Delta/\sigma)_{max}$	0.0014	0.0005
$\Delta\rho_{max}$, $\Delta\rho_{min}$ (e Å^{-3})	0.35, -0.31	0.73, –0.92
Extinction method	none	None
Extinction coefficient		

Neutron Data	**Phase II of thiourea dioxide at 0.54 GPa**	**Phase III of thiourea dioxide at 3.49 GPa**
Crystal data		
Chemical formula	$C(ND_2)_2S(O_2)$	$C(ND_2)_2S(O_2)$
M_r	112.14	112.14
Cell setting, space group	Monoclinic, $P2_1/n$	Orthorhombic, *Pbma*

Temperature (K)	293(2)	293(2)
a, b, c (Å)	10.7050(33), 10.0627(32), 3.747(7)	10.3704(26), 9.4309(19), 3.3952(5)
$\beta(^{\circ})$	94.136(30)	n/a
V (Å^3)	402.59(17)	332.06(8)
Z	4	4
D_x (Mg m^{-3})	1.95	2.31
wRp	0.0489	0.0484
Parameters	52	52
Restraints	27	27

Appendix B: Publications

Publications are included as an electronic copy in the attached CD at the back of the thesis.

Alistair J. Davidson, Iain D. H. Oswald, Duncan J. Francis, Alistair R. Lennie, William G. Marshall, David I. A. Millar, Colin R. Pulham, John E. Warren, and Adam S. Cumming. **Explosives under pressure – the crystal structure of γ-RDX determined by high-pressure X-ray and neutron diffraction**, CrystEngComm, 2008, 10, 162–165.

Francesca P. A. Fabbiani, David R. Allan, William I. F. David, Alistair J. Davidson, Alistair R. Lennie, Simon Parsons, Colin R. Pulham, and John E. Warren. **An Exploration of the Behaviour of Piracetam**. *Crystal Growth & Design*. 2007, **7(6)** 1115.